BOŠTJAN GOLOB

A Study of the Decays of B_s^0 Mesons produced at the Z^0 Resonance at LEP

Doctoral Thesis

SUPERVISOR: Ass. Prof. Danilo Zavrtanik

Ljubljana, 1996

Boštjan Golob

Študij razpadov mezona B_s^0 na trkalniku LEP

Disertacija

MENTOR: Doc. dr. Danilo Zavrtanik

Ljubljana, 1996

Špeli in Gaji, za dni, ko nismo bili skupaj

Abstract

In the present work the measurement of the B_s^0 meson lifetime is described. The lifetime was measured in two isolated samples of B meson semileptonic decays recorded by the Delphi spectrometer at LEP. The first data sample consists of a reconstructed ϕ meson accompanied by a high transverse momentum lepton in the same hadronic jet. In the second sample a $D_s^{\pm}$ meson was reconstructed in the same jet as an identified lepton $\ell^{\mp}$ of the opposite electric charge. The selection of a high p_t lepton enriches the samples in semileptonic decays of hadrons, containing the b quark, and the ϕ and $D_s^{\pm}$ mesons assure a high fraction of B_s^0 mesons in selected events. The $\phi\ell$ final state benefits from a high available statistics which is found to be crucial for the performed lifetime measurement. On the other hand the $D_s^{\pm}\ell^{\mp}$ analysis offers a better signal to background ratio and thus lower systematical error of the measurement. The combination of results obtained by the two analyses yields an average lifetime of the B_s^0 meson $\tau_{B_s} = (1.66 \pm 0.19)$ ps.

Povzetek

V pričujočem delu je predstavljena meritev življenjskega časa mezona B_s^0. Meritev je bila izvedena na dveh vzorcih semileptonskih razpadov mezonov B zabeleženih s spektrometrom Delphi, ki deluje na trkalniku LEP. Prvi vzorec vsebuje dogodke z rekonstruiranim mezonom ϕ v hadronskem pljusku skupaj z leptonom visoke transverzalne gibalne količine. Drugi vzorec je sestavljen iz

7

mezonov $D_s^\pm$, ki jih spremlja nasprotno nabiti lepton $\ell^\mp$. Izbira leptonov z visoko transverzalno gibalno količino omogoča obogatitev obeh vzorcev s semileptonskimi razpadi hadronov, sestavljenih iz kvarkov b, prisotnost mezonov ϕ ter $D_s^\pm$ v končnem stanju pa poveča delež mezonov B_s^0 v izbranih dogodkih. Izbrani vzorec s končnim stanjem $\phi\ell$ zagotavlja visoko statistično moč meritve, ki je pri določanju življenjskega časa mezona B_s^0 bistvenega pomena. Pri analizi dogodkov z mezonom $D_s^\pm$ je ozadje manjše, to pa se zrcali v manjši sistematični napaki meritve. Kombinacija obeh rezultatov da za povprečni življenjski čas mezona B_s^0 vrednost $\tau_{B_s} = (1.66 \pm 0.19)$ ps.

Ključne besede: LEP, Delphi, B_s^0 mezon, življenjski čas, ϕ mezon, $D_s^\pm$ mezon

PACS: 13.20.He   Decays of bottom mesons

14.40.Nd   Bottom mesons

Contents

Part I

Phenomenology of B_s^0 Meson Production and Decay

Chapter 1

Introduction

The Standard Model of strong and electroweak interactions [1] is nowadays one of the most established theories in contemporary particle physics. The first direct experimental verifications of the theory have been obtained by the observation of the neutral weak interaction, propagated by weak bosons, in 1973 [2]. The Standard Model predictions were further confirmed with the discovery of charged and neutral weak bosons by UA1 and UA2 experiments in 1983 [3]. However, high precision measurements of the parameters of the Standard Model as well as confirmations of many of its predictions have been made possible only six years later, by the construction of the Large Electron Positron Collider (LEP) in the European Laboratory for Particle Physics (CERN) near Geneva in Switzerland. LEP began operation in July 1989. The designed energy of the collider allowed a copious production of the neutral weak boson Z^0 , one of the carriers of the electroweak interaction. The study of the Z^0 production and decay properties at LEP confirmed the Standard Model to a yet unsurpassed precision.

An important ingredient of the Standard Model is the unitary Cabbibo-Kobayashi-Maskawa (CKM) matrix [4]. Nine elements of this matrix describe the strength of the couplings between the

quarks and the charged weak bosons $W^\pm$ and must be determined experimentally. From the three individual elements of the CKM matrix describing the couplings of a bottom (b) quark, V_{ub}, V_{cb}, and V_{tb}, the first two can be accessed through the measurements of decay properties of the hadrons containing the b quark. For the extraction of these elements from the measurements of inclusive and exclusive branching ratios of B mesons [5] an accurate knowledge of their lifetimes is required. Since around 22% of the quark-antiquark pairs produced in Z^0 decays are $b\bar{b}$ pairs [6], LEP is also a very convenient apparatus to study hadron systems with the b quark constituents.

The physics of b quarks has been explored already before the construction of LEP at the e^+e^- storage rings. Advantages of the LEP environment for the b-physics studies arise from a higher available energy taken by the b-hadrons. This results in measurable decay lengths of these particles and hence in a possibility of lifetime evaluations. Due to the higher available energy also a whole spectrum of b-hadron species is produced in the Z^0 decays. At LEP for the first time one can reconstruct B_s^0 mesons and measure the lifetime of Λ_b baryons. A study of the differences in decay properties of individual species of the b-hadrons can give some insight into the importance of the specific processes involved in the decays.

The present work describes a measurement of the B_s^0 meson lifetime. This quantity is known with the lowest precision among the lifetimes of the three different types of B mesons: B_s^0 , B^+ and B_d^0 [1]. Since the B_s^0 meson existence was experimentally verified only a few years ago its decays have not yet been studied to a great ex-

---

[1] The symbol B_s^0 is used to describe the meson composed of a $\bar{b}$ and an s quark. B^+ and B_d^0 stand for the $\bar{b}u$ and $\bar{b}d$ meson respectively. Unless explicitly indicated otherwise the corresponding statements for the charge conjugate states are always implied.

tent. Apart from the reasons given above, the determination of the lifetime is important also for the future extraction of the partial decay widths of strange B mesons from the measured branching fractions. Probably an even more important motivation for the lifetime measurement is its indispensability for the study of the neutral B meson oscillations, one of the challenges of the b-quark physics.

The lifetime measurement was performed on two samples of semileptonic B_s^0 decays, obtained by using different reconstructed final states of the B_s^0 decay products. The two samples differed in statistical power as well as in purity of the B_s^0 meson content.

The first part of this work gives a short phenomenological introduction of the production and the decay of B_s^0 mesons at LEP. The specifics of the experimental setup with an emphasis on the Delphi spectrometer sub-detectors, used in the analysis, is described in the second part. The third part consists of two chapters, each of them detailing the performed data analysis of the two studied inclusive B_s^0 decay channels. Finally, in part four, the results are combined and conclusions are drawn.

Chapter 2

Production and Decay of B_S^0 Mesons at LEP

2.1 Production of B_S^0 Mesons in Z^0 Decays

The annihilation of an electron and a positron resulting in a fermion-antifermion pair may proceed through a photon or a neutral weak boson exchange. The corresponding Feynman diagrams are shown in figure 2.1.

$$a) \qquad\qquad\qquad b)$$
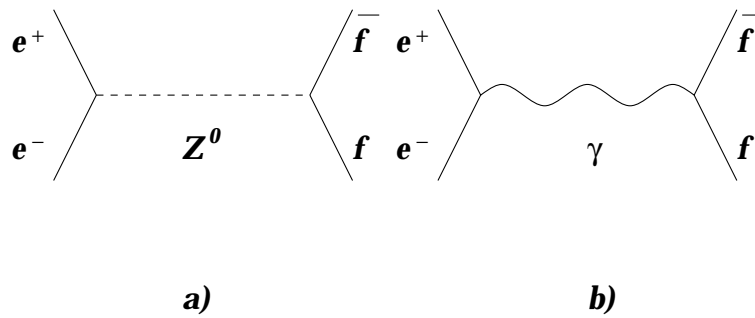
Figure 2.1: Feynman diagrams for the annihilation of an electron and a positron into a fermion-antifermion pair through the exchange of a) a neutral weak boson and b) a photon.

The total cross-section for such a process at the centre-of-mass energy $\sqrt{s}$ is [1] [7]

$$
\begin{aligned}
\sigma(e^+e^- \to f\bar{f}) \;=\; & N_f^c f_{QCD} \left[k_f^v \frac{4\pi\alpha^2}{3s} Q_f^2 \right. + \\
& + k_f^v \frac{G_F \alpha}{3\sqrt{2}} Q_f v_e v_f \frac{M_Z^2(M_Z^2 - s)}{(s - M_Z^2)^2 + s^2 \frac{\Gamma_Z^2}{M_Z^2}} + \\
& \left. + \frac{G_F^2}{96\pi}(v_e^2 + a_e^2)(k_f^v v_f^2 + k_f^a a_f^2) \frac{M_Z^4 s}{(s - M_Z^2)^2 + s^2 \frac{\Gamma_Z^2}{M_Z^2}} \right] .
\end{aligned}
$$

$$(2.1)$$

Q_f is the charge of the final fermion in units of e_0 and N_c^f is the number of colours (3 for quarks and 1 for leptons). G_F is the Fermi constant that is most accurately obtained from the measurements of the muon lifetime [5] and α is the fine-structure constant. The fermion axial and vector coupling constants to the Z^0 boson are

$$
\begin{aligned}
v_f &= 2T_{3f} - 4Q_f \sin^2\theta_w \\
a_f &= 2T_{3f} .
\end{aligned}
$$

$$(2.2)$$

T_{3f} represents the third component of the weak isospin for the left-handed part of fermions (+1/2 for neutrinos and uplike quarks and -1/2 for massive leptons and downlike quarks). M_Z and Γ_Z are the mass and the width of the Z^0 boson and θ_w is the Weinberg angle. Factors $k_f^{v,a}$ equal unity in the limit of massless fermions:

$$
\begin{aligned}
k_f^v &= \beta \frac{3 - \beta^2}{2} \\
k_f^a &= \beta^3 \\
\beta &= \sqrt{1 - \frac{4m_f^2}{s}} .
\end{aligned}
$$

$$(2.3)$$

---

[1] Throughout this chapter the natural system of units is used with $\hbar = c = 1$. Hence a decay width is given in units of $[\Gamma]$ =GeV and time in units of $[t]$ =GeV^{-1}.

In addition to the tree level Feynman diagrams of figure 2.1 one should consider also higher order processes involving the radiation of photons and gluons from the fermion lines and electroweak loop corrections to the vertices and propagators [7] [8]. While the electroweak corrections are absorbed by the use of the Fermi constant in the expression (2.1) and in a small shift of the $\sin^2 \theta_W$, the lowest-order corrections due to the gluon radiation are described by

$$f_{QCD} = \left\{ \begin{array}{c} 1; \text{ leptons} \\ 1 + \frac{\alpha_s(M_Z^2)}{\pi}; \text{ quarks} \end{array} \right\} \tag{2.4}$$

where $\alpha_s(M_Z^2)$ is the strong interaction coupling constant.

The cross-section of equation (2.1) is in the vicinity of the Z^0 pole completely dominated by the third term, arising from the exchange of the neutral weak boson. The annihilation into the photon described by the first term of equation (2.1) as well as the interference term represent only a small correction to the overall cross-section. For example, the cross-section for the e$^+$e$^-$ annihilation into a $\mu^+\mu^-$ pair via the exchange of the Z^0 at $s = M_Z^2$ is

$$
\begin{aligned}
\sigma_{NC}(\text{e}^+\text{e}^- \to \mu^+\mu^-) &= \\
&= \frac{G_F^2 M_Z^4}{24\pi\Gamma_Z^2} \left(1 - 4\sin^2\theta_w + 8\sin^4\theta_w\right)^2 \approx \\
&\approx 2 \text{ nb},
\end{aligned}
\tag{2.5}
$$

while the cross-section for the same process proceeding through the exchange of the photon amounts only to

$$\sigma_{QED}(\text{e}^+\text{e}^- \to \mu^+\mu^-) = \frac{4\pi\alpha^2}{3M_Z^2} \approx 12 \text{ pb}. \tag{2.6}$$

The actual measured cross-sections for the above processes are lower than the ones quoted in equations (2.5) and (2.6). This is the result of large initial state radiation effects which were not

taken into account in the evaluation of the cross-section formulae. The probability for emission of real photons by the colliding electrons or positrons is described by the radiation function $\mathcal{H}(s, s')$ [7] and the cross-section including the hard photon initial state radiation is obtained from

$$\sigma(s) = \int_{s_{min}}^{s} \mathcal{H}(s, s')\sigma^0(s')ds' \, . \tag{2.7}$$

The function $\mathcal{H}(s, s')$ describes the probability that the initial electron and positron with the centre-of-mass energy $\sqrt{s}$ radiate one or several photons, which reduce the available annihilation energy to $\sqrt{s'}$. The effect of this correction is a decrease of the original cross-section of equation (2.1) for approximately 30%. However, since in the ratios of the cross sections these corrections largely cancel [7], the above estimations of σ_{NC} and σ_{QED} are adequate to gain an insight into the significance of different physical processes involved in the f$\bar{\text{f}}$ production in the Z^0 decays.

When evaluating the cross-section for the e^+e^- annihilation into a pair of bottom quarks one should take into account also the Z^{0}b$\bar{\text{b}}$ vertex corrections, arising from possible loops involving the top quarks and the Higgs boson [9] [7]. The contributions of such processes are negligible for lighter quarks because of the smallness of relevant CKM matrix elements and of the Yukawa couplings between the Higgs boson and the quarks. The decay width and the relative rate of Z^0 decays into the bottom quark pairs were measured to be [6]:

$$\Gamma(\text{Z}^0) = (2496.3 \pm 3.2) \, MeV$$
$$\Gamma(\text{Z}^0 \to \text{q}\bar{\text{q}}) = (1740.7 \pm 5.9) \, MeV$$
$$R_\text{b} \equiv \frac{\Gamma(\text{Z}^0 \to \text{b}\bar{\text{b}})}{\Gamma(\text{Z}^0 \to \text{q}\bar{\text{q}})} = 0.2219 \pm 0.0017 \, . \tag{2.8}$$

In the process of hadronization the original pair of quarks, arising from the Z^0 decay and moving in the opposite direction with an energy $E_q \approx \sqrt{s}/2$, gradually degrades in energy by producing additional q$\overline{\text{q}}$ pairs. They form colourless hadrons which are stable or undergo possible secondary decays.

During the last two decades a large number of the hadronization models has been developed. The most important ingredient of such models are the fragmentation functions $D_q^h(z)$, giving the probability density for observing a hadron of type h produced in the fragmentation of the original quark of type q and carrying the fraction z of the original quark momentum. In the most widely used string model of hadronization [10] the production of additional q$\overline{\text{q}}$ pairs is a consequence of the strong force, of asymptotically constant strength, acting between any quark-antiquark pair. The basic principle of the model is the iterative principle [11]. Let q$_0$ be the originally produced quark and $\overline{\text{q}}_1$ one of the first pair of quarks produced in the strong field. The iterative principle states that the remnant of the jet, after the removal of the meson formed from the q$_0$ and $\overline{\text{q}}_1$, looks exactly the same as the original jet apart from the lower remaining momentum. Thus the remnant jet hadronizes exactly as a down scaled version of the original one.

Since the momentum of the final hadrons must match the momentum of the original quark, fragmentation functions should satisfy the relation [12]

$$\sum_h \int_0^1 zD_q^h(z)dz \; = \; 1 \;, \tag{2.9}$$

where the sum runs over all the hadrons produced in the process of hadronization. The number of the produced hadrons follows from the sum of probabilities for producing a hadron from differ-

ent quark flavours available at a certain momentum:

$$\sum_q \int_{z_{min}}^{1} [D_q^h(z) + D_{\bar{q}}^h(z)]dz \;=\; n_h \;.$$ (2.10)

$z_{min} = 2M_h/\sqrt{s}$ is the threshold invariant mass fraction for the production of a hadron with mass M_h. For light quark (q= u,d,s) jets the hadronization is usually described by the fragmentation functions of the form [12]

$$D_q^h(z) \propto \frac{(1-z)^2}{z} \;.$$ (2.11)

By inserting this dependence into (2.10) one can easily conclude that the multiplicity of hadrons depends logarithmically on the centre-of- mass energy:

$$n_h \propto \ln \frac{\sqrt{s}}{2M_h} \;.$$ (2.12)

From the kinematical considerations another form of fragmentation functions was proposed for the hadronization of jets induced by heavier quarks (Q=b,c) [13]:

$$D_Q^h \propto \frac{1}{z\left[1 - (\frac{1}{z}) - \frac{\epsilon_Q}{(1-z)}\right]^2} \;.$$ (2.13)

The parameter ϵ_Q is of the order of the ratio of constituent quark masses m_q^2/m_Q^2.

The shape of this Peterson fragmentation function is plotted in figure 2.2 for b and c quarks, taking the value of 350 MeV for a light quark mass and 1.6 GeV and 5.0 GeV for c and b quark masses respectively [5]. The ansatz (2.13) is in agreement with the experimentally measured momentum distributions of heavy mesons.

Through the process of hadronization the quarks arising from the Z^0 decay are transformed into jets of observable hadrons. In the present work we will focus on the $Z^0 \to b\bar{b}$ decays, followed by the hadronization of b quarks into the B_s^0 mesons, and especially on the subsequent decays of the formed mesons.
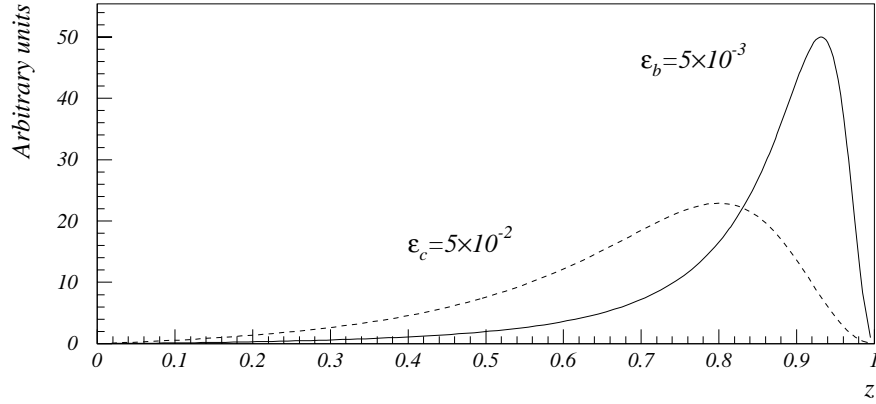
Figure 2.2: The dependence of the Peterson fragmentation function on the momentum fraction z. The parameters ϵ_Q are in the ratio of $1/10$, which is approximately the square of the ratio of heavy quark masses.

2.2 B$_\text{S}^0$ Meson Decays

2.2.1 Spectator Model

The most frequent decay of the B$_\text{S}^0$ meson, composed of the $\overline{\text{b}}$ and s quark, is on the parton level pictured by the Feynman diagram of figure 2.3.

The decay proceeds through the charged current interaction propagated by the weak charged bosons W$^\pm$. The available final states include hadronic modes, where the W$^+$ couples to the u$\overline{\text{d}}$, c$\overline{\text{s}}$, u$\overline{\text{s}}$ or c$\overline{\text{d}}$ pair, and semileptonic modes with lepton pairs $\ell^+ \nu_\ell$. In the framework of the Standard Model the matrix element for the process of figure 2.3 is written as

$$\mathcal{M} = -\frac{G_F}{\sqrt{2}} V_{\text{q}_3\text{b}} \left[\overline{v}_\text{b} \gamma^\mu (1 - \gamma_5) v_{\text{q}_3} \right] V_{\text{q}_1\text{q}_2} \left[\overline{u}_{\text{q}_1} \gamma_\mu (1 - \gamma_5) v_{\text{q}_2} \right]$$

(2.14)

for hadronic decays. For semileptonic decays the second term is

$$q_1 = u, c$$
$$\overline{q}_2 = \overline{d}, \overline{s}$$
$$l^+ = e^+, \mu^+, \tau^+$$
$$\overline{q}_3 = \overline{c}, \overline{u}$$
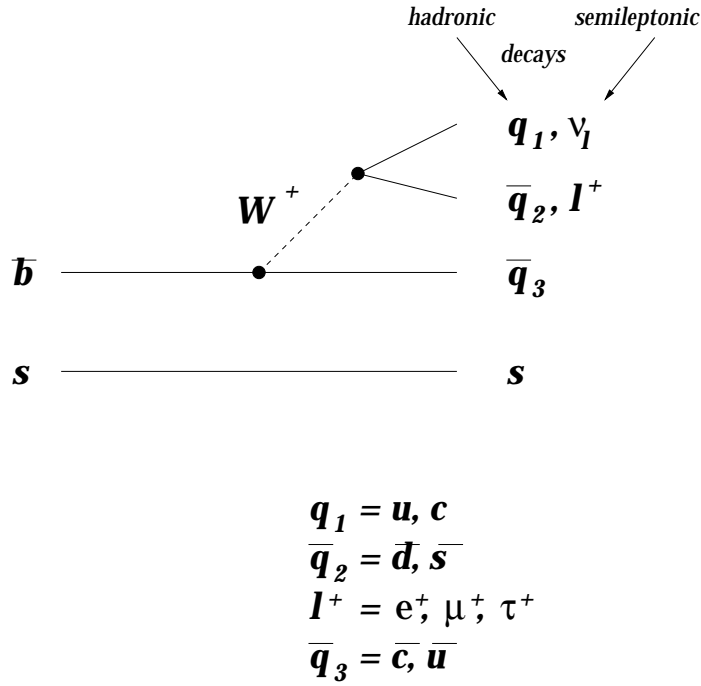
Figure 2.3: The Feynman diagram of the B$_\text{s}^0$ decay.

replaced by the leptonic current and the matrix element reads

$$\mathcal{M} = -\frac{G_F}{\sqrt{2}} V_{\text{q3b}} \left[\overline{v}_\text{b} \gamma^\mu (1 - \gamma_5) v_{\text{q}_3} \right] \left[\overline{u}_{\nu_\ell} \gamma^\mu (1 - \gamma_5) v_\ell \right]$$

$$(2.15)$$

with u_f, v_f representing the particle and anti-particle spinors of fermion f. The coupling strength of the b quark to the c or u quark is given by the corresponding elements V_{q3b} of the CKM matrix. Since the ratio $|V_{\text{ub}}/V_{\text{cb}}|$ was measured to be 0.08 ± 0.02 [5] the b$\rightarrow$u transitions represent a negligible part of the total decay width of the B$_\text{s}^0$ meson. The second CKM matrix factor $V_{\text{q}_1\text{q}_2}$ influences the relative proportion of different hadronic final states. Magnitudes of $|V_{\text{us}}/V_{\text{ud}}|$ and $|V_{\text{cd}}/V_{\text{cs}}|$ are similar and amount to approximately 20% [5]. Using this value one can conclude that the decays of the B$_\text{s}^0$ meson resulting in u$\overline{\text{s}}$ or c$\overline{\text{d}}$ pairs are suppressed by a factor of

~ 20 with regard to the decays into $u\overline{d}$ or $c\overline{s}$ pairs.

The above calculation completely neglects the influence of the s quark accompanying the $\overline{b}$ quark in the B$_\text{s}^0$ meson. Such approximation, known as the spectator model, leads to the total decay width analogous to the decay width for the muon decay $\mu^+ \rightarrow e^+\nu_e\overline{\nu}_\mu$. Hence the decay width of any B meson would equal to

$$\Gamma(b \rightarrow \overline{c}q_1\overline{q}_2) = 3\frac{G_F^2}{192\pi^3}m_b^5|V_{cb}|^2|V_{q_1q_2}|^2I(\frac{m_c}{m_b}, x_2, x_1) \ .$$
(2.16)

Finite masses of the final state quarks are accounted for by the function $I(x_3, x_2, x_1)$ [14], where $x_i = m_i/m_b$ is the fractional mass of the quark q$_i$. If $x_i = 0$, the phase space function is just $I(0, 0, 0) = 1$ and the relation (2.16) reduces to the well known formula for the muon decay width [12], apart from the factor 3 which arises because of the quark colours. To take into account the mass of the c quark and neglecting masses of the light quarks in the $\overline{b} \rightarrow \overline{c}u\overline{d}$ decay, one needs the relation [14]

$$I(x, 0, 0) = 1 - 8x^2 + 8x^6 - x^8 - 24x^4 \ln x \ .$$
(2.17)

Assuming the values of $m_c = 1.6$ GeV/c^2 and $m_b = 5$ GeV/c^2 [5] and by the use of the functional form of $I(x, 0, x)$ given in [14], one can see that due to the phase space limitations the decay $\overline{b} \rightarrow \overline{c}c\overline{s}$ is suppressed with regard to the $\overline{c}u\overline{d}$ decay by a factor of approximately 3 to 4. The semileptonic decay width has the same form as the hadronic width apart from the colour factor and the CKM matrix element $V_{q_1q_2}$. The effect of the muon and electron masses is negligible.

The total B decay width is obtained by summing all partial decay widths. In the spectator model the total decay width of B

mesons is thus

$$\frac{1}{\tau_B^{spec}} = \Gamma_B^{spec} = \frac{G_f^2}{192\pi^3}m_b^5|V_{cb}|^2 I(\frac{m_c}{m_b},0,0)[5+3g_{cc}+g_{c\tau}] \, . \tag{2.18}$$

In the derivation of the total decay width we assumed the value of the CKM matrix elements V_{cs} and V_{ud} to be 1. The g_{cc} and $g_{c\tau}$ are the relative phase space suppressions of the decays with two charm quarks and with one charm quark and the τ lepton in the final state respectively, compared to the decays into a single charm quark final state. By using the above quoted masses of the quarks and the mass of the τ lepton the numerical values are $g_{cc} \approx 0.31$ and $g_{c\tau} \approx 0.23$.

2.2.2   QCD Corrections

The quarks in the diagram 2.3 can emit real or virtual gluons. The corresponding Feynman diagrams at the lowest order of α_s are sketched in figure 2.4. While the processes in 2.4 a) and c) affect only hadronic decays, the processes in 2.4 b) contribute also to semileptonic B meson decays.

The effect of the real radiated gluons, which further materialise into quarks, is the multiplicative correction factor for the semileptonic and hadronic decay width [15]:

$$\begin{aligned} f_{QCD}^{sel} &= 1 - \frac{2\alpha_s(m_b^2)}{3\pi}(\pi^2 - \frac{25}{4}) \\ f_{QCD}^{had} &= 1 + \frac{2\alpha_s(m_b^2)}{3\pi}0.6 \, . \end{aligned} \tag{2.19}$$

The QCD mechanisms that affect only the hadronic decays and are the result of soft gluon exchange between the quarks are taken into account by the correction of the matrix element of (2.14). The summation of different diagrams involving gluonic loops generates a new amplitude, which must be added to the usual charged
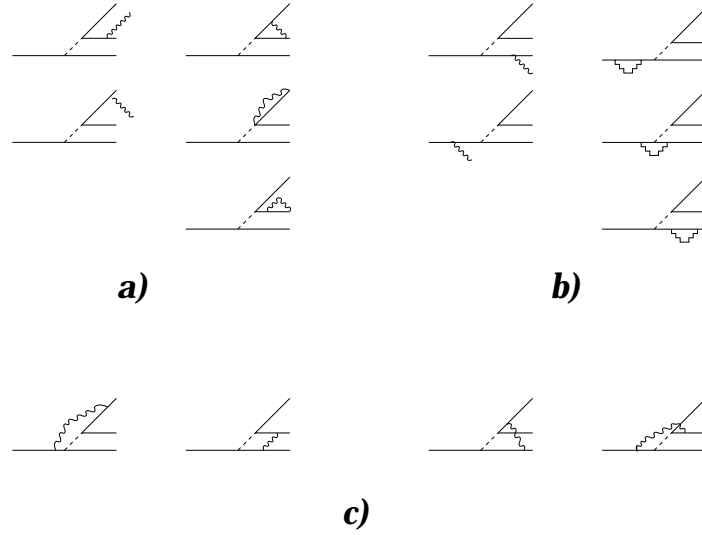
Figure 2.4: Different processes contributing to the QCD corrections of the spectator B meson decay width.

current amplitude. The $(\overline{v}_b v_{q_3})_{V-A}(\overline{u}_{q1} v_{q_2})_{V-A}$ form of (2.14) is in the QCD induced amplitude replaced by $(\overline{v}_b v_{q_2})_{V-A}(\overline{u}_{q1} v_{q_3})_{V-A}$, with the subscript $V-A$ denoting $\gamma^\mu(1-\gamma_5)$ operator between the spinors [16]. The additional amplitude may be represented by the diagram plotted in figure 2.5 a) together with the original charged current interaction. Despite the similarity to the neutral current interaction the new amplitude is just an effective description of the corrections due to the emission of gluons.

The two amplitudes must be summed with the relative strengths given by $(c_+ + c_-)/2$ and $(c_+ - c_-)/2$. The coefficients c_+ and c_- are calculated in the QCD framework to be [16]:

$$c_\pm = \left[\frac{\alpha_s(M_W^2)}{\alpha_s(m_b^2)}\right]^{\gamma_\pm}$$

$$\gamma_+ = \frac{6}{33-2N_f} = -\frac{1}{2}\gamma_- . \qquad (2.20)$$

N_f is the number of available quark flavours which for the B decays
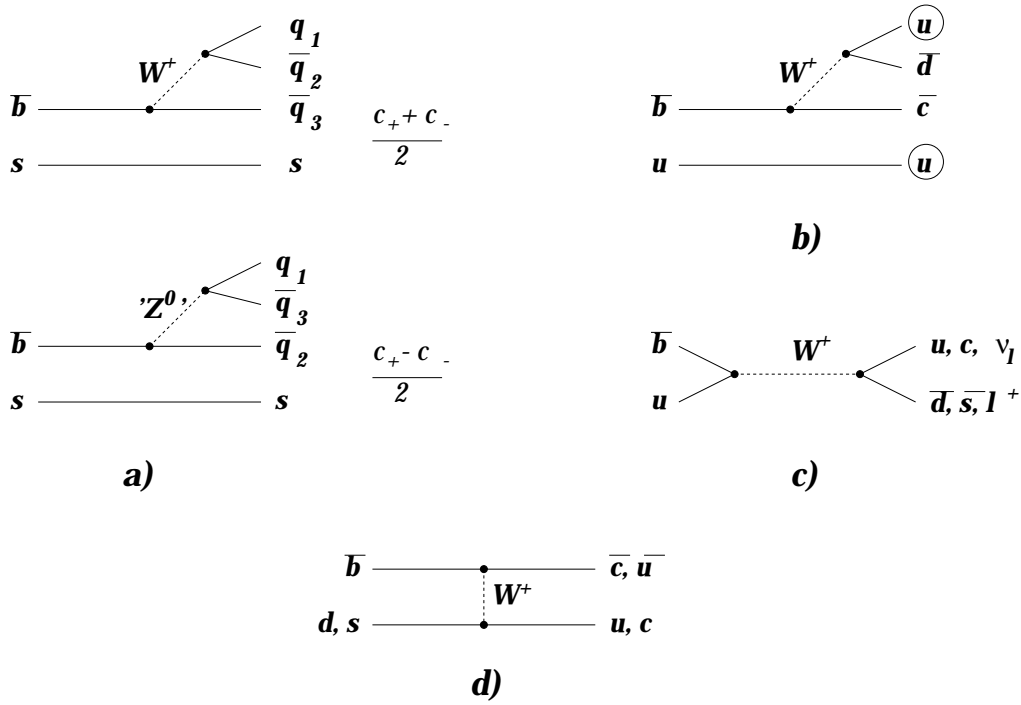
Figure 2.5: a) The charged current interaction responsible for the B decay and an effective neutral current interaction used to describe the QCD corrections to the decay width. The relative strengths of the two amplitudes are indicated at the side. b) The B^+ decay with the two identical u quarks in the final state leading to the interference corrections of the decay width. c) The annihilation diagram for the B^+ decay. d) The exchange processes contributing to decays of the neutral B mesons.

is four. Numerically the coefficients amount to $c_+ \approx 0.84$ and $c_- \approx 1.42$ [17].

The corrected matrix element for the hadronic B decay is

$$\mathcal{M} = -\frac{G_F}{\sqrt{2}} V_{q_3 b} V_{q_1 q_2} \left[\left(\frac{c_+ + c_-}{2} \right) \overline{v}_b \gamma^\mu (1 - \gamma_5) v_{q_3} \overline{u}_{q_1} \gamma_\mu (1 - \gamma_5) v_{q_2} \right. +$$
$$\left. + \left(\frac{c_+ - c_-}{2} \right) \overline{v}_b \gamma^\mu (1 - \gamma_5) v_{q_2} \overline{u}_{q_1} \gamma_\mu (1 - \gamma_5) v_{q_3} \right]$$
$$(2.21)$$

By squaring the matrix element (2.21) and including the correction due to the hard gluon radiation (2.19) one obtains the decay

width

$$\Gamma(B_{d,s}^0 \rightarrow \overline{c} q_1 \overline{q}_2 s(d)) =$$
$$= \frac{G_F^2}{192\pi^3} m_b^5 |V_{cb}|^2 |V_{q_1 q_2}|^2 (2c_+^2 + c_-^2) I(\frac{m_c}{m_b}, x_2, x_1) f_{QCD}^{had} \,.$$
(2.22)

By comparing equations (2.22) and (2.16) and by using the value $\alpha_s(m_b^2) = 0.21$ [5] one can see that the effect of described QCD corrections is an enhancement of the hadronic decay width by approximately 17%. At the same time these corrections reduce the semileptonic decay width by almost the same relative amount.

In the relation (2.22) we used an explicit notation for the $B_{d,s}^0$ mesons. In the case of the charged B mesons another non-spectator effect takes place which will be described in the following section.

2.2.3 Interference Corrections

A possible decay of the charged B^+ meson composed of the $\overline{b}u$ pair is presented in figure 2.5 b). The noticeable difference to decays of the B_d^0 and B_s^0 mesons is the appearance of two identical fermions (u quarks) in the final state. In accordance with the Fermi statistics the wave function of the final state should thus be antisymmetrized with regard to the interchange of the two identical particles. This leads to [15] a modified expression (2.22) in the case of the charged B meson decay:

$$\Gamma(B^+ \rightarrow \overline{c}u\overline{d}u) =$$
$$= \frac{G_F^2}{192\pi^3} m_b^5 |V_{cb}|^2 |V_{ud}|^2 \left[(2c_+^2 + c_-^2) + \right.$$
$$\left. + 16\pi^2 \frac{f_B^2}{m_b^2} (2c_+^2 - c_-^2) \right] I(\frac{m_c}{m_b}, x_2, x_1) f_{QCD}^{had} \,.$$
(2.23)

The amount of the interference effect is given by the second term of (2.23) and controlled by the value of the B meson decay constant

f_B.

From equation (2.23) one can note that in the absence of QCD corrections, i.e. with $c_+ = c_- = 1$, the interference would be constructive. It would result in a shortened lifetime of the $B^\pm$ with regard to the lifetime of a neutral B meson. However, considering the values of parameters c_+ and c_- given above, the interference effect prolongs the lifetime of charged B mesons with regard to the lifetime of neutral B mesons.

2.2.4   Annihilation and Exchange Corrections

The Feynman diagram of figure 2.3 is not the only process that can contribute to the decay width of B mesons. The annihilation process illustrated in figure 2.5 c) is also possible in the $B^\pm$ decay. For neutral mesons the possibility of the $W^\pm$ exchange leads to the processes shown in figure 2.5 d).

The relative contribution of these processes can be inferred from the following consideration [15]. The decay width connected to the annihilation of the $\overline{b}u$ pair in the B^+ meson is an analogy of the decay rate for the pion decay [9] and is proportional to $f_B^2 m_b m_q^2$, with m_q being the mass of the heaviest final state quark. The same is valid for the exchange processes in neutral B decays. The annihilation diagram involves the coupling of the initial $\overline{b}$ and u quark which results in the $|V_{ub}|^2$ factor in the decay rate. On the other hand the exchange diagrams are Cabbibo allowed ($|V_{ud}| \approx |V_{cs}| \approx 1$) but require the matching of the final quark colours and hence obtain an additional factor of $1/9$.

A detailed calculation of numerical factors [15] gives the relative suppression of the described processes with regard to the

spectator width as

$$
\begin{aligned}
\frac{\Gamma^{ann}}{\Gamma^{spec}} &= 24\pi^2 \, \frac{|V_{ub}|^2}{|V_{cb}|^2} \, \frac{f_B^2}{m_b^2} \, \frac{m_q^2}{m_b^2} \\
\frac{\Gamma^{exc}}{\Gamma^{spec}} &= 24\pi^2 \, \frac{1}{9} \, \frac{f_B^2}{m_b^2} \, \frac{m_q^2}{m_b^2} \; .
\end{aligned}
\tag{2.24}
$$

The relative suppression due to the required constituent over-lap described by the factor f_B^2/m_b^2 in (2.24), due to the helicity suppression accounted for by m_q^2/m_b^2, and due to the colour or Cabbibo suppressions reflecting in $1/9$ and $|V_{ub}|^2/|V_{cb}|^2$ respectively, somewhat competes with the larger available phase space resulting in the factor $24\pi^2$. Numerical evaluation however proves that the contribution of annihilation and exchange processes in B meson decays is negligible, not only when compared to the spectator decay width but also when compared to the already small contribution from the interference effect.

2.2.5   Phenomenological Expectations for the B Meson Lifetimes

According to the arguments nicely presented in [16] the differences between the individual species of hadrons containing the same heavy quark Q are expected to decrease with the increasing mass of the heavy constituent. As the mass of the heavy quark Q exceeds the mass of the charged weak boson, the decay time of the quark becomes shorter than the typical hadronization time. Such a quark decays into a real weak boson before hadronization and hence no hadrons composed of the quark Q can be formed. Due to a finite width of the W boson the overpassing of its mass proceeds in a continuous manner. As the mass of the Q approaches the mass of the W one can thus anticipate a decreasing influence of the spectator quark on the lifetime of a hadron. Lifetimes of mesons, containing

the heavy quark, approach one another and the τ_Q obtained in the spectator model.

The previous sections described the quantification of this principle. Different non-spectator effects contribute to the lifetime differences among the B mesons with the leading relative factor f_B^2/m_b^2 with regard to the spectator lifetime. The same qualitative picture as in the B meson sector can be applied to the D mesons, composed of a c quark. The non-spectator effects in the B sector can thus be expressed by the measured lifetime differences between the different species of D mesons:

$$\frac{\tau_{B^+} - \tau_{B^0}}{\tau_{B^0}} \sim \frac{f_B^2}{f_D^2} \frac{m_c^2}{m_b^2} \frac{\tau_{D^+} - \tau_{D^0}}{\tau_{D^0}} . \qquad (2.25)$$

For the decay constants f_D and f_B values of 230 and 180 MeV respectively can be taken. While the value of f_D corresponds to the measured decay constant of the D$_s^+$ meson in the $\mu^+ \nu_\mu$ decays [18], the f_B is the theoretical expectation given in [19]. From the measured lifetimes of D mesons one would obtain the expected lifetime difference between the charged and the neutral B mesons of the order of 10%.

A somewhat more accurate prediction is achieved by the calculations referred to in previous sections. The corrections to the spectator model should be applied due to the possible radiation and exchange of the gluons between the quarks. The decay width of charged B mesons is affected by the interference effect which prolongs their lifetime. In the decays of neutral B mesons annihilation and exchange processes take place but their effect on the lifetime is negligible. By introducing the estimated corrections to the spectator model decay width, the expected lifetime ratios of

individual B mesons can be summarized as [17]:

$$\frac{\tau_{B^+}}{\tau_{B_d}} \approx 1 + 0.05\left(\frac{f_B}{200MeV}\right)^2$$

$$\overline{\tau}_{B_d} \approx \overline{\tau}_{B_s} . \tag{2.26}$$

The notations $\overline{\tau}_{B_s,B_d}$ denote the average lifetime of the two mass eigenstates in neutral B meson systems.

Part II

Experimental Environment

Chapter 3

Delphi Spectrometer at LEP

3.1   Large Electron Positron Collider

The Large Electron Positron (LEP) collider is operating at the European Particle Physics Laboratory near Geneva. Four bunches of electrons and the same number of positron bunches circulate in a vacuum beam pipe. The beam pipe has almost 27 kilometres in circumference to reduce energy losses due to a synchrotron radiation. Four spectrometers, Aleph, Delphi, Opal and L3, are situated at four out of eight bunch-crossing points on the particles orbit. The map marking the position of CERN and LEP in a vicinity of Geneva is shown in figure 3.1.

The acceleration of particles colliding at LEP is performed in several stages. Electrons from an electron gun and positrons from an electron converter are first accelerated to 600 MeV energy in the two linear accelerators followed by an electron-positron accumulator which injects the particles into the CERN Proton Synchrotron (PS). At the energy of 3.5 GeV particles are passed over from the PS into the CERN Super Proton Synchrotron (SPS). In the SPS electrons and positrons reach 20 GeV, a starting energy for the injection into LEP.
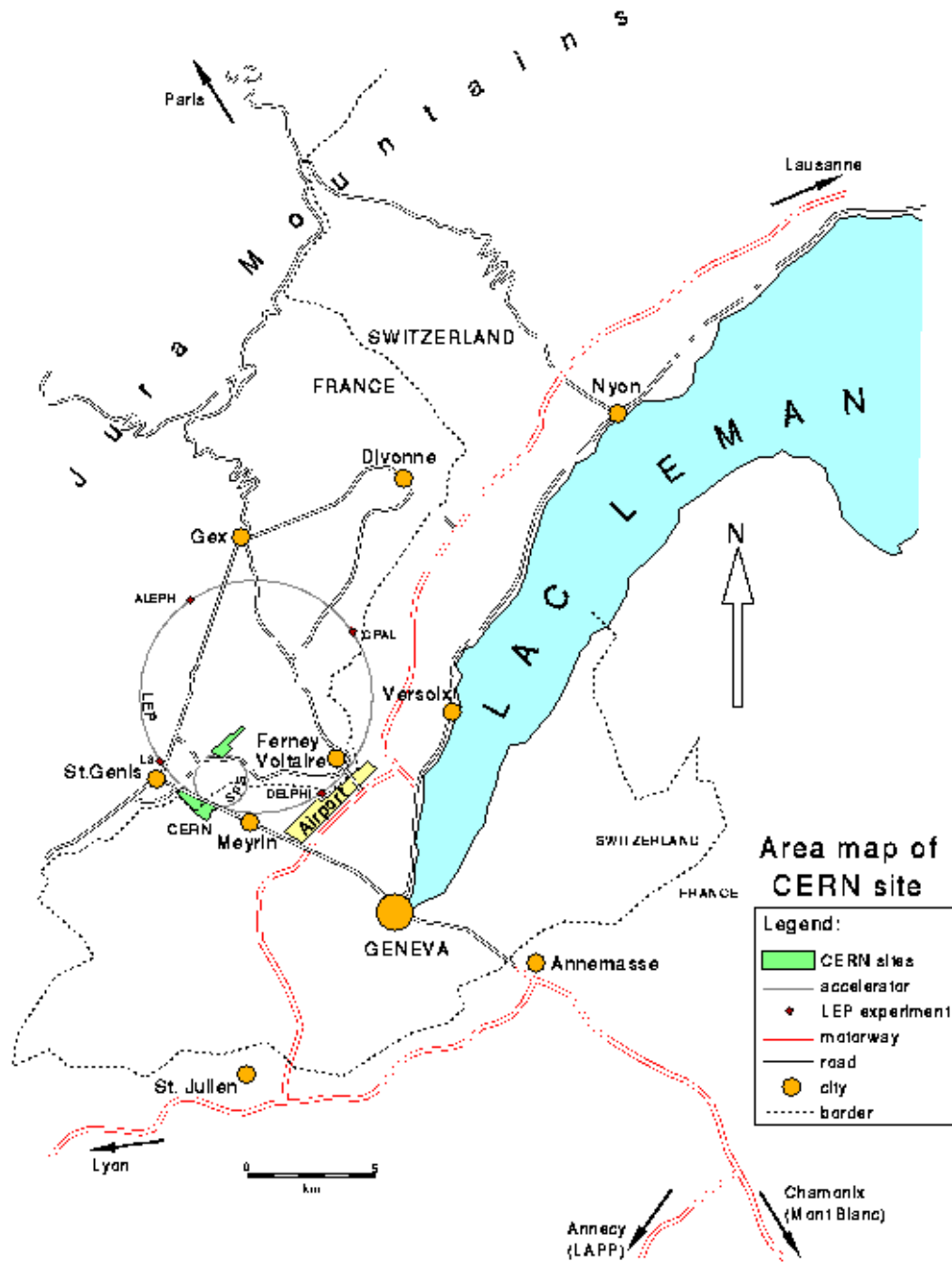
Figure 3.1: Surroundings of Geneva with CERN sites and LEP collider with marked experimental points.

At LEP, electrons and positrons collide at a beam energy of 45.5 GeV [1]. The centre-of-mass energy is thus the same as the mass of the Z^0 vector boson ($M_{Z^0} = (91.1885 \pm 0.0022)$ GeV/c^2 [6]) produced in the collision. By variation of the centre-of-mass energy in an interval of $\delta E \approx 6$ GeV around the Z^0 peak a scanning of the Z^0 lineshape and the measurement of cross-sections for Z^0 decays into a pair of fermions is performed. At LEP luminosity of 1.1×10^{31} cm^{-2}s^{-1} and the peak cross section for the process $e^+e^- \rightarrow Z^0 \rightarrow q\bar{q}$, $\sigma^0_{had} = (41.488 \pm 0.078)$ nb [6], one hadronic Z^0 decay is produced approximately every two seconds.

A typical time of bunch circulating inside LEP is 10 hours, after that the accelerating cycle is repeated. In the running periods from the beginning of 1990 until the end of 1994 the four spectrometers recorded more than 12×10^6 Z^0 decays into $q\bar{q}$ pairs.

3.2 Delphi Spectrometer

Delphi (**DE**tector with **L**epton, **P**hoton and **H**adron **I**dentification) spectrometer is one of the four spectrometers operating at the LEP collider. A collaboration of physicists gathered around the Delphi spectrometer consists of more than 540 scientists from 53 institutes and 22 countries. Eight physicists from the Experimental Particle Physics Department of the Jožef Stefan Institute in Ljubljana are taking part in the collaboration as well.

The spectrometer was designed to identify and accurately track particles produced in Z^0 decays. It is composed of many detectors structured in a cylindric shape, covering most of the solid angle around the electron-positron interaction point. It consists of

---

[1]In October 1995 the collision energy of LEP was raised to 140 GeV and a gradual upgrade of the energy is foreseen until the 1998. The description given here thus corresponds to the LEP collider for data taking periods between 1989 and 1995.

the barrel and two end-caps. A schematic view of the cross-section through the spectrometer is shown in figure 3.2.

Forward Chamber A

Forward RICH

Forward Chamber B

Forward EM Calorimeter

Forward Hadron Calorimeter

Forward Hodoscope

Forward Muon Chambers

Surround Muon Chambers

Barrel Muon Chambers

Barrel Hadron Calorimeter

Scintillators

Superconducting Coil

High Density Projection Chamber

Outer Detector

Barrel RICH

Small Angle Tile Calorimeter

Quadrupole

Very Small Angle Tagger

Beam Pipe

Vertex Detector

Inner Detector

Time Projection Chamber

DELPHI

Figure 3.2: Spectrometer Delphi: the cross-section through the barrel and one of the end-caps.

The spectrometer as well as the entire collider is installed in a tunnel 100 meters below the ground. Both end-caps of 10 m diameter may be independently removed to allow access to specific detector components. The superconducting solenoid produces a uniform magnetic field in the direction of the beam axis. The magnitude of the longitudinal component of the field inside the Time Projection Chamber (see description below) is $B_z = 1.2334 \pm {}^{0.0001}_{0.0010}$ T [20]. The magnitude of the radial component is less than 0.0005 T.

A complete description of the spectrometer may be found in [20]. In the following we will briefly review the most important

properties of detectors relevant to this analysis. We shall use the coordinate system with the z-axis parallel to the beam of electrons. The radial coordinate R is measured from the beam axis and the azimuth angle φ in the plane perpendicular to it. θ is the polar angle with respect to the z-axis.

3.2.1 Tracking Detectors

- Vertex Detector (VD)

  Three concentric layers of silicon microstrip detectors [21] are mounted at the average radii of 6.3, 9 and 11 cm surrounding the beam pipe. The interval of polar angles in which the particle originating from the interaction point crosses all three layers is $44° \leq \theta \leq 136°$. Each shell consists of 24 modules of single-sided silicon strip detectors, with a 10% overlap in φ for a careful internal alignment between the shells. For the 1994 data taking the first and the third layer were equipped with double-sided detectors. The sense strips of these detectors are aligned parallel to the beam axis on one side and in the perpendicular direction on the other side. Such a configuration enables the measurement of the (R, φ) as well as of the z coordinate. The polar angle coverage of the first layer was also increased to $25° \leq \theta \leq 155°$. A schematic view of one half of the second and the third layer of the VD is shown in figure 3.3 a).

  The VD enables high precision measurements of a track position in the vicinity of a primary vertex and improves the particle momentum resolution. It is used to reconstruct secondary vertices of long lived particles and is indispensable for lifetime measurements of particles containing the heavy
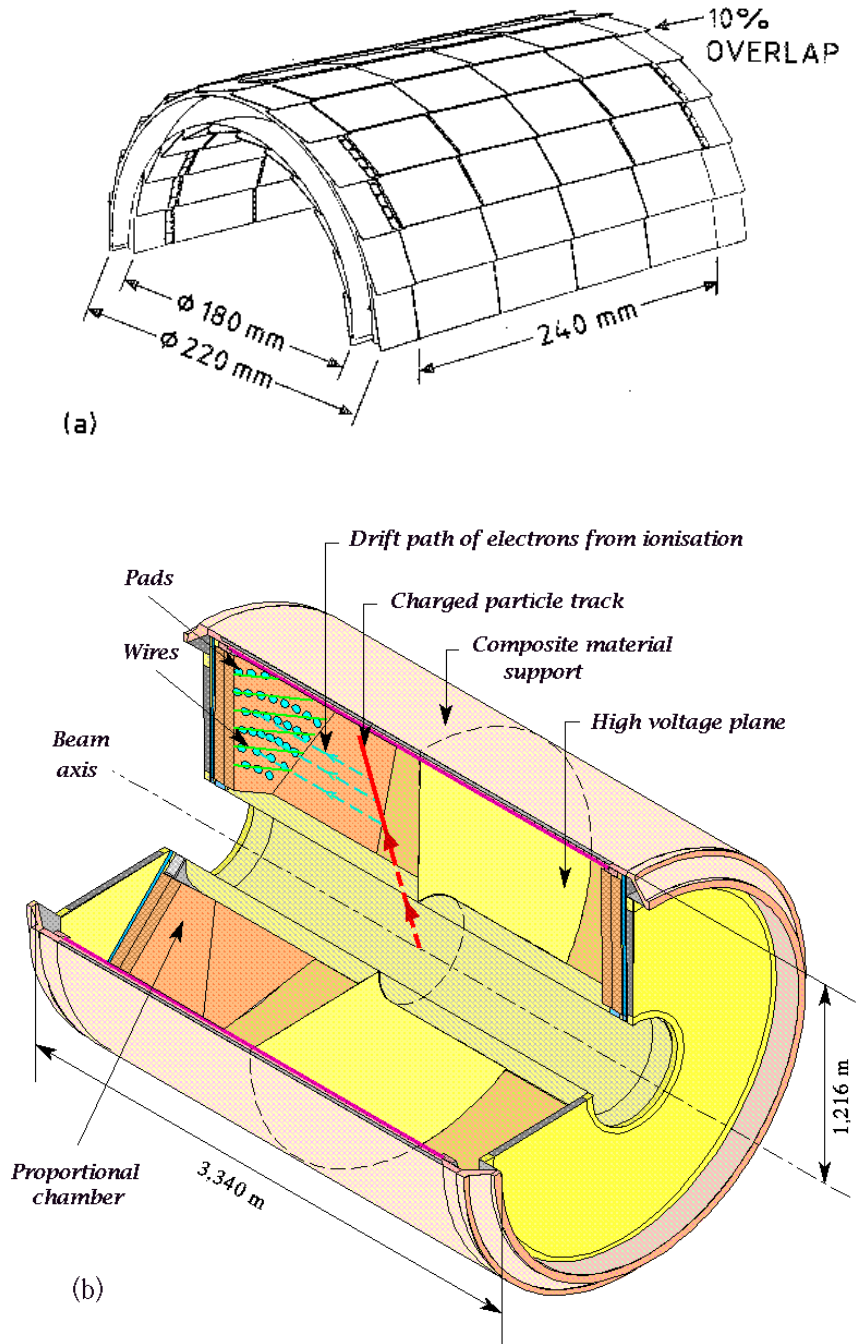
Figure 3.3: a) A schematic view of one half of the second and the third layer of the VD. b) A schematic view of the TPC.

quarks.

Charged particles, crossing the VD, ionize atoms of the semi-conducting material. Coordinates of the tracks are obtained from the division of the charge, released in the semiconductor, among several sense strips of the detector. A single layer of the detector provides a measurement of the track position with a precision of 7.6 μm and approximately 100 μm double track separation in the (R, φ) coordinate, averaged over the polar angle [20]. In the z coordinate single hit precision varies from 9 μm at $\theta = 90°$ to around 30 μm at $\theta = 45°$ [21].

- Inner Detector (ID)

  The detector consists of two concentric layers: the drift chamber giving 24 (R, φ) points per track and 5 cylindrical multi-wire proportional chambers with 192 wires providing the (R, φ) coordinate and 192 cathode strips providing the z coordinate. One quarter of the ID is plotted in figure 3.4 a).

  The detector is mounted at radii between 12 and 28 cm. The geometrical acceptance of drift chambers in θ is 17° to 163°. The (R, φ) coordinate of the track traversing the drift chamber is determined from the measured drift time of electrons from ionization. The achieved single wire resolution in the drift chamber is $\sigma_{R\varphi} = 75 - 125$ μm, depending on the drift distance. The drift time does not provide information on the direction of the drift. These inherent left-right ambiguities of drift chambers are resolved by multi-wire proportional chambers.
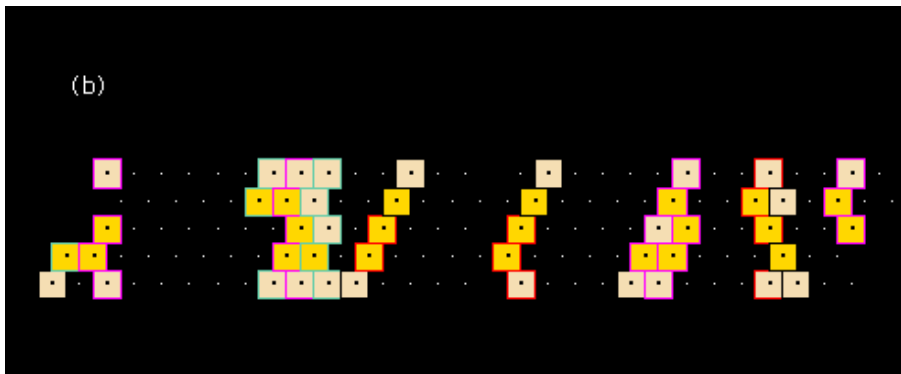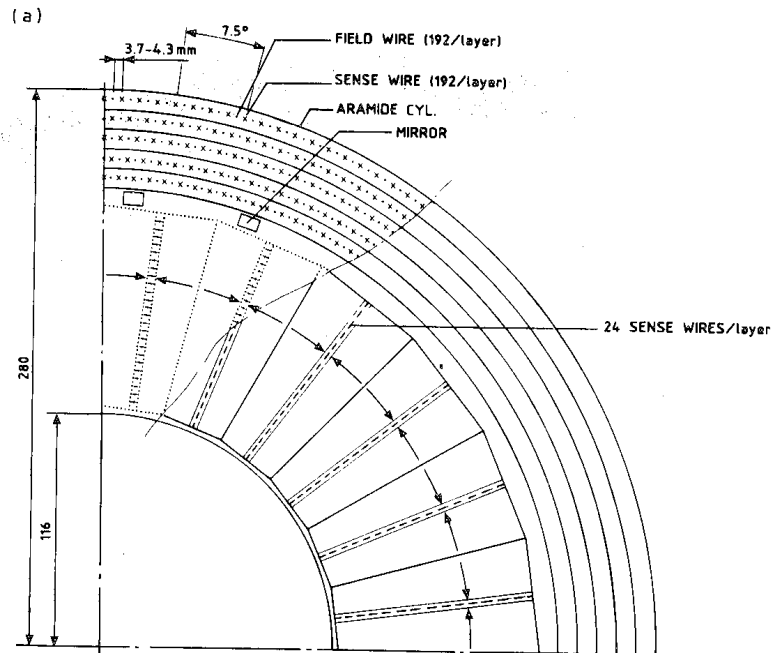
Figure 3.4: a) One quadrant of Inner Detector, each φ module composed of a drift chamber and 5 multi-wire proportional chambers (taken from [20]). b) 5 layers of OD drift tubes shown in (R, φ) projection. Tubes, traversed by charged particles, are shown in colours.

They also provide the z coordinate measurement. The resolution of a single proportional chamber is $\sigma_z = 0.5 - 1.0$ mm [20] [2].

- Time Projection Chamber (TPC)

A schematic view of the TPC is shown in figure 3.3 b). From the TPC response a charged track reconstruction usually starts. The detector provides a 3-dimensional measurement of particle trajectories. Electrons, produced in ionization of gas atoms in the TPC by a charged track, drift in the electric field parallel to the beam axis. From the drift time the z coordinate of the trajectory is reconstructed. Precision of the track position measurement in z direction depends crucially on the accurate knowledge of the electron drift velocity.

At both end-caps of the TPC, drifting electrons enter the multi-wire proportional chambers. Each chamber is divided into 6 sector plates with 192 sense wires and 16 circular pad rows. The induced electric signal on the cathode pads serves for the measurement of the (R, φ) coordinate of the charged track. The granularity of pads determines the spatial resolution of the detector in this coordinate. The pads give up to 16 measurements of the (R, φ) coordinate between $R \approx 35$ cm and $R \approx 111$ cm. If one requires at least 3 pad rows to be hit, the angular acceptance of the TPC is between $\theta = 20°$ and $\theta = 160°$.

The high voltage plane provides an electric field $E = 187$ V/cm [20] resulting in electron drift velocity of $v_d \approx 7$ cm/μs at T=29°C. The spatial resolution for a single pad row (measured

---

[2]Since the beginning of 1995 the polar angle coverage of the ID has been increased to $15° < \theta < 165°$ and the multi-wire proportional chambers have been replaced by straw tube detectors.

for $Z^0 \to \mu^+\mu^-$) is 250 μm in (R, φ) and 880 μm in z [20]. Signals from two tracks can be separated if the distance between the tracks is at least 1 cm.

Beside accurate position measurements the TPC provides also information for particle identification. Each sense wire performs a dE/dx measurement which will be discussed in the section on combined charged particle identification with Delphi.

- Outer Detector (OD)

  The OD completes the tracking in the barrel region. It consists of 24 azimuthal modules, each one containing 145 drift tubes, compounded in 5 layers. Layers of drift tubes are shown in figure 3.4 b). Drift tubes in different layers overlap to give the full azimuthal coverage. The OD considerablly improves the momentum resolution particularly for fast particles.

  Drift tubes are aligned parallel to the beam axis. While all the layers provide the (R, φ) coordinate, three of them measure the z position of a track as well. The z coordinate measurement is obtained by comparing the relative timing of electronic signals at both ends of the drift tube. Drift tubes cover the polar angles from 42° to 138° and are situated at radii between 197 and 206 cm. Single point precisions are $\sigma_{R\varphi}$=110 μm and σ_z=3.5 cm [20].

The combined tracking performance of the VD, ID, TPC and OD can be illustrated with the average momentum resolution for muons from a dimuon decay of the Z^0. The distribution of the inverse momentum can be parametrized with the sum of two Gaussian distributions. The narrower Gaussian, which includes around

92% of events, has a width of [20]

$$\sigma(\frac{1}{p}) = 0.57 \times 10^{-3} \ (\text{GeV/c})^{-1} \ . \tag{3.1}$$

The precision of the momentum evaluation for tracks arising from hadronic Z^0 decays may be obtained by comparison of the reconstructed and simulated momenta in simulated decays of the Z^0. Figure 3.5 [20] shows the relative momentum resolution as a function of polar angle.
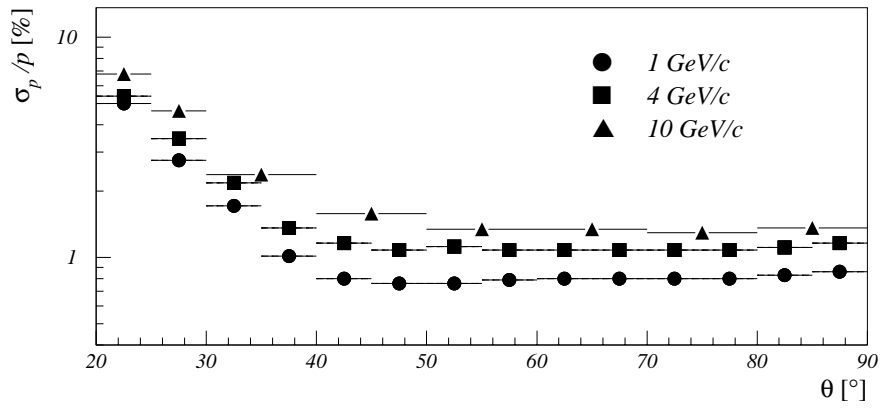
Figure 3.5: Relative precision on the momentum of particles in hadronic Z^0 decays as obtained from simulation (adopted from [20]).

Beside the momentum another important parameter of a track is the impact parameter with respect to the primary vertex, measured in the (R, φ) plane. The performance of the four above-mentioned detectors is expressed with the following expression for the resolution on the impact parameter ϵ [21]:

$$\sigma_\epsilon = \sqrt{20^2 + (\frac{65\text{GeV/c}}{p_t})^2} \ \mu\text{m} \ . \tag{3.2}$$

p_t is the transverse momentum of a particle with respect to the z axis.

3.2.2   Calorimetry

- Electromagnetic Calorimeter (HPC)

  The barrel electromagnetic calorimeter of the Delphi spectrometer is called High Density Projection Chamber (HPC). HPC, as its name suggests, uses a large number of time-projection chambers for calorimetry measurements. The calorimeter is composed of 144 modules, separated into 6 rings along the beam axis. Each ring includes 24 coaxially arranged modules with an inner radius of 208 cm and an outer radius of 260 cm. Polar angle coverage of the HPC is $43° < \theta < 137°$.

  Each module is a time-projection chamber. The gas volume of the chamber is in the radial direction intercepted by 41 lead walls. Electrons and photons, penetrating this high density material of HPC, induce electromagnetic showers. Charged particles from the showers ionize atoms of the gaseous parts of the chamber. Layers of lead, which serve as a converter material, provide also a constant drifting electric field for the electrons from ionization. One end of the module is equipped with a multi-wire proportional chamber. Like in the TPC, charge carriers released in the ionization, drift to the proportional chamber. They induce an electric signal on 128 cathode pads arranged in 9 rows.

  The response of the detector is monitored and calibrated by occasional small admixture of radioactive ^{83}Kr* to the gas of the time-projection chambers [22]. Electrons with an energy of about 40 keV are produced in the decay of ^{83}Kr*. The charge, released by such electrons, is normally collected by a single cathode pad. This enables an equalisation of responses of individual pads to particles with a given energy deposition.

The final energy calibration of HPC is performed with electrons and positrons of precisely known energy, arising from $Z^0 \rightarrow e^+e^-$ decays .

The total thickness of lead layers in each HPC module corresponds to 17.5 radiation lengths in the direction perpendicular to the beam axis [23]. The time-projection method used in the calorimeter enables a measurement of showers, induced by electrons and positrons from $Z^0 \rightarrow e^+e^-$ decays, with a spatial resolution of 1.3-3.1 mm in z, depending on polar angle, and around 0.2° in azimuthal angle φ. The relative energy resolution for these particles is $(6.4 \pm 0.2)\%$ [23]. The precision of energy measurement for lower energy particles is obtained from the decays of neutral pions into two photons. 7% of the photons convert into e^+e^- pairs in front of the TPC and can thus be measured with a high precision. One can use the position and the width of the π^0 invariant mass peak, reconstructed from one converted photon and one photon detected in the HPC, to obtain the resolution on the measured photon energy [20]:

$$\frac{\sigma(E)}{E} = \sqrt{(0.043)^2 + \frac{(0.32)^2 \mathrm{GeV}}{E}} \, . \qquad (3.3)$$

- Hadron Calorimeter (HCAL)

  The barrel HCAL consists of streamer tubes, inserted in 1.8 cm slots between 5.0 cm thick iron plates of the return yoke of the Delphi solenoid. 20 layers of tubes are mounted between $R = 3.20$ m and $R = 4.79$ m. Tubes are grouped in modules. 24 modules cover a full azimuthal range.

  Hadrons, entering the HCAL, strongly interact in the iron plates and produce hadronic showers, which are almost completely

absorbed in the detector. Muons loose energy dominantly through ionization and leave only a fraction of their energy in the calorimeter.

The charge, released by ionization of the gas in streamer tubes, induces a signal on the cathode pads. Each pad covers an angular region of $2.96°$ in θ and $3.75°$ in φ [20]. Pads of five consecutive layers in the radial direction are read out by the same electronic channel [3].

The electronic signal from streamer tubes is independent of the amount of ionization produced by a charged particle. The energy is measured from the number of hits in different tubes, which is of course larger for hadronic showers than for penetrating muons. Calibration is performed using dimuon decays of Z^0 and the total deposited energy in hadronic decays of Z^0.

The calibration of hadronic shower energy is checked by comparing the measured energy of a single pion, arising from $\tau^- \rightarrow \pi^- \nu_\tau$ decays, with momentum of the pion, measured in tracking detectors. The precision of the energy measurement in the hadronic calorimeter is determined to be [20]

$$\frac{\sigma(E)}{E} = \sqrt{(0.21)^2 + \frac{(1.12)^2 \text{GeV}}{E}} \ . \tag{3.4}$$

3.2.3 Charged Particle Identification

- Electron Identification

  Electron identification is performed from two independent pieces of information [24]. The first one relies on the energy deposition of particles in the electromagnetic calorimeter

---

[3]Since the beginning of 1995 a new readout system was implemented in the HCAL. This improves the granularity of the detector by a factor of 5 in the radial and a factor of 3 in the φ direction.

(HPC). In the HPC one uses the ratio of the particle's energy and momentum, directional mismatch between the reconstructed charged track and electromagnetic shower, and the longitudinal profile of the shower to discriminate between electrons and other charged particles. The second piece of information is the dE/dx measurement in the TPC.

Electrons and positrons, unlike other charged particles, are completely absorbed in the HPC. The ratio of the deposited energy and momentum, measured with tracking devices, should thus be close to unity. The measured E/p ratio of a certain track is compared to the one, expected for electrons. The agreement is expressed as a probability for a track being an electron.

Showers produced by particles penetrating the HPC are associated to tracks reconstructed in the TPC. A difference between the reconstructed track and the direction of the associated shower, in z and φ coordinates, enables to exclude showers, produced by neutral particles.

Finally, the expected energy deposition rate dE/dt [25], where t is the shower depth, expressed in units of radiation length, is fitted to the measured energy deposition in the HPC. The quality of the fit, given by a χ^2 probability, can be used to determine whether the shower is of electromagnetic origin.

The second piece of information used in the electron identification is the dE/dx measurement in the TPC. Specific ionization is sampled by 192 anode wires of the TPC. Signals arising from nearby tracks cannot be correctly separated and are not used for the dE/dx measurement. The minimum track distance enabling a separate measurement of dE/dx is around

2 cm [20]. The average energy loss is calculated from 80% of lowest amplitudes of the wire signals in order to reduce the effect of the Landau distribution tail. By requiring at least 30 TPC sense wires to give a signal the relative precision on this truncated mean is found to be 7.4% for particles in hadronic jets [20]. This gives above 2σ separation between electrons and pions with momenta up to 20 GeV/c. Figure 3.6 [20] shows the specific ionization of electrons and their separation from hadrons as a function of particles momenta.

The combination of both measurements yields a classification of electrons with momentum above 2 GeV/c into three categories: loose, standard and tight. They are sorted according to decreasing efficiency and increasing purity of the electron sample. Efficiencies and typical misidentification probabilities of different tags for electrons in hadronic Z^0 decays are given in table 3.1 [20]. Misidentification probability is defined as probability for a single pion, arising from $K_s^0 \rightarrow \pi^+\pi^-$ decays, to be identified as an electron.

Tag	Efficiency [%]	Missid. probability [%]
Loose	80	≈ 1.6
Standard	55	≈ 0.4
Tight	45	≈ 0.2

Table 3.1: Efficiencies and misidentification probabilities, averaged over momentum and direction of tracks, for different tags of electron identification (taken from [20]). Misidentification probabilities are measured on selected $K_s^0 \rightarrow \pi^+\pi^-$ decays.

An algorithm for the reconstruction of the converted photons in material in front of the TPC tags the electrons arising from such a process.
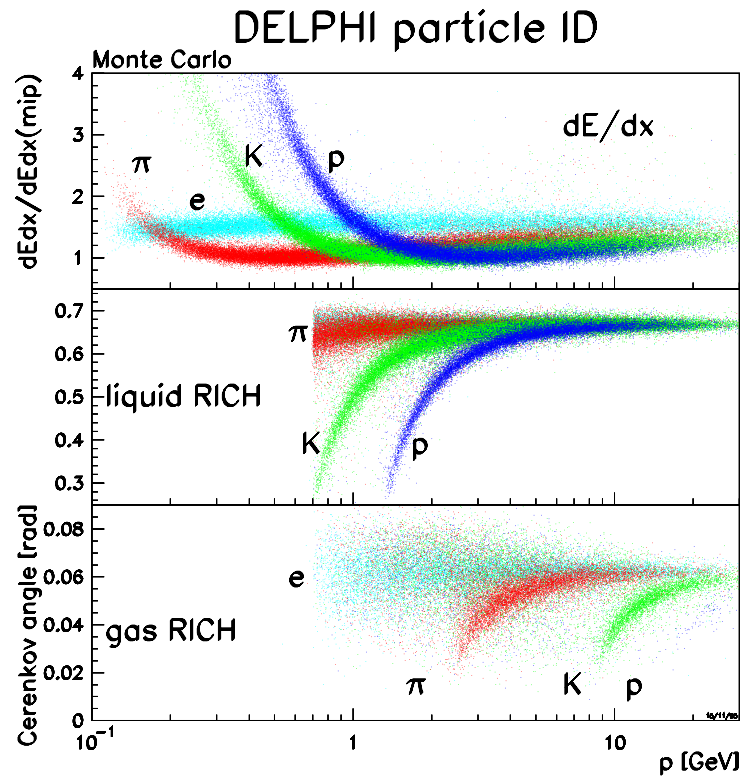
Figure 3.6: Specific ionization reconstructed by the TPC and Čerenkov angle reconstructed by the RICH for electrons and different types of hadrons as a function of the particle momentum. The specific ionization is normalized to the dE/dx of minimum ionizing particles. The plots shown are the result of the reconstruction for simulated hadronic Z^0 decays (taken from [20]).

- Muon Identification

  The identification of muons is based on the separation between hadrons and muons provided by the iron of the Hadron Calorimeter (HCAL). This material prevents the majority of hadrons to enter five planes of Muon Chambers (MUC), located in the final part and outside the HCAL. However, there are still residual hadronic tracks, or remnants of the hadronic showers developed in the HCAL, that are traversing the material in

front of the MUC. Hits in the drift chambers of the MUC which are produced by such punch-through are more scattered than hits produced by the prompt muons. Hence an additional suppression of the background is obtained by performing a χ^2 fit to extrapolated tracks from the tracking part of the spectrometer together with associated hits in the MUC. Tracks with associated hits are tagged as very loose, loose, standard or tight muon candidates, each tag corresponding to a different cut on the χ^2 of the fit. Standard and tight tags require also an associated hit in one of the two outermost layers of the MUC.

The efficiency for muon identification was determined from data. Decays of Z^0 into muon pairs provide a source of muons which can be easily identified from the topology of events. The same is valid also for $Z^0 \rightarrow \tau^+\tau^-$ decays, where one of τ leptons decays into a muon. The latter sample can be used for extraction of misidentification probability as well. For that purpose, τ decays into pions were used. Efficiencies are given in table 3.2 [20], together with probability for pions to be identified as muons.

Tag	Efficiency [%]	Missid. probability [%]
Very Loose	95.9 ± 0.1	5.4 ± 0.2
Loose	94.8 ± 0.1	1.5 ± 0.1
Standard	86.1 ± 0.2	0.7 ± 0.1
Tight	76.0 ± 0.2	0.4 ± 0.1

Table 3.2: Efficiencies and misidentification probabilities, averaged over momentum and direction of tracks, for different tags of muon identification (taken from [20]).

- Charged Hadron Identification

  In Delphi, charged hadrons are being identified by dE/dx measurements in the TPC and with the Ring Imaging Čerenkov

Detectors (RICH). The measurement of specific ionization is performed as described in the section about the electron identification. A dE/dx value is available for about 75% of the particles in hadronic Z^0 decays. The inefficiency is mostly due to the imposed cut on the number of wires hit by a track, and due to a 2 cm two track separation in the TPC. One σ level separation between kaons and pions for momenta above 2 GeV/c is achieved by the specific ionization measurement alone [20] (see figure 3.6 for the plot of specific ionization for different hadrons).

The RICH detector contains two radiators in which particles emit Čerenkov light. The two radiators differ in the value of refractive index n. The angle between the direction of emitted photons and direction of the particle is

$$\cos \theta_c = \frac{1}{n}\sqrt{1 + \frac{M^2 c^2}{p^2}} \, , \qquad (3.5)$$

where M and p are mass and momentum of the particle. By measuring the value of Čerenkov angle θ_c and given the momentum of the particle, one can reconstruct its mass.

Čerenkov light is emitted only above a certain threshold momentum which can readily be obtained from equation (3.5), imposing the inequality $\cos \theta_c \leq 1$. If the RICH is used for separation of particles below the threshold from those giving light in radiators, it is said to be used in a veto mode.

The Čerenkov angle as a function of the momentum is shown in figure 3.6 for different types of particles. The plot is a result of the reconstruction for a simulated sample of hadronic Z^0 decays [20]. Approximate momentum ranges for separation of pions, kaons and protons, using either reconstruction of

the Čerenkov angle or a veto mode, are given in table 3.3 [26]. Pions and kaons, for example, are identified by a measurement of θ_c in the liquid radiator from $p \approx 0.7$ GeV/c (threshold for kaons Čerenkov radiation) to $p \approx 5$ GeV/c. The veto mode in the gas radiator can be used from 2.5 GeV/c, where pions start to radiate, to 8.5 GeV/c, the momentum, up to which kaons do not emit light. The Čerenkov angle for kaons in the gas radiator can thus be reconstructed from 8.5 GeV/c, and distinguished from θ_c for pions up to $p \approx 21$ GeV/c.

	$K^\pm/\pi^\pm$	$p^\pm/\pi^\pm$	$K^\pm/p^\pm$
Liquid, θ_c	0.7 - 5.0	1.5 - 7.5	0.7 - 7.5
Gas, veto	2.5 - 8.5	2.5 - 16	8.5 - 16
Gas, θ_c	8.5 - 21	16 - 25	16 - 25

Table 3.3: Approximate momentum ranges (in GeV/c) for separation of pions, kaons and protons, with measurement of Čerenkov angle or using a veto mode in the RICH detector (taken from [26]).

Expected values of θ_c are determined from data over a wide range of momenta, using clean samples of particles, e.g pions from K_s^0 decays. Knowing the expected angles for different particles, the measured value can be translated into a probability for a track being due to a pion, kaon or proton. This probability is combined with an analogous quantity obtained by the dE/dx measurement in the TPC.

The combined measurements of dE/dx in the TPC and Čerenkov angle in the RICH provide a four level tag for kaons and protons. Various tags, very loose, loose, standard and tight, offer a selection of particle samples with different efficiency and of different purity. By requiring, for example, the very loose kaon tag, kaons can be selected with an efficiency over 90%, averaged over the momentum and direction of particles. The

purity, defined as a fraction of true kaons in the selected sample, is of the order of 30%. Tighter tags have lower efficiency and higher purity. For the standard tag both the efficiency and purity have a value of 70% [20].

Part III

Data Analysis

As already indicated in the introduction the present part describes the analysis of data taken by the Delphi spectrometer with the aim of the B_s^0 lifetime measurement. Two separate chapters deal with the selection of two samples of B meson semileptonic decays. In each chapter, first all the possible decay channels contributing to the selected final state are presented. The general description of selection criteria is followed by the list of cuts used and by the study of the obtained sample composition. The next section describes the evaluation of proper decay times. Each chapter is concluded with the results of the performed maximum likelihood fit to decay time distributions and the evaluation of systematic errors.

Chapter 4

The ϕ - ℓ Analysis

In hadronic decays of Z^0 several processes contribute to the presence of a lepton and a ϕ meson in the same jet. In order to perform a lifetime measurement on an isolated sample of such events, contributions of different production mechanisms must be evaluated. The processes that contribute to the $\phi - \ell$ final state are listed below, with corresponding Feynman diagrams shown in figure 4.1.

1. Direct semileptonic decays of strange and non-strange B mesons ($b \rightarrow \ell$):

   a. Semileptonic decays of B_s^0 mesons where a ϕ meson in the final state originates from an intermediate charmed (D) meson (figure 4.1-1.a).

   b. Semileptonic decays of non-strange B mesons with a ϕ meson in the final state produced in a charmed meson decay (figure 4.1-1.b).

2. Cascade decays of B mesons ($b \rightarrow c \rightarrow \ell$) where the lepton and the ϕ meson are produced in the semileptonic decay of a D meson. These processes may be subdivided into three categories:

    a. Decays of non-strange B mesons into two charmed mesons; the lepton and the ϕ meson arise from the decays of two different D mesons (figure 4.1-2.a).

    b. The initial B_s^0 meson decays into a D_s meson; the lepton and the ϕ are decay products of the latter (figure 4.1-2.b).

    c. A non-strange B meson produces a D_s meson which is a source of both the lepton and the ϕ meson (figure 4.1-2.c).

3. Semileptonic decays of D_s mesons (figure 4.1-3.) produced in $Z^0 \rightarrow c\bar{c}$ events (c $\rightarrow \ell$).

4. Events with leptons arising from light hadron decays or misidentified leptons. This category will often be addressed as the fake lepton category.

5. Events where the lepton accompanies a ϕ meson from the original fragmentation of quarks.

6. Accidental combinations of pairs of charged tracks with the invariant mass in the ϕ region, usually called the combinatorial background.

At this point, it should be mentioned that the above processes are listed in a decreasing value of the mean transverse momentum of the lepton, with respect to the jet axis. Definition of the transverse momentum, as well as its discriminating power, will be discussed in the section on selection of leptons.

Different production mechanisms can be separated into those where the appearance of a ϕ meson is induced by b quarks (1.,2.) and those where ϕ originates from lighter quarks (3.-5.). Apart from the signal process 1.a all the other categories do not contain a semileptonic decay of B_s^0 meson and are thus classified as
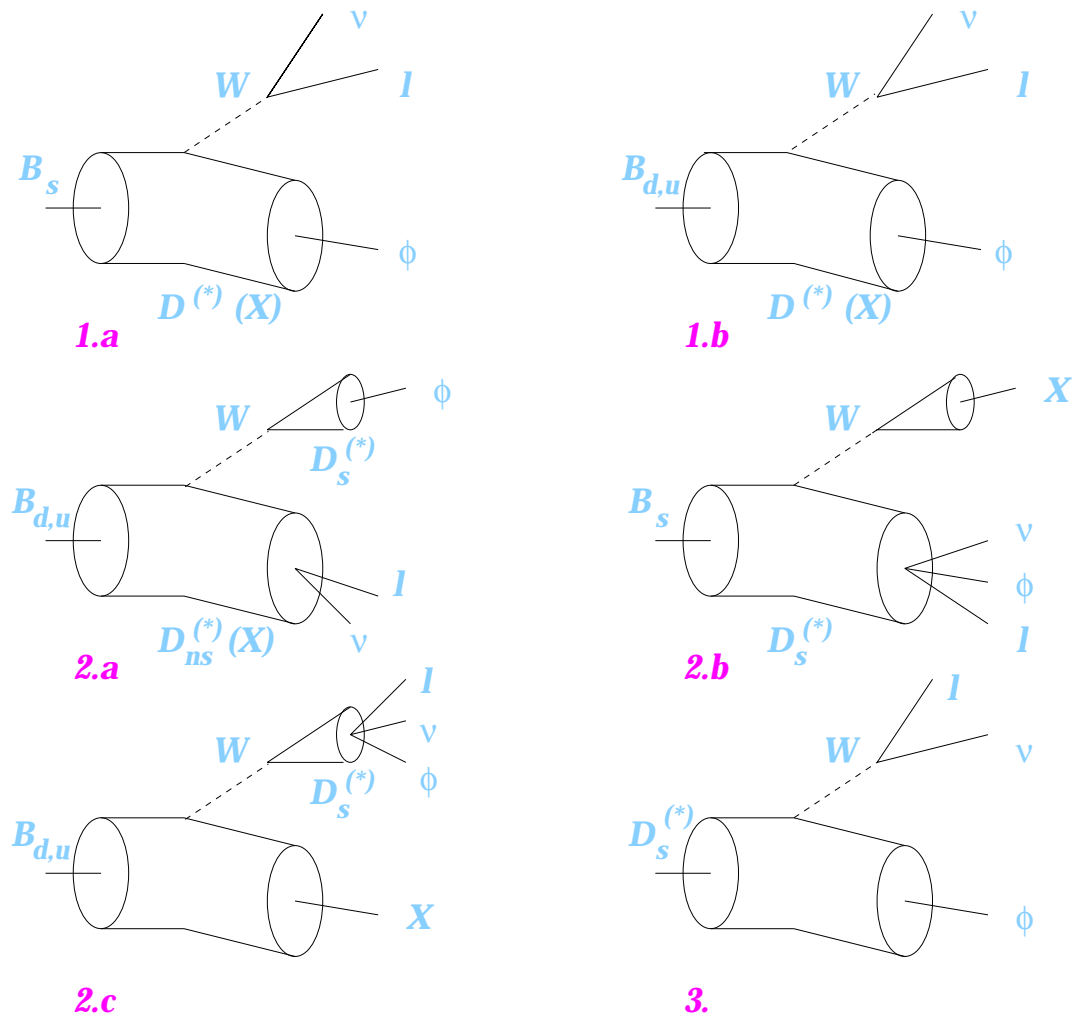
Figure 4.1: Feynman diagrams of different production mechanisms of a ϕ meson and a lepton in the same hadronic jet. Processes 1.a and 1.b correspond to direct semileptonic decays of b quarks. Processes 2.a-c are cascade decays of the type $b \to c \to \ell$. Process 3. is the semileptonic decay of a strange charmed meson produced directly in $Z^0 \to c\bar{c}$ event. The symbol D is used to describe any charmed meson, D_s is used for strange charmed mesons and D_{ns} for non-strange charmed mesons. X denotes any hadronic system that can be additionally produced in a process.

a background[1]. The classes of events labelled 4. and 6. are non-physical processes and are due to a specificity of the apparatus and the experimental method used. While the process 1.b is a source of irreducible background for the B_s^0 lifetime measurement all the other sources can be reduced by appropriate selection criteria.

The following sections describe the selection of direct semileptonic B_s^0 decays and determination of the fractions of the above mentioned processes in the selected sample of events. For a determination of the selection criteria and efficiencies we used simulated hadronic Z^0 decays. These events were generated according to the Jetset parton shower model [28] and processed through the full simulation of the Delphi spectrometer [29].

4.1 Selection of Hadronic Events

The isolation of events where the B_s^0 meson undergoes a semileptonic decay starts with a selection of hadronic Z^0 decays. Hadronic events are searched for and tagged already at the level of the central production of tapes containing the data.

The most important criterion for the selection of hadronic events is the number of charged tracks observed in the event. While the average number of charged tracks in hadronic decays is around 20, the decays $Z^0 \to e^+e^-$, $\mu^+\mu^-$ result in a presence of only two tracks in the final state. In decays of Z^0 into two τ leptons several tracks can be present in the final state, because of possible subsequent decays of τ leptons. However, the number of charged tracks in $Z^0 \to \tau^+\tau^-$ events is still well below the average number of tracks in hadronic decays. A cut on the charged multiplicity of

---

[1]Although the process 2.b is induced by the B_s^0 meson it is suppressed by the selected cut on the transverse momentum of the lepton.

the event efficiently removes the background arising from leptonic decays of the Z^0. Hence at least 5 charged tracks must be present in the event to be selected as $Z^0 \rightarrow q\overline{q}$ event. In order to minimise the effect of wrong reconstruction, these tracks must satisfy the following criteria [27]:

- $p > 400$ MeV/c

- $20° < \theta < 160°$

- track length at least 30 cm in the TPC.

The total energy of these tracks must exceed 12% of the centre-of-mass energy.

For a set of tracks i with momenta p_i the thrust axis $\vec{n}$ is calculated from the definition of the thrust T:

$$T = \max_{\vec{n}}(\frac{\sum_i |\vec{p}_i \vec{n}|}{\sum_i |\vec{p}_i|}) . \tag{4.1}$$

The polar angle of the thrust axis of the event is required to satisfy $|\cos\theta_{thrust}| < 0.95$.

With the described cuts, hadronic events are selected with an efficiency over 95%. The remaining background, arising mainly from $Z^0 \rightarrow \tau^+\tau^-$ events and two photon collisions, is below 0.7%.

The number of recorded Z^0 hadronic decays with the Delphi spectrometer, selected according to the above criteria, was around 751×10^3 in 1992, 755×10^3 in 1993 and 1484×10^3 in 1994 data taking period. The $\phi - \ell$ analysis includes the 1993 and 1994 data.

4.2   Selection of Leptons

According to the simple spectator model, the momentum spectrum of the lepton from semileptonic decay, evaluated in the centre-of-mass system, depends quadratically on the mass of the decaying

quark [12]. While the total momentum in the laboratory frame mostly depends on the Lorentz boost, the spectrum of the momentum transversal to the direction of the meson flight is not affected by the Lorentz transformation. This allows one to obtain an enriched sample of mesons containing b quarks by requiring a high transverse momentum p_t of the identified lepton. On average B mesons have larger momentum than charmed mesons produced in $Z^0 \rightarrow c\bar{c}$ events or particles produced in light quark decays of the Z^0 [30]. This is demonstrated by the shape of Peterson fragmentation functions for b and c quarks, sketched in figure 2.2. Hence also a cut on the total momentum of leptons helps to isolate B meson semileptonic decays.

In the present analysis tracks with the tight, standard or loose muon tag were considered as muon candidates. For electrons the tight or the standard tag of the identification algorithm was required. Electron candidates found to originate from a γ conversions were rejected. τ leptons decay into hadrons and leptons before they can be detected with the spectrometer as a single charged track. Hence they were not used for the isolation of the event sample.

The direction of B_s^0 mesons was approximated by the thrust axis of the jet containing the lepton track. The transverse momentum of the lepton was calculated with respect to the axis of the jet, after having removed the lepton from it. The adequacy of the meson direction approximation was studied using the Monte Carlo simulated sample of B_s^0 decays. It can be inferred from figure 4.2, showing the difference in $\cos\theta$ between the simulated direction of the B_s^0 meson and the reconstructed axis of the jet. The width of the distribution is $\sigma(\cos\theta) = (3.37 \pm 0.07) \times 10^{-2}$ with small
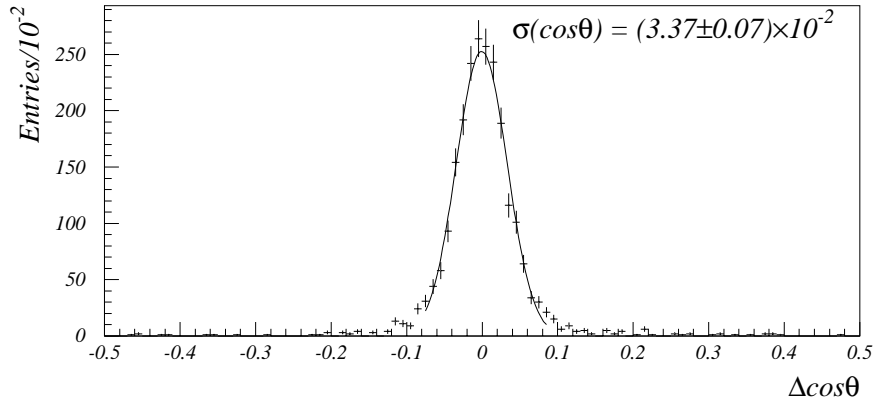
non-Gaussian tails.

Figure 4.2: The difference between the polar angle of the simulated B_s^0 direction and the polar angle of the reconstructed axis of the jet containing the lepton from semileptonic decay of the meson. The distribution was obtained on the simulated sample of B_s^0 decays.

Figure 4.3 shows the total and the transverse momentum of leptons originating from direct B meson decays, from cascade decays, where a B meson decays into a charmed meson and the lepton is a product of the charm decay, as well as from semileptonic decays of charmed mesons produced in $Z^0 \to c\bar{c}$ events. The distributions were obtained on the Monte Carlo sample of hadronic Z^0 decays. The background includes misidentified leptons and leptons originating from light hadron decays. The process $b \to \tau \to \mu(e)$ is included in the cascade category. The p_t distribution includes the cut on the total momentum $p \geq 3$ GeV/c. To illustrate the influence of the cut on the p_t for the isolation of direct semileptonic B meson decays, one can calculate the increase in the fraction of these decays among the processes of figure 4.3 for a certain minimal required transverse momentum of the lepton. By selecting events with $p_t > 1.0$ GeV/c the fraction of direct B meson decays

is increased by a factor of approximately 1.7.

For the isolation of the $\phi\ell$ sample the identified leptons were selected by requiring the total momentum p greater than 2.0 GeV/c and the transverse momentum p_t greater than 1.0 GeV/c. In addition the lepton track had to have at least one associated hit in the Vertex Detector. The last criterion was used in order to assure an accurate determination of the secondary vertex.
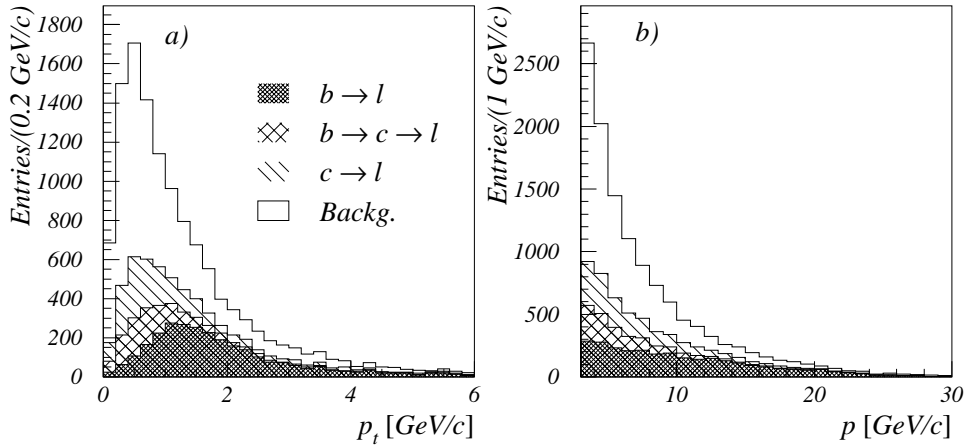
Figure 4.3: a) The reconstructed transverse momentum of leptons from different sources in the Monte Carlo sample of hadronic Z^0 decays. p_t is calculated with respect to the axis of the jet to which the lepton is attributed. The distribution includes the cut on the total momentum $p \geq 3$ GeV/c. b) Same for the total momentum of leptons.

4.3   Selection of ϕ Mesons

ϕ mesons were reconstructed through the $\phi \rightarrow K^+K^-$ decay mode which represents (49.1 ± 0.9) % of the total ϕ meson decay width [5]. Charged particles of the event were separated into two hemispheres defined by a plane perpendicular to the thrust axis of the event. The invariant mass was calculated for all pairs of particles with the opposite charge and in the same hemisphere as the

identified lepton by assigning them the mass of the kaon. Figure 4.4 a) shows simulated momentum distributions of the $K^{\pm}$ candidates with invariant mass in the ϕ meson region: 1.01 GeV/c^2 $\leq$ $M(K^+K^-)$ $\leq$1.03 GeV/c^2. Selection of the high momentum kaons suppresses the number of events with kaon candidates arising primarily from the fragmentation, i.e. the processes 5.-7. listed at the beginning of this chapter. However, the cut on the $K^{\pm}$ momentum cannot be very tight, not only because of the loss of statistics, but also due to the larger relative contribution of direct charm decays (process 3.) at higher values of p_K. Together with cascade decays (process 2.a-c), direct charm events are highly suppressed by the cut on the total and transverse momentum of the lepton as described in the previous section.

For the reconstructed ϕ meson momentum a similar feature as for the p_K can be seen in figure 4.4 b).

A quantity, which is partially correlated to the momentum of the kaons as well as to the transverse momentum of the lepton, is the invariant mass of the $K^+K^-\ell^{\pm}$ combination, shown in figure 4.4 c). In contrast to the momentum of the kaons and the ϕ meson, $M(\phi\ell)$ enables also a partial suppression of cascade and direct charm events.

Because of the Lorentz boost of the ϕ meson and the phase space limitation for the $\phi \rightarrow K^+K^-$ decay, the momenta of the two kaon candidates are highly correlated as shown in figure 4.5. By imposing a cut on the correlation between the two momenta one suppresses the combinatorial background only above the ϕ mass region and does not change significantly the signal to background ratio achieved by the other selection requirements. The effect of such a cut on the mass distribution of the combinatorial back-
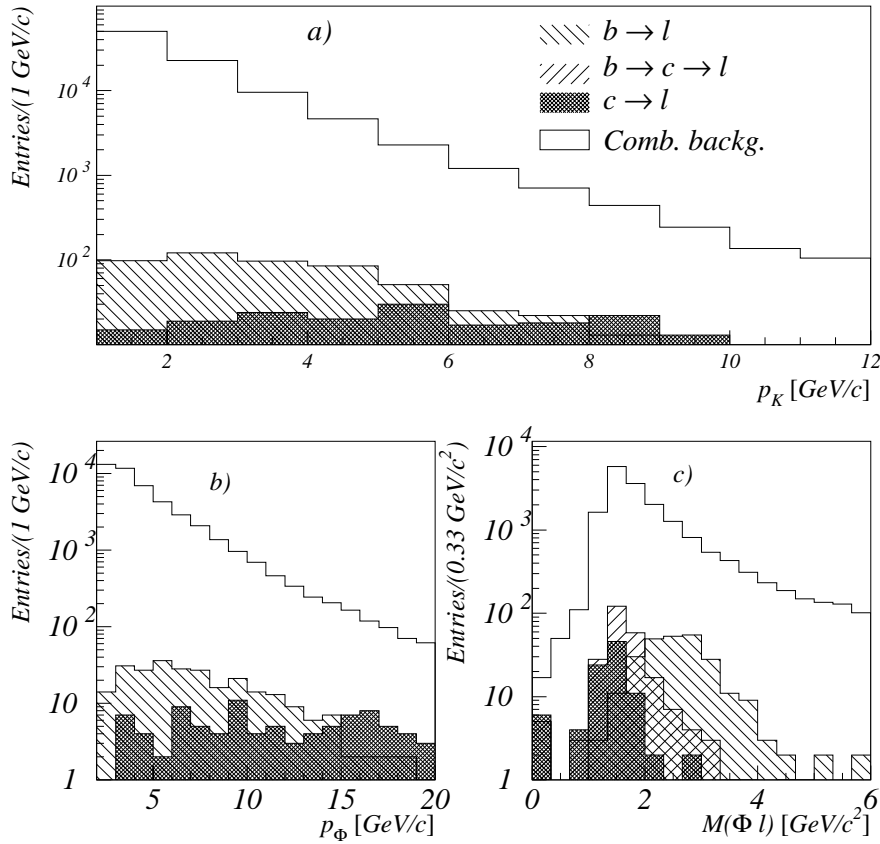
Figure 4.4: a) Momentum distributions of kaons from ϕ decays produced in different categories of events. The contribution of cascade decays is not shown since it is very similar to the distribution of direct semileptonic B meson decays. b) Same for the reconstructed ϕ meson momentum. c) Distributions of the invariant mass of $K^+K^-\ell^\pm$ combination. All distributions were obtained on the simulated sample of hadronic Z^0 decays.

ground was studied on the simulated events. As described below the final parametrization of the mass distribution describes properly the number of the true ϕ mesons.

From the study of simulated hadronic Z^0 decays a set of cuts for the ϕ meson reconstruction was chosen. Since the performance of the spectrometer has not been identical during the years of data
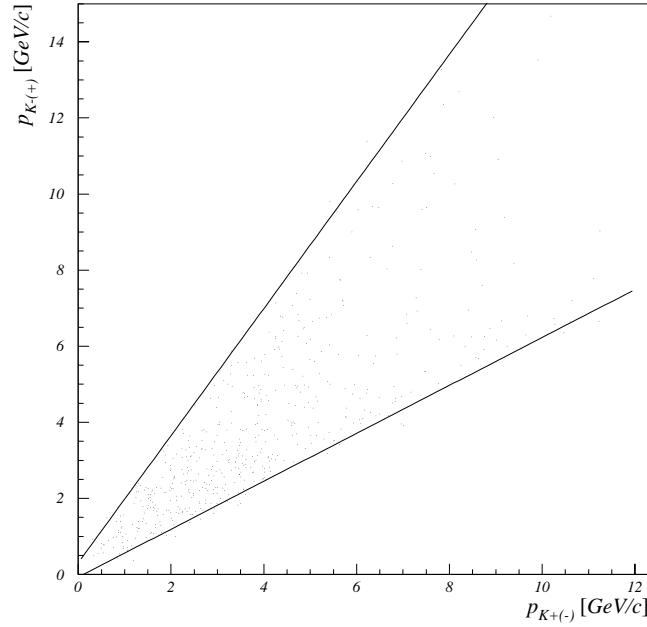
Figure 4.5: The correlation between momenta of kaons from the ϕ decay. Only ϕ mesons coming from direct semileptonic decays of B meson were considered. Lines represent imposed cuts used for the selection described in the text.

taking also the cuts were slightly different in order to get a similar signal to background ratio. In particular since the RICH detectors were fully operational only in the 1994 several kinematical cuts were tightened for the 1993 data. The first selection criterion was applied to the 1994 data and the cut in parenthesis to the 1993 data:

- $p_{K^\pm} > 1.5$ GeV/c (2.0 GeV/c)

- $p_\phi > 3.5$ GeV/c (4.0 GeV/c)

- $M(K^+K^-\ell^\pm) > 1.7$ GeV/c^2 (1.9 GeV/c^2)

- $1.67\ p_{K^{-(+)}} + 0.31$ GeV/c $>\ p_{K^{+(-)}}\ >\ 0.63\ p_{K^{-(+)}} - 0.07$ GeV/c.

In order to further suppress the combinatorial background
the kaon candidates had to be also identified by the hadron identi-
fication algorithm (see section 3.2.3). A loose kaon tag was required
for at least one of the charged tracks used to reconstruct the ϕ me-
son (both kaons had to be identified by a very loose tag for the 1993
data). The very loose tag enables the selection of kaons with an ef-
ficiency over 90% and with a pion misidentification probability of
the order of 30%.

The invariant mass distribution for the selected kaon pairs is
shown in figure 4.6. It was fitted using a Breit-Wigner function to
account for the signal and a polynomial for the parametrization of
the combinatorial background. The fitting function describes well
the shape of the distribution as obtained from the simulation. The
width of the fitted Breit-Wigner function reflects the natural width
of ϕ meson resonance, $\Gamma_\phi = (4.43\pm0.05)$ MeV [5], as well as the res-
olution of spectrometer. A signal of 433 ± 62 events was observed
in the mass region 1.008 GeV/c^2 < $M(\mathrm{K}^+\mathrm{K}^-)$ < 1.030 GeV/c^2. The
signal is centred at M_ϕ=(1.019$\pm$0.001) GeV/c^2 and has a width of
Γ=(11.0$\pm$1.5) MeV. The invariant mass distribution is in agreement
with the Monte Carlo prediction shown in the same plot. The value
of M_ϕ agrees with the nominal mass (1019.413 $\pm$ 0.008) MeV/c^2
of the ϕ meson [5]. The relative difference between the simulated
and the fitted number of ϕ mesons in the simulated sample was
found to be $(N_{fit} - N_{sim})/N_{sim} \approx 6\%$. This value is below the sta-
tistical error of the fit. It can be concluded that no accumulation of
combinatorial background in the ϕ mass region is introduced by
the cuts used to select the sample of events.
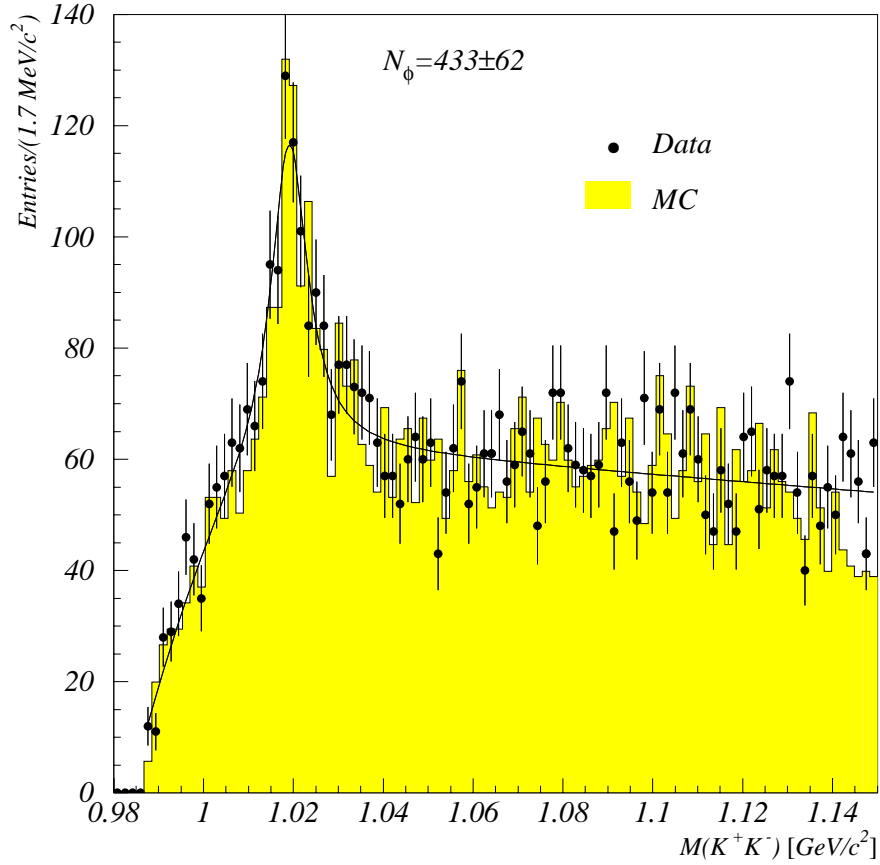
Figure 4.6: The invariant mass distribution of the selected kaon pairs. The distribution obtained from the $Z^0 \rightarrow q\bar{q}$ simulation is shown for comparison.

4.4 Composition of the Selected Sample

In order to gain insight into the composition of the selected sample a numerical evaluation of relative contributions described at the beginning of this chapter must be performed. Events with the invariant mass of the kaon pair between 1.008 GeV/c^2 and 1.030 GeV/c^2 were considered for the composition study and for the B_s^0 lifetime measurement. Various production rates and branching ratios used in the calculations are summarized in table 4.1 [31]. Selection ef-

ficiencies for different processes were estimated from the Monte
Carlo simulation.

Measured quantity	Value
$B_1 = Br(\overline{b} \to B_s^0 \to D_s^- \ell^+ \nu X) \times Br(D_s^- \to \phi\pi^-)$	$(3.1 \pm 0.5) \times 10^{-4}$
$B_2 = Br(\overline{b} \to B_{u,d} \to D_s X) \times Br(D_s \to \phi\pi)$	$(3.66 \pm 0.22) \times 10^{-3}$
$B_3 = Br(\overline{b} \to B_s^0 \to D_s X) \times Br(D_s \to \phi\pi)$	$(3.9 \pm 0.9) \times 10^{-3}$
$B_{bc\ell} = Br(\overline{b} \to \overline{c} \to \ell^-)$	$(8.22 \pm 0.42) \times 10^{-2}$
$Br(\overline{b} \to \ell^+)$	$(10.43 \pm 0.24) \times 10^{-2}$
$P_{u,d} = Br(\overline{b} \to B_u^\pm) = Br(\overline{b} \to B_d^0)$	0.392 ± 0.022
$P_s = Br(\overline{b} \to B_s^0)$	0.100 ± 0.022
$R_b = \Gamma(Z^0 \to b\overline{b})/\Gamma(Z^0 \to q\overline{q})$	0.2202 ± 0.002
$R_c = \Gamma(Z^0 \to c\overline{c})/\Gamma(Z^0 \to q\overline{q})$	0.1583 ± 0.0098
$Br(D_s^\pm \to \phi X)/Br(D_s^\pm \to \phi\pi^\pm)$	4.8 ± 0.5
$Br(D^0 \to \phi X)$	$(1.8 \pm 0.3) \times 10^{-2}$
$Br(D^+ \to \phi X)$	$(1.7 \pm 0.3) \times 10^{-2}$

Table 4.1: Measured branching ratios and production rates used for the
calculation of the ϕ meson sample composition [31].

Probabilities for observing a certain category of events in the
hadronic decay of the Z^0 are given below:

1. a. The probability of observing a semileptonic decay of the
       B_s^0 meson is

$$P_1^{B_s} = 2R_b P_s \big[Br(B_s^0 \to D_s^- \ell^+ \nu X) Br(D_s^- \to \phi X) +$$
$$+ Br(B_s^0 \to D_{ns} \ell^+ X) Br(D_{ns} \to \phi X) \big] \approx$$
$$\approx 2R_b B_1 \frac{Br(D_s^- \to \phi X)}{Br(D_s^- \to \phi\pi^-)} \ . \tag{4.2}$$

In the last line we used an inclusive branching ratio $B_1 = P_s Br(B_s^0 \to D_s^- \ell^+ \nu X) Br(D_s^- \to \phi\pi^-)$ defined in table 4.1.
The much smaller contribution of non-strange D mesons
in (4.2) with regard to $B_s^0 \to D_s^- \ell^+ X$ decays is a conse-
quence of the ratio $Br(D_s \to \phi X)/Br(D^{0(+)} \to \phi X) \approx 10$,
and of the fact that non-strange D mesons in the B_s^0 decay

are mainly produced via an orbitally excited D_s^{**} meson. The fraction of D_s^{**} in B_s^0 decays has not yet been measured but can be inferred from the measured production rate in non-strange B decays where it amounts to approximately 1/3 (see Appendix A). Hence the approximation done in the last line of (4.2) is justified.

b.

$$P_1^B = 2R_b P_{u,d} \big[Br(B_{u,d} \to D^0 \ell X) Br(D^0 \to \phi X) +$$
$$+ Br(B_{u,d} \to D^+ \ell X) Br(D^+ \to \phi X) \big] \approx$$
$$\approx 4R_b P_{u,d} Br(b \to \ell) Br(D^{0(+)} \to \phi X) \qquad (4.3)$$

is the probability for direct semileptonic non-strange B meson decay. Since the inclusive branching ratios for D^0 and D^+ decays into the ϕ meson are equal within the errors, instead of $[Br(B_{u,d} \to D^0 \ell X) + Br(B_{u,d} \to D^+ \ell X)]$ we can use the $Br(b \to \ell)$ in the last line of (4.3). The probability for a $D_s^\pm \ell^\mp$ pair occurrence in the $B_{u,d}$ decay requires an intermediate $D^{**0(+)} \to D_s K$ decay and was not incorporated into P_1^B (see Appendix A).

2. a. The cascade production of ϕ and ℓ from two different D mesons in non-strange B decay has the probability

$$P_2^B = 2R_b P_{u,d} Br(B_{u,d} \to D_s D_{ns} X) \big[Br(D_{ns} \to \ell X) Br(D_s \to \phi X) +$$
$$+ Br(D_s \to \ell X) Br(D_{ns} \to \phi X) \approx$$
$$\approx 2R_b B_{bc\ell} B_2 \frac{Br(D_s \to \phi X)}{Br(D_s \to \phi \pi)} \cdot \qquad (4.4)$$

Again the contribution from the $D^{0(+)}$ was neglected in comparison with the D_s contribution.

b. The relative occurrence of cascade B_s^0 decays into a strange

D meson per hadronic Z^0 event is

$$
\begin{aligned}
P_2^{\text{B}_\text{s}} &= 2R_\text{b}P_\text{s}\left[Br(\text{B}_\text{s}^0 \to \text{D}_\text{s}X) - Br(\text{B}_\text{s}^0 \to \text{D}_\text{s}^-\ell^+X)\right]Br(\text{D}_\text{s} \to \phi\ell\nu) = \\
&= 2R_\text{b}(B_3 - B_1)\frac{Br(\text{D}_\text{s} \to \phi\ell\nu)}{Br(\text{D}_\text{s} \to \phi\pi)} .
\end{aligned}
\tag{4.5}
$$

From the inclusive branching fraction $Br(\text{B}_\text{s}^0 \to \text{D}_\text{s}X)$ we subtracted the semileptonic branching ratio since the latter decays by definition belong to the category 1.a.

c. The last of cascade decays is the process with a non-strange B decay where ℓ and ϕ are both products of a D_s . The probability for such a production mechanism is

$$
\begin{aligned}
P_3^B &= 2R_\text{b}P_\text{u,d}Br(\text{B}_\text{u,d} \to \text{D}_\text{s}X)Br(\text{D}_\text{s} \to \phi\ell\nu) = \\
&= 2R_\text{b}P_\text{u,d}B_2\frac{Br(\text{D}_\text{s} \to \phi\ell\nu)}{Br(\text{D}_\text{s} \to \phi\pi)} .
\end{aligned}
\tag{4.6}
$$

3. The only direct charm decay expected to contribute to the selected sample is a D_s semileptonic decay with the probability

$$
P_1^{\text{D}_\text{s}} = 2R_\text{c}P_\text{s}Br(\text{D}_\text{s} \to \phi\ell\nu) .
\tag{4.7}
$$

The production rate of strange mesons in $c\bar{c}$ events is assumed to be the same as in $b\bar{b}$ events.

The relative contribution of cascade decays (2.a-c) in the selected sample was determined from the simulation, by comparing the number of cascade decays that pass the selection criteria with the number of all events in the sample. The sum of the three processes yielded

$$
f_{bc\ell} = \frac{N(\text{b} \to \text{c} \to \ell)}{N(\text{all events in sample})} = 0.014 \pm 0.004 .
\tag{4.8}
$$

The contribution of direct charm events (process 3.) was found to be negligible (of the order of 5×10^{-3}).

Larger fractions of background events were found to originate from the following sources:

4. Fake leptons accompanying the ϕ meson represented f_{fake}=0.11±0.02 of the simulated sample after the cuts.

5. The relative contribution of ϕ mesons arising from the primary fragmentation was f_{frag}=0.030±0.006, evaluated from simulation.

6. The fraction of the combinatorial background was determined directly from the fit to the mass distribution of the K^+K^- invariant mass. It was found to be f_{comb}=0.629±0.085.

The B_s^0 purity of the sample is defined as the fraction of B_s^0 mesons among all the selected B mesons. The kinematics of non-strange B meson decays described by the process 1.b is very similar to the kinematics of B_s^0 decays (process 1.a). No difference in the reconstruction efficiency (ϵ_{B_s}, $\epsilon_{B_{u,d}}$) for these classes of events was expected and indeed a negligible difference was found from the simulated events. The purity of the sample can thus be calculated from the probabilities derived above:

$$f_{B_s} = \frac{\epsilon_{B_s} N(B_s^0)}{\epsilon_{B_s} N(B_s^0) + \epsilon_{B_{u,d}} N(B_{u,d})} = \frac{P_1^{B_s}}{P_1^{B_s} + P_1^B} = 0.50 \pm 0.07 . \tag{4.9}$$

4.5   Lifetime Measurement

4.5.1   Evaluation of the Proper Decay Time

In order to evaluate the proper decay time of a B_s^0 meson two quantities must be determined: the decay length L and the momentum p_{B_s} of the decaying particle. The proper decay time is then given

by

$$t \; = \; \frac{L \, M_{B_s}}{p_{B_s}} \tag{4.10}$$

with $M_{B_s} = (5375 \pm 6)$ MeV/c^2 [5].

The uncertainty of the calculated decay time t is derived as a function of the measurement errors on L and p_{B_s}:

$$\sigma_t \; = \; \frac{M_{B_s}}{p_{B_s}} \sqrt{\sigma_L^2 + \frac{\sigma_{p_{B_s}}^2}{M_{B_s}^2} t^2} \; . \tag{4.11}$$

The measurement of the decay length L was achieved by the reconstruction of the secondary $K^+K^-\ell$ vertex. The fitted vertex position is obtained by minimising the χ^2 of the distance between the vertex and three tracks in a 5-dimensional space of track parameters [32]. A loose cut was imposed to the quality of the reconstructed vertex by requiring the χ^2 probability of the fit to be larger than 10^{-4} [2]. The cut is used for the rejection of badly reconstructed vertices and hence for an improvement of the decay length resolution and to a much smaller extent for the suppression of background events. Since the errors on the measured track parameters are not completely Gaussian the distribution of the χ^2 probability is not flat but peaks at lower values. The imposed cut rejects 2% of signal events.

The primary vertex of the Z^0 decay was fitted from all the charged tracks in the event except the two kaon and the lepton candidates. The interaction region of electrons and positrons, called the beam spot, was used as a constraint in the fit. It is determined for about every 200 recorded hadronic decays. Coordinates of the primary vertex are fitted for these subsamples of events and the

---

[2]The number of degrees of freedom for the vertex fit is 2N - 3, where N is the number of outgoing tracks.

mean and the width of coordinate distributions determine the position and the size of the beam spot. The size varies in time with typical values between 100 and 120 μm in one of the coordinates transverse to the direction of the beam and approximately 10 times smaller values in the other direction. If the primary vertex fit failed the position of the beam spot was used for the evaluation of the decay length.

For the data taken in 1993 the decay length L followed from the relation

$$L \; = \; \frac{L_t}{\sin \theta_{B_s}} \; ,\tag{4.12}$$

where L_t is a measured distance between the primary and the secondary vertex in the (R, φ) plane. $\sin \theta_{B_s}$ is the polar angle of the B meson direction approximated by the thrust axis of the jet containing the ϕ meson and the lepton. For 1994 data the decay length was reconstructed in 3 dimensions due to the measurement of the z coordinate with the upgraded Vertex Detector. The sign of the decay length was determined with regard to the angle between the direction of the momentum of the $\phi\ell$ system, denoted by $\vec{P}$ in figure 4.7, and the vector joining the reconstructed primary and secondary vertex $\vec{L}$. Due to the measurement errors on parameters of tracks and due to the background events the angle can be larger than 90°. A negative decay length was assigned to such events.

The average decay length of B_s^0 mesons increases and the angle between the direction of the lepton and the ϕ meson decreases with increasing momentum of a B_s^0. Since the precision of the vertex reconstruction improves for larger angles between the outgoing tracks the resolution on the decay length σ_L was parametrized as
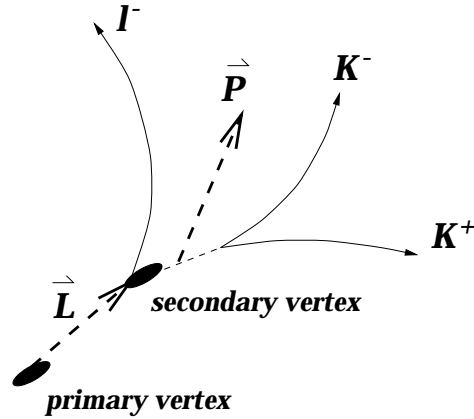
Figure 4.7: Illustration of a $\phi\ell$ event with vector $\vec{L}$, joining the primary and secondary vertex, and momentum of the $\phi\ell$ system $\vec{P}$. For events, where the angle between the two vectors was larger than $90°$, the decay length was signed negatively.

a function of the decay length:

$$\sigma_L \;=\; \begin{cases} a_L + b_L^+ L \; ; \; L > 0 \\ a_L + b_L^- L \; ; \; L < 0 \end{cases} . \tag{4.13}$$

The parameters were estimated from simulated B_s^0 decays. For the 1994 data they were found to be $a_L = (276 \pm 12)$ μm, $b_L^+ = (4.43 \pm 0.46) \times 10^{-2}$ and $b_L^- = -0.443 \pm 0.023$. For the 1993 data the corresponding values were (319 ± 26) μm, $(5.09 \pm 1.01) \times 10^{-2}$ and -0.527 ± 0.054 respectively. For each event used for the lifetime measurement the precision on the decay length was calculated according to the above parametrization on the event-by-event basis.

For a general illustration, the average difference between reconstructed and generated decay lengths is shown in figure 4.8 a) for the 1994 simulated data. The distribution was fitted with two Gaussian distributions. The width of the narrower Gaussian was $< \sigma_L > = (371 \pm 28)$ μm. The wider Gaussian comprised a small

fraction of events ($\approx$ 6%) with $< \sigma_L > \approx$ 4 mm. Since kaons and leptons do not originate from the same vertex a small shift in the mean of the distribution was observed. Its value was around 70 μm which is negligible compared to the resolution. In the 1993 the average resolution $< \sigma_L >$ was slightly worse and amounted to (429 ± 97) μm.

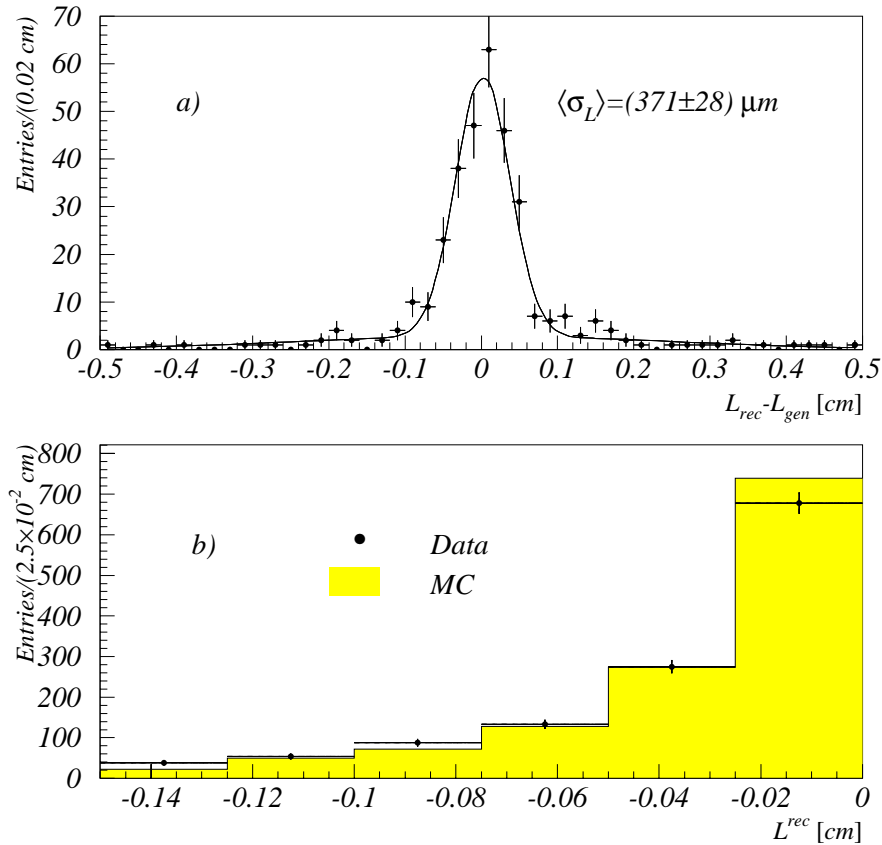Figure 4.8: a) The average accuracy on the decay length L obtained on the simulated sample of B_s^0 decays. b) The comparison of negative decay length distributions for the simulated and the real data sample enriched in light quark decays.

A possible discrepancy between the accuracy of decay length determination for the real data and simulated events was checked by comparing negative decay length distributions for which the res-

olution effects are dominating. The sample of events was selected using the same cuts as described above. In addition events were required to have a low probability of originating from $Z^0 \to b\overline{b}$ decays [33]. The comparison is shown in figure 4.8 b). The relative difference in the mean of the two distributions is 9.8%. Hence in the final evaluation of systematic errors on the B_s^0 lifetime measurement the resolution σ_L was varied for $\pm\,10\%$ to account for the possible difference between the Monte Carlo and the real data.

The analysis of the simulated sample showed that an approximate linear relation holds between the fraction of the momentum taken by a $\phi\ell$ system in decays of B_s^0 mesons and the $\phi\ell$ momentum itself. The following B_s^0 momentum estimate was obtained from the fit to the dependence shown in figure 4.9 a):

$$\frac{p(\phi\ell)}{p_{B_s}} \;=\; a_p \;+ b_p \; p(\phi\ell) \;, \qquad\qquad (4.14)$$

with $a_p \;=\; 0.203 \pm 0.065$ and $b_p \;=\; (1.83 \pm 0.28) \times 10^{-2}$ c/GeV. The momentum of a B_s^0 meson as well as the accuracy of the momentum evaluation were calculated from the above values of fitted parameters and their errors for each individual event in the data sample.

Figure 4.9 b) shows the average relative difference between the reconstructed and the simulated momentum of the B_s^0 meson. The distribution was fitted with the sum of two Gaussians. The parametrization (4.14) resulted in an average error on the B_s^0 momentum of about 16%.

In order to check the reliability of the Monte Carlo simulation the comparison of the reconstructed momentum in simulated and real data was performed. The reconstructed momentum of real events in the signal region after the subtraction of the background, taken from the side band in the K^+K^- invariant mass distribution
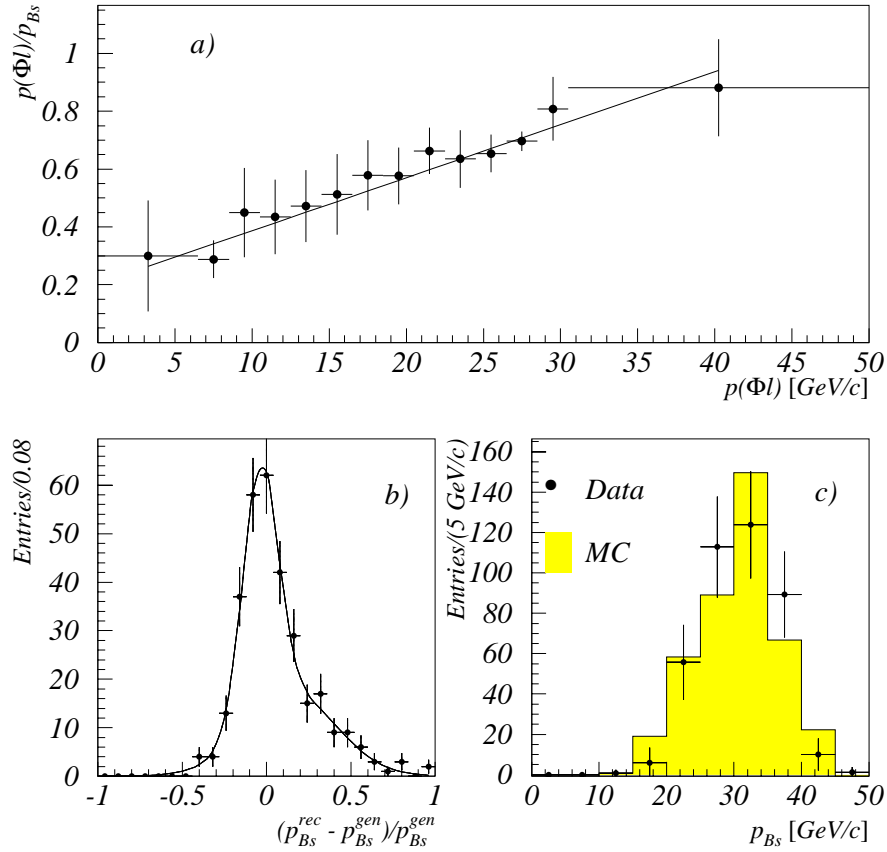
Figure 4.9: a) The simulated fraction of the momentum taken by a $\phi\ell$ system in decays of B_s^0 mesons. b) The difference between the simulated and reconstructed B_s^0 momentum as obtained on the Monte Carlo sample of B_s^0 decays. c) Comparison of the reconstructed momentum for the simulated and real data in the signal region, after the subtraction of the combinatorial background (see text).

(1.06 GeV/c^2 < M(K$^+$K$^-$) < 1.15 GeV/c^2), is shown in figure 4.9 c). The agreement with the momentum reconstructed in the simulated sample is satisfactory. The difference between the mean values of these distributions is 0.3 ± 0.4 GeV/c. The statistical error of this difference was considered in evaluation of the systematic error on the lifetime measurement, arising from the possible difference between the real and simulated data in the B_s^0 momentum estimation.

The corresponding momentum distributions were compared also for combinatorial background events taken from the side band in the K^+K^- invariant mass distribution. No significant difference was observed in these distributions as well.

The cuts used for the sample selection might influence the efficiency behaviour as a function of the proper decay time of a B_s^0 meson. This dependence was studied in the simulated sample and found to be constant within the statistical error over the studied decay time range. The efficiency dependence on the generated proper decay time can be seen in figure 4.10 for kinematical cuts and after the inclusion of kaon identification. The full line shows the result of the χ^2 fit to the efficiency of the selected cuts without the kaon identification requirements. The value of the fitted constant is (45 ± 2) %. Note that the plotted efficiency does not include the geometrical acceptance due to the requirement of at least one Vertex Detector hit for the kaon and lepton candidates.
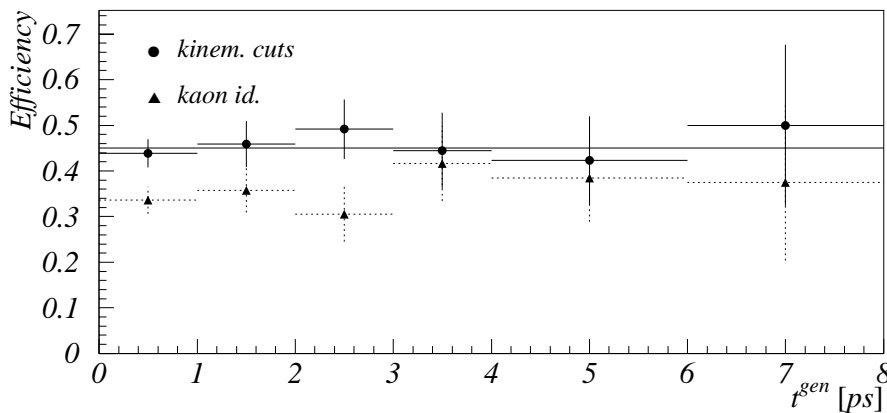

Figure 4.10: The efficiency of the ϕ meson sample selection criteria as a function of the generated proper decay time of a B_s^0 meson. Circles illustrate the efficiency of kinematic cuts alone and triangles the efficiency after inclusion of kaon identification. The efficiency does not include the geometrical acceptance of the VD.

4.5.2 Likelihood Fit

To obtain the B_s^0 lifetime an unbinned maximum likelihood fit was
performed on the proper decay time distribution of selected events
in the ϕ meson signal region. The likelihood function was con-
structed with individual terms describing different contributions
to $\phi\ell$ events, estimated in section 4.4:

$$
\begin{aligned}
\mathcal{L} \;=\; \prod_{i=1}^{N_{signal}} &\Big[(1 - f_{comb} - f_{bckg}) f_{B_s} \mathcal{P}_{B_s}(t_i, \sigma_{t_i}, \tau_{B_s}) \;+ \\
&+\; (1 - f_{comb} - f_{bckg})(1 - f_{B_s}) \mathcal{P}_{B}(t_i, \sigma_{t_i}, \tau_{B}) \;+ \\
&+\; f_{comb} \mathcal{P}_{comb}(t_i, \sigma_{t_i}, \tau_{comb}, f_{comb}^{G}) \;+ \\
&+\; f_{bckg} \mathcal{P}_{bckg}(t_i, \sigma_{t_i}, \tau_{bckg}, f_{bckg}^{G}) \;.
\end{aligned}
\tag{4.15}
$$

The probability density distribution for B_s^0 decays was de-
scribed by a convolution of an exponential and a Gaussian function
(see Appendix B):

$$
\begin{aligned}
\mathcal{P}_{B_s}(t_i, \sigma_{t_i}, \tau_{B_s}) \;&=\; \mathcal{G}(t_i, \sigma_{t_i}) \otimes \mathcal{E}(t_i, \tau_{B_s}) \;\equiv \\
&\equiv\; \frac{1}{\sqrt{2\pi}\,\sigma_{t_i} \tau_{B_s}} \int_0^\infty e^{\frac{-(t_j - u)^2}{2\sigma_{t_i}^2}} \, e^{\frac{-u}{\tau_{B_s}}} \, du \;.
\end{aligned}
\tag{4.16}
$$

The same form was assumed for the probability density dis-
tribution of non-strange B meson decays $\mathcal{P}_{B}(t_i, \sigma_{t_i}, \tau_{B})$ with τ_{B_s} re-
placed by the average $B_u^\pm$ and B_d^0 meson lifetime $\tau_{B} = (1.60 \pm 0.04)$ ps
[34].

The decay time probability distribution for combinatorial back-
ground events was parametrized as a sum of two terms: a Gaussian
and an exponential convoluted with a Gaussian. The first term de-
scribes events with all the selected tracks arising from the primary
fragmentation or decays with a negligible decay length. The sec-
ond term accommodates for events with the kaon candidates from

the fragmentation and the lepton originating from particles with a
non-vanishing decay time:

$$\mathcal{P}_{comb}(t_i, \sigma_{t_i}, \tau_{comb}, f^G_{comb}) \;=\; f^G_{comb} \mathcal{G}(t_i, \sigma_{t_i}) \;+$$
$$+\; (1 - f^G_{comb}) \mathcal{G}(t_i, \sigma_{t_i}) \otimes \mathcal{E}(t_i, \tau_{comb}) \;.$$
$$(4.17)$$

Parameters τ_{comb} and f^G_{comb} were derived by performing the un-
binned maximum likelihood fit with the above term to events in
the upper side band of the K^+K^- invariant mass distribution. The
fit yielded $\tau_{comb} = (1.57 \pm 0.05)$ ps and $f^G_{comb} = 0.457 \pm 0.011$.
The corresponding distribution and the fitted curve are shown in
figure 4.11 b). The lifetime of the flying part of the combinatorial
background τ_{comb} is similar to the mean lifetime of B mesons. The
effect is due to the enrichment of the sample in B meson decays
caused by the cut on the transverse momentum of the lepton.

   The contribution of events with fake leptons and small con-
tributions of events with ϕ mesons from fragmentation and cas-
cade decays were considered together in $\mathcal{P}_{bckg}(t_i, \sigma_{t_i}, \tau_{bckg}, f^G_{bckg})$.
Their relative fraction was obtained from the contributions given
in section 4.4 as $f_{bckg} = f_{fake} + f_{frag} + f_{bc\ell}$. The corresponding
probability term was parametrized with the same expression as
(4.17). The parameters obtained from the fit to the distribution of
simulated events (figure 4.11 c)) were $\tau_{bckg} = (1.76 \pm 0.07)$ ps and
$f^G_{bckg} = 0.501 \pm 0.012$.

   After the incorporation of the necessary parameters into the
likelihood function (4.15), the final fit to events in the ϕ meson
signal region was performed with τ_{B_s} as a free parameter. Figure
4.11 a) shows the proper decay time distribution and the result of
the fit superimposed. The fitted lifetime was

$$\tau_{B_s} \;=\; (1.73 \;\pm\; 0.20(\text{stat.})) \text{ ps} \;. \qquad (4.18)$$
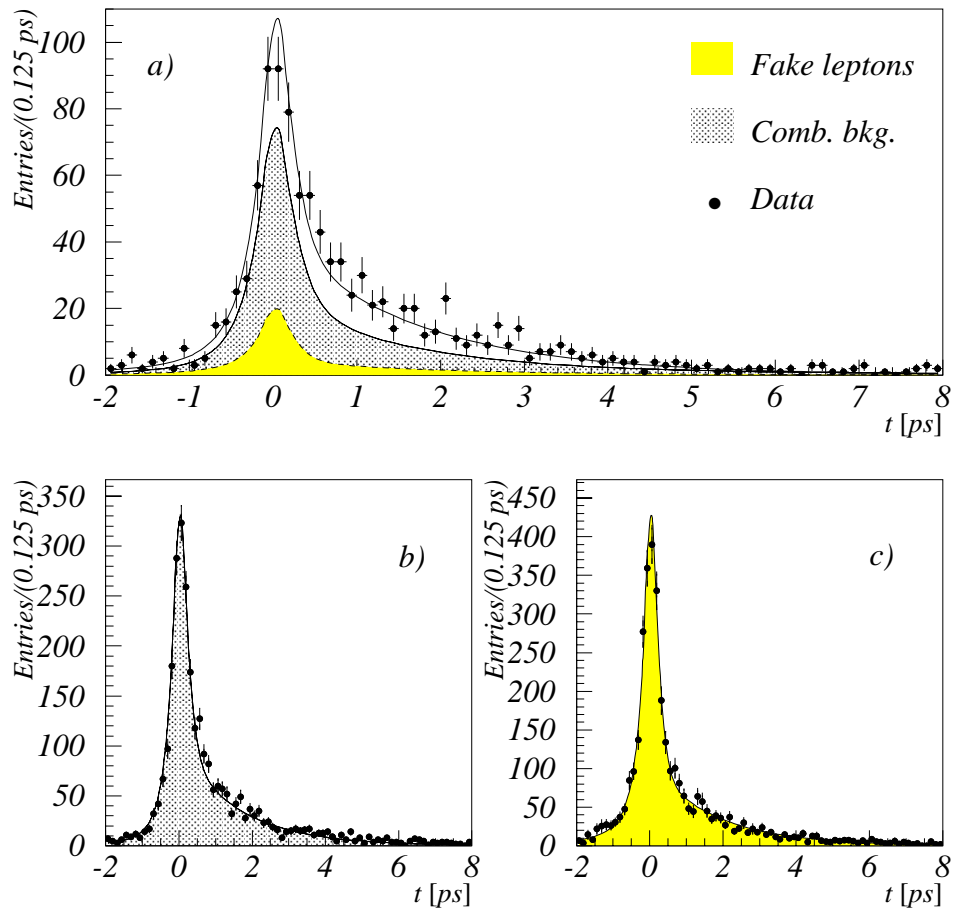
Figure 4.11: a) The proper decay time distribution for events in the ϕ meson signal region. The result of the maximum likelihood fit is shown superimposed. Shaded regions are contributions of different types of background described in the text. b) Same for events in the side band of the kaon pair invariant mass. The full curve is the result of the maximum likelihood fit with the term describing the combinatorial background. c) The proper decay time distribution for events with fake leptons, ϕ mesons from fragmentation and cascade decays. The distribution was obtained on the simulated sample and fitted with the corresponding probability density term.

As a cross-check the fitting function containing the term for the signal (4.16) was used to fit the simulated proper decay time distribution of B_s^0 decays. The distribution was obtained using the same set of cuts as for the real data sample. For the sample with the generated lifetime of 1.6 ps the resulting fitted lifetime was 1.580 ± 0.075 ps.

4.5.3   Systematic Errors

Systematic errors of the B_s^0 lifetime measurement can be divided into three types. The first category arises from the τ_{B_s} dependence on the parameters entering the maximum likelihood fit. These errors were estimated by repeating the fit with parameters changed by 1σ from the average value. Parameters which were estimated by the fit of the simulated sample of B_s^0 decays, or of the side band of the invariant mass distribution, were changed in a correlated manner considering the resulting correlation coefficients of these fits. Variations of the fitted lifetime caused by the corresponding parameter errors are summarized in table 4.2.

The main contribution arises from the uncertainty in the fraction of the combinatorial background in the data sample. The increase in the fraction f_{comb} is compensated by a decrease of semileptonic B_s^0 decays in the sample. The fit performed with an increased fraction of combinatorial background, in order to evaluate the systematic error arising from the uncertainty in f_{comb}, thus results in a statistically less accurate fitted lifetime. Nevertheless, the difference between this value and the central value (4.18) represents a systematic error of this source. This offers an explanation for an asymmetry found in the systematic error which is due to the combinatorial background.

Source of systematic error	$\tau_{\mathrm{B_s}}$ variation [ps]
Combinatorial background (f_{comb}, f^G_{comb}, τ_{comb})	$+0.117$ -0.042
Fake leptons (f_{bckg}, τ_{bckg}, f^G_{bckg})	$+0.025$ -0.021
Purity ($f_{\mathrm{B_s}}$)	$+0.021$ -0.020
Average B lifetime (τ_B)	$+0.008$ -0.009
Difference data/MC in $p_{\mathrm{B_s}}$ eval.	$+0.032$ -0.029
Difference data/MC in σ_L	$+0.026$ -0.033
Possible analysis bias	$+0.083$ -0.083
Total	$+0.153$ -0.107

Table 4.2: Summary of systematic errors on the $\mathrm{B_s^0}$ lifetime measurement for the $\phi\ell$ sample.

The second category of systematic effects includes possible differences between the Monte Carlo simulation and real data. These discrepancies have already been discussed in the section on the decay length and $\mathrm{B_s^0}$ momentum estimation. In order to account for them the values of the momentum and the decay length resolution were varied for 0.4 GeV/c and 10%, respectively.

Finally, a possible bias of the analysis was studied. The bias may be a consequence of the modelling used in the fit, i.e. the parametrization of the $p_{\mathrm{B_s}}$ dependence on $p(\phi\ell)$, the parametrization of the σ_L dependence on L, the parametrization of different terms in the likelihood function, and the small proper decay time dependence of the acceptance. The above effects would manifest in a systematic shift of the fitted lifetime on a simulated sample of infinite statistics with a known generated value of the $\mathrm{B_s^0}$ lifetime. In the finite Monte Carlo sample, the difference between the generated and the fitted lifetime might arise because of the limitations of the model used, as well as because of the finite statistical power

of the sample. A conservative approach to the systematic error estimation was chosen by attributing the difference to the former cause solely. Hence the fitted lifetime was corrected for the ratio of the generated and the fitted lifetime $r_{corr} = 1.0127 \pm 0.0481$. The error $\sigma(r_{corr})\tau_{B_s}$, arising from the statistical error of the likelihood fit of the simulated sample, was included as a separate entry in the table of systematic errors. Due to the correction, the statistical error of the measurement must be multiplied by the r_{corr} as well.

Including systematic errors, the B_s^0 lifetime obtained from the $\phi - \ell$ analysis is

$$\tau_{B_s} = \left[1.75 \pm 0.20(\text{stat.}) \, {}^{+0.15}_{-0.11}(\text{syst.}) \right] \text{ps} .$$

(4.19)

Chapter 5

The $D_S^\pm$ - $\ell^\mp$ Analysis

A sample of B_s^0 decays, more exclusive than the one described in the previous chapter, may be obtained by the reconstruction of a $D_s^\pm$ meson accompanied by a lepton with an opposite charge in the same jet. Such a sample has the advantage of higher B_s^0 purity but suffers from a lower statistical power. As in the $\phi\ell$ sample several processes contribute to a $D_s^\pm\ell^\mp$ in the same jet:

I. The direct semileptonic decay of a B meson producing a strange charmed meson and a lepton (b → ℓ); the initial B meson can be strange or non-strange:

   α. The semileptonic B_s^0 decay directly produces a $D_s^\pm$ meson with the charge opposite to the charge of a lepton in the final state (figure 5.1-I.α).

   β. Decays of non-strange B mesons require an additional s$\bar{\text{s}}$ pair for the $D_s^\pm$ final state. The decay proceeds through an intermediate D^{**} state and results in the presence of a kaon among the decay products (figure 5.1-I.β).

II. Cascade decays (b → c → ℓ) where the lepton originates from the decay of a charmed meson; again there are two categories of such events:

    α. Decays of non-strange B mesons into two charmed mesons (figure 5.1-II.α).

    β. The decay of a B_s^0 into two $D_s^\pm$ mesons (figure 5.1-II.β).

III. Events with a wrongly associated lepton arising from light hadron decays or with a misidentified lepton.

IV. Decays $D^\pm \rightarrow K^\mp \pi^\pm \pi^\pm$, which by misidentification of one of the pions for the kaon produce reflections in the $D_s^\pm$ mass region. If the $D^\pm$ is a product of a non-strange B meson semileptonic decay these events simulate B_s^0 decays.

 V. The combinatorial background.

The production mechanism I.α in the figure 5.1 and in the list above is the desired signal for the lifetime measurement. The event classes I.β and II. are physical and the classes III.-V. non-physical sources of the possible background [1].

The selection criteria described below were used to isolate the sample of events containing a B_s^0 meson from around 3×10^6 hadronic Z^0 decays recorded by Delphi in 1992, 1993 and 1994. The selection of $Z^0 \rightarrow q\overline{q}$ events has been described already in the section on the $\phi - \ell$ analysis.

5.1 Selection of Leptons

By selecting electrons and muons with high total and transverse momentum the obtained sample was enriched in direct semileptonic decays of B mesons (see figure 4.3). The transverse momentum calculation was done in the same way as for the previous analysis. However, in order to gain the purity of the sample as high

---

[1] As in the $\phi - \ell$ analysis the process II.β, although induced by a B_s^0 meson, is treated as a background from cascade decays.
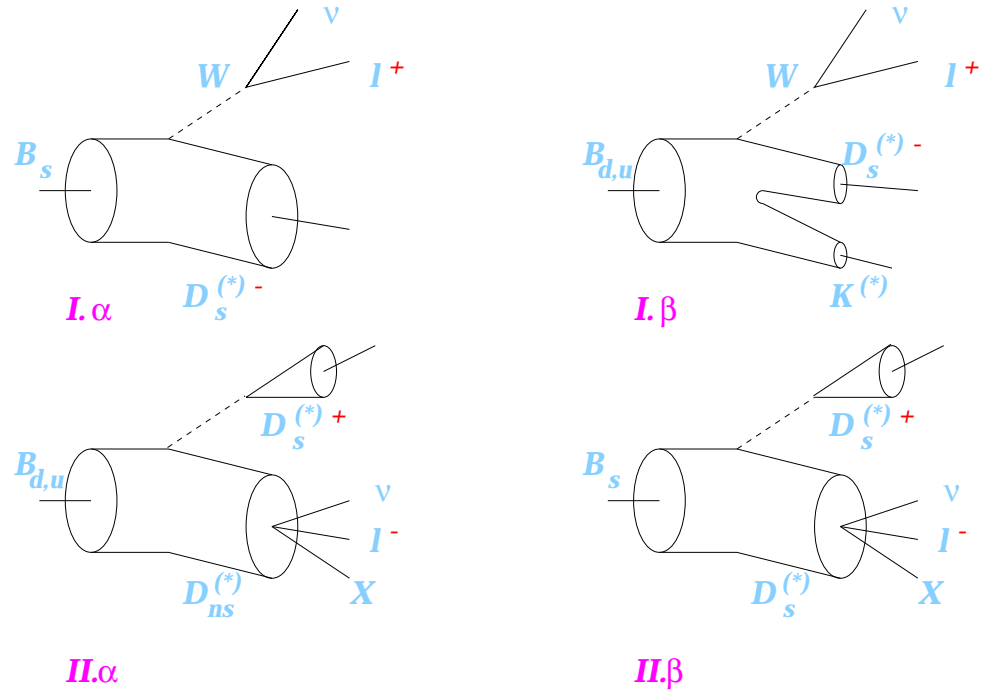
Figure 5.1: Diagrams of the processes contributing to $D_s^\pm \ell^\mp$ correlations in the same hadronic jet of the Z^0 decay. The symbol D_{ns} is used to represent non-strange charmed mesons. X denotes any hadronic system that can be additionally produced in a process.

as possible, the cuts were made tighter. Leptons were required to have at least 1.2 GeV/c transverse momentum and the total momentum above 3 GeV/c. The lepton candidate had to be associated to at least one hit in the VD. The lepton candidates were selected using the tight, standard or loose tag of the muon identification algorithm and tight or standard tag for the electron identification. In addition electrons arising from photon conversions were rejected.

5.2   Selection of $\mathrm{D}_\mathrm{S}^\pm$ Mesons

Strange charmed mesons were reconstructed in the following decay modes:

$$\mathrm{D}_\mathrm{s}^+ \; \rightarrow \; \phi\pi^+ \; ; \; \phi \; \rightarrow \; \mathrm{K}^+\mathrm{K}^-$$
$$\mathrm{D}_\mathrm{s}^+ \; \rightarrow \; \overline{\mathrm{K}}^{*0}\mathrm{K}^+ \; ; \; \overline{\mathrm{K}}^{*0} \; \rightarrow \; \mathrm{K}^-\pi^+ \qquad\qquad (5.1)$$

The corresponding branching ratios of $\mathrm{D}_\mathrm{S}^\pm$ decay modes are
$Br(\mathrm{D}_\mathrm{s}^+ \rightarrow \phi\pi^+) = (3.5 \pm 0.4)\%$ and $Br(\mathrm{D}_\mathrm{s}^+ \rightarrow \overline{\mathrm{K}}^{*0}\mathrm{K}^+) = (3.3 \pm 0.5)\%$
[5].

First the invariant mass of two oppositely charged tracks in the lepton hemisphere, defined by the thrust axis of the event, was calculated. In the ϕ decay mode both tracks were attributed the kaon mass. In the K^{*0} decay mode the pion mass was attributed to one of the tracks and mass of the kaon to the other. At this stage of analysis only the specific ionization measured in the TPC was used to resolve the mass ambiguity of the two tracks. The kaon mass was attributed to a track with lower dE/dx measurement in the TPC. The dE/dx distribution of kaons and pions from the K^{*0} decay is shown in figure 5.2 for particles with momentum larger than 1 GeV/c. If the specific ionization measurement was not available both combinations were taken into account. The calculated invariant mass had to be compatible with a ϕ or K^{*0} meson.

Since the momenta of decay products exhibit a similar behaviour as could already be seen in figure 4.4 a), the selection of particles with higher momentum suppresses the contribution from the combinatorial background. For the same reason the cut on the reconstructed ϕ or K^{*0} momentum can be applied.

The third particle with the proper charge was then added to decay products of a vector meson (ϕ or K^{*0}) and the invariant mass
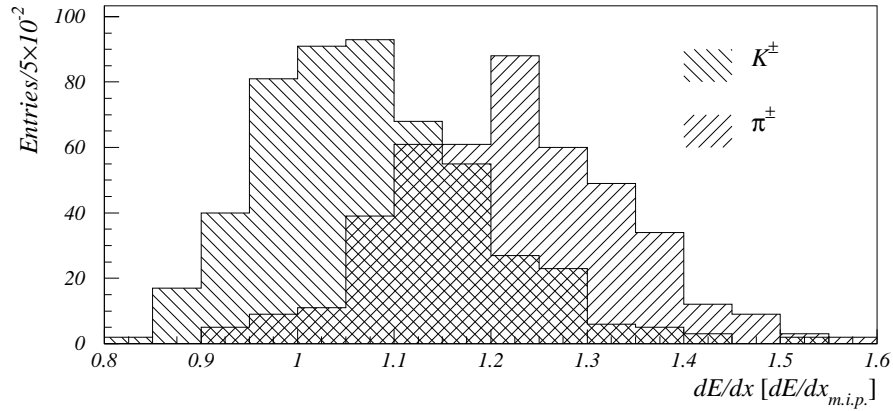
Figure 5.2: The specific ionization measured in the TPC for particles from the K^{*0} meson decay. The distribution is obtained on the simulated sample by requiring the momentum of a particle to exceed 1 GeV/c.

of the three particle $KK\pi$ combination was calculated. Figure 5.3 shows the momentum distribution of a bachelor pion from the $D_s^\pm \to \phi\pi_b^\pm$ and of a bachelor kaon from the $D_s^\pm \to \overset{(-)}{K}{}^{*0}K_b^\pm$ decay. It stretches to even higher values than the momenta of particles from the ϕ and K^{*0} decay. Note that distributions of figure 5.3 as well as that of 5.4 were obtained on the dedicated Monte Carlo sample of $D_s^\pm$ decays and hence the relative fractions of different contributions are not the same as in the real sample of $q\bar{q}$ events.

The energy distribution of pseudo-scalar mesons $D_s^\pm$ for the signal and for two sources of background is shown in figure 5.4 a). E_{D_s} is reconstructed as a square of the quadratic sum of the invariant mass and of the momentum of a $K^\pm K^\mp \pi_b^\pm$ and $K^\pm \pi^\mp K_b^\pm$ combination, for the ϕ and K^{*0} decay mode respectively. The combinatorial background exhibits a lower average energy of the meson while the distributions of the signal and of cascade decays are similar. The separation of the latter source is achieved through cuts on the quantities related to the momentum of the selected lepton.
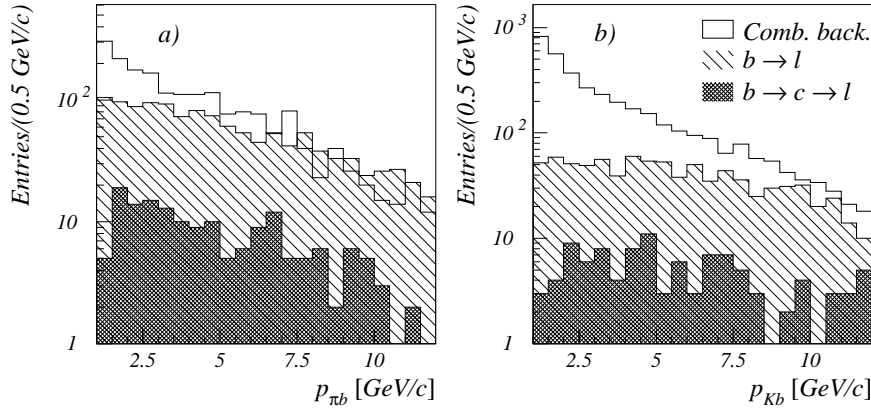
Figure 5.3: a) The momentum of a bachelor pion from the $D_s^\pm \rightarrow \phi\pi_b^\pm$. b) The momentum of a bachelor kaon from $D_s^\pm \rightarrow \overset{(-)}{K}{}^{*0}K_b^\pm$. Distributions were obtained in the dedicated Monte Carlo sample of D_s decays.

Beside the selection requirements on leptons these include the momentum and the invariant mass of a $D_s^\pm \ell^\mp$ system, shown in figures 5.4 b) and c).

In the considered decay modes a pseudo-scalar meson $D_s^\pm$ decays into a vector (ϕ, K^{*0}) and a pseudo-scalar ($\pi^\pm$, $K^\pm$) meson. Helicity conservation implies that the angle between the direction of vector meson decay products in its rest frame and the flight direction of $D_s^\pm$ follows a $\cos^2 \alpha$ dependence (see Appendix C). For the background with accidental track combinations this dependence is more isotropic. The additional suppression of the background is thus obtained by requiring a high $|\cos \alpha|$ value.

For both decay modes the secondary vertex of $D_s^\pm$ decay products was fitted. As a result of the fit, the parameters of a $D_s^\pm$ meson track were calculated for the later estimation of the B_s^0 decay vertex. For more accurate vertex determination, decay products of $D_s^\pm$ mesons as well as leptons were required to have at least one associated hit in the VD.
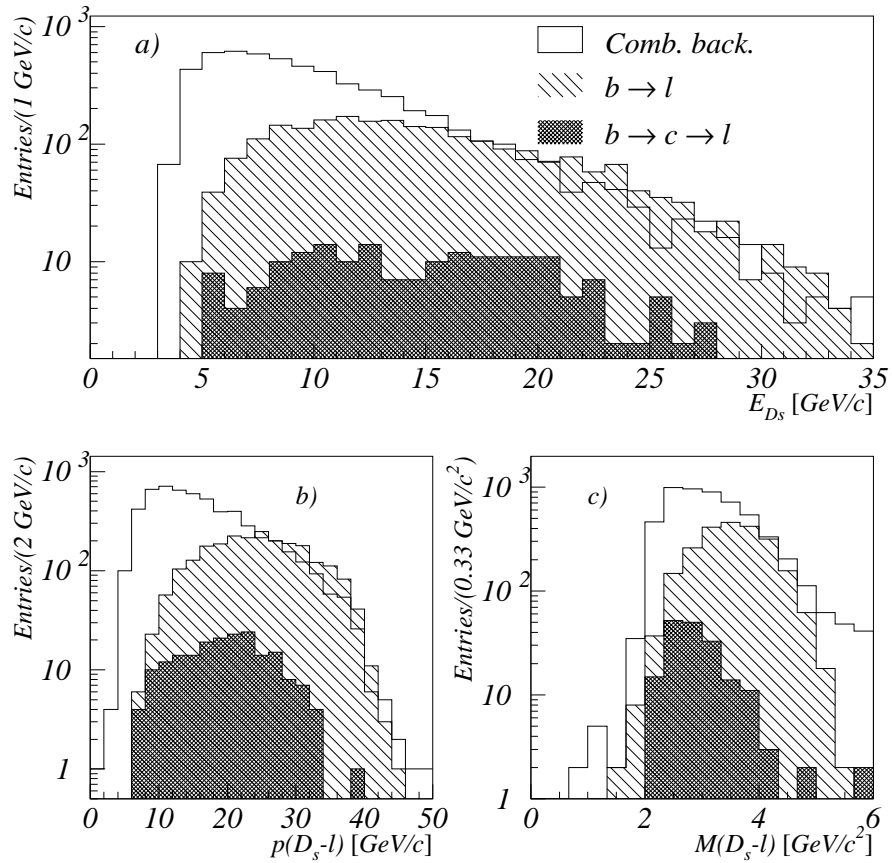
Figure 5.4: a) The energy distribution of a D$_s$ meson for various sources described in the text. b) The reconstructed momentum of a D$_s^\pm \ell^\mp$ system. c) The reconstructed invariant mass of a D$_s^\pm \ell^\mp$ system for the signal and the background. All distributions were obtained on the dedicated Monte Carlo sample of D$_s$ decays.

In accordance to general kinematical considerations given above a set of cuts was chosen for the selection of D$_s^\pm \ell^\mp$ correlations. Since the width of the ϕ meson resonance is more than ten times smaller than the width of the K^{*0} [5] the combinatorial background is expected to be larger in the latter decay mode. Some of the cuts were thus tighter for this decay channel. As for the $\phi - \ell$ analysis the cuts were tuned slightly different for different years of data

taking. Also the cuts, used to select the $D_S^{\pm}e^{\mp}$ sample, were relaxed with regard to the ones used for the $D_S^{\pm}\mu^{\mp}$ sample, due to the lower average identification efficiency and misidentification probability for electrons. The selection criteria are summarized in table 5.1.

	'92, '93				'94			
	e μ ϕ		e μ K^{*0}		e μ ϕ		e μ K^{*0}	
$p_{K^{\pm}(\pi^{\pm})}$ [GeV/c]	>1.3							
$p_{\pi_b(K_b)}$ [GeV/c]	>1.7	>2.0	>1.7	>2.0	>1.5	>2.0	>1.5	>2.0
$M(KK\pi)$ $[GeV/c^2]$	1.012- -1.028		0.855- -0.935		1.01- -1.03		0.845- -0.945	
$\lvert\cos\alpha\rvert$	>0.4							
$Prob(\chi^2)_{D_s}$	$>5\times10^{-3}$							
$p_{\phi(K^{*0})}$ [GeV/c]	>3.3		>3.3	>3.4	>3.2	>3.5	>3.2	>4.0
E_{D_s} [GeV/c]	>7.0	>9.0	>7.5	>9.5	>6.5	>8.5	>7.0	>8.5
$p(D_S^{\pm}\ell^{\mp})$ [GeV/c]	>10.0	>14.5	>11.5	>14.5	>10.0	>12.0	>10.5	>12.0
$M(D_S^{\pm}\ell^{\mp})$ $[GeV/c^2]$	>3.3				>3.0			

Table 5.1: The selection criteria used for the isolation of the $D_S^{\pm}\ell^{\mp}$ sample.

Beside kinematical cuts different identification requirements, summarized below, were imposed:

$$D_S^{\pm} \rightarrow \overset{(-)}{K}{}^{*0}K^{\pm}$$

- For the muon sample both kaon candidates had to be identified with at least a very loose tag by the combined hadron identification algorithm. For the data taken in 1994 this cut was tightened by an additional requirement for one or both tracks to be tagged by at least a loose kaon tag.

- For the electron sample only one of the kaons had to be identified by a very loose tag (both kaons for the 1994 data).

- Since the above identification criteria are tighter for 1994 data, the compatibility of the kaon candidates specific ionization

with the one expected for kaons of the same momentum was additionally checked for 1992 and 1993 data. Figure 5.5 shows the difference between the reconstructed and the expected dE/dx for the kaon and the pion hypothesis obtained in the Monte Carlo sample. σ is the r.m.s. of the Landau distribution. While the sample of kaons from K^{*0} decays is compatible with the kaon hypothesis (figure 5.5 a)), the combinatorial background, with the majority of the tracks being pions, is compatible with the pion hypothesis (figure 5.5 b)). The selection required the sum of both plotted quantities (figure 5.5 c)) to be less than 0.3.

$$\mathrm{D}_\mathrm{s}^\pm \to \phi\pi^\pm$$

- The events where a bachelor pion was identified as a kaon or a proton with the tight tag were rejected.

The signal of D$_\mathrm{s}^\pm$ mesons accompanied with a lepton of the opposite charge (right sign) obtained with the described selection criteria is shown in figure 5.6. The invariant mass distribution was fitted with the sum of an exponential slope for the combinatorial background and two Gaussian distributions. The Gaussians of equal width described the D$_\mathrm{s}^\pm$ and a small contribution from D$^\pm \to \phi\pi^\pm(\overset{(-)}{\mathrm{K}}{}^{*0}\mathrm{K}^\pm)$ decays. The D$^\pm$ mass was fixed at a nominal value of (1869.4 ± 0.4) MeV/c^2 [5]. 81 ± 13 D$_\mathrm{s}^\pm$ candidates were found within $\pm 2\sigma_{\mathrm{D}_\mathrm{s}}$ from the peak centred at $M_{\mathrm{D}_\mathrm{s}} = (1.968 \pm 0.002)$ GeV/c^2. This value agrees with the nominal mass of a D$_\mathrm{s}^\pm$ meson of (1968.5 ± 0.7) MeV/c^2 [5]. The width of the D$_\mathrm{s}^\pm$ meson peak was found to be $\sigma_{\mathrm{D}_\mathrm{s}} = (13.5 \pm 2.2)$ MeV.

The same selection was repeated on data for the isolation of the same charge D$_\mathrm{s}^\pm\ell^\pm$ pairs (wrong sign). The mass distribution
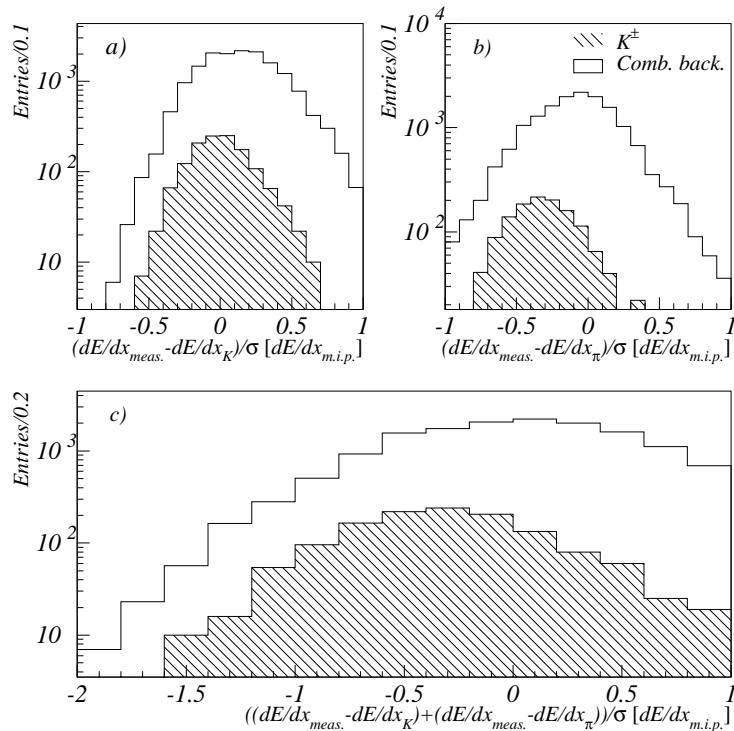
Figure 5.5: a) The difference between the measured specific ionization and the one expected for kaons with the same momentum. The distribution for the sample of kaons from K^{*0} decays is centred at zero while the combinatorial background has a higher mean value. b) Same difference for the pion hypothesis. c) The sum of quantities shown in a) and b). The suppression of the combinatorial background is achieved by selecting tracks with lower values of this sum. All distributions were obtained in the simulated sample of K^{*0} decays.

is shown together with the right sign combinations. No excess of events is found in the D$_s^\pm$ mass region, in accordance to the absence of physical processes that might contribute to such charge correlations.

Invariant mass distributions for subsamples of the single decay mode (ϕ, K^{*0}) and lepton flavour (e$^\pm$, $\mu^\pm$) are shown separately in figure 5.7. The fitted masses are equal to the one obtained in the full sample and the widths of the signals agree within statistical
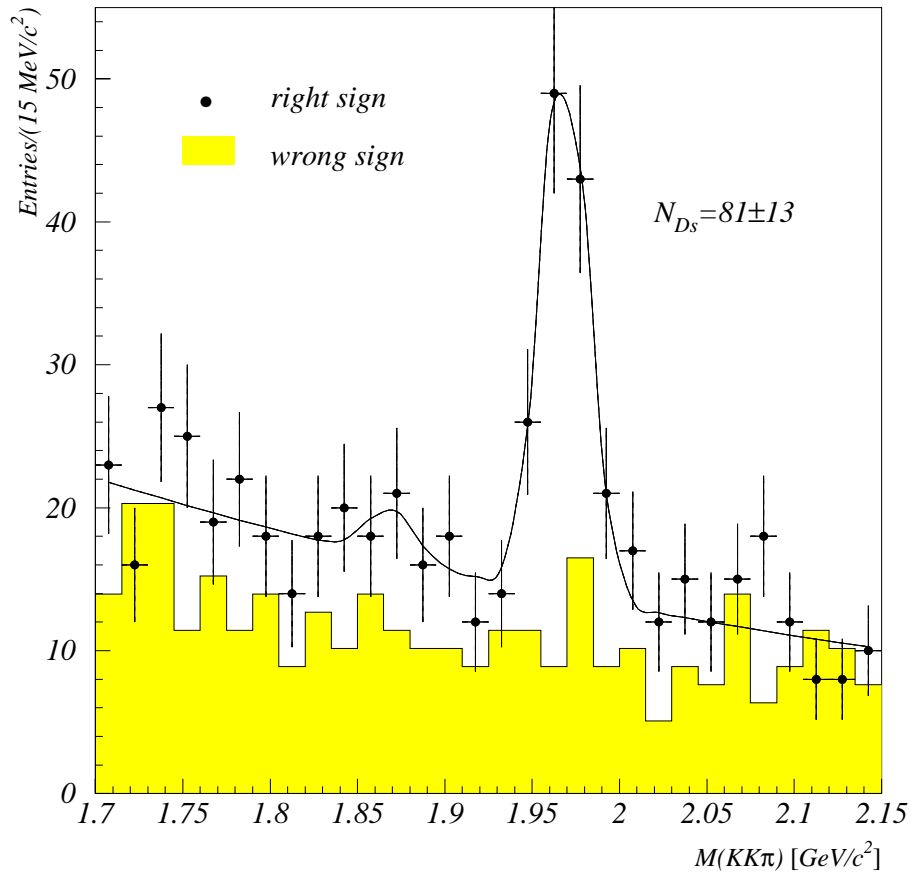
Figure 5.6: The invariant mass distribution of KKπ combinations in the selected $D_s^{\pm} \rightarrow \phi\pi^{\pm}$, $\overset{(-)}{K}{}^{*0}K^{\pm}$ decays, accompanied by $\ell^{\mp}$ in the same jet. The shadowed region shows the distribution of the same charge $D_s^{\pm}\ell^{\pm}$ combinations.

errors of the fit.

5.3   Composition of the Selected Sample

The lifetime measurement was performed on events in the $D_s^{\pm}$ meson mass region between 1.941 and 1.995 GeV/c^2. To correctly construct the likelihood function relative fractions of different processes contributing to events in this signal region must be calcu-
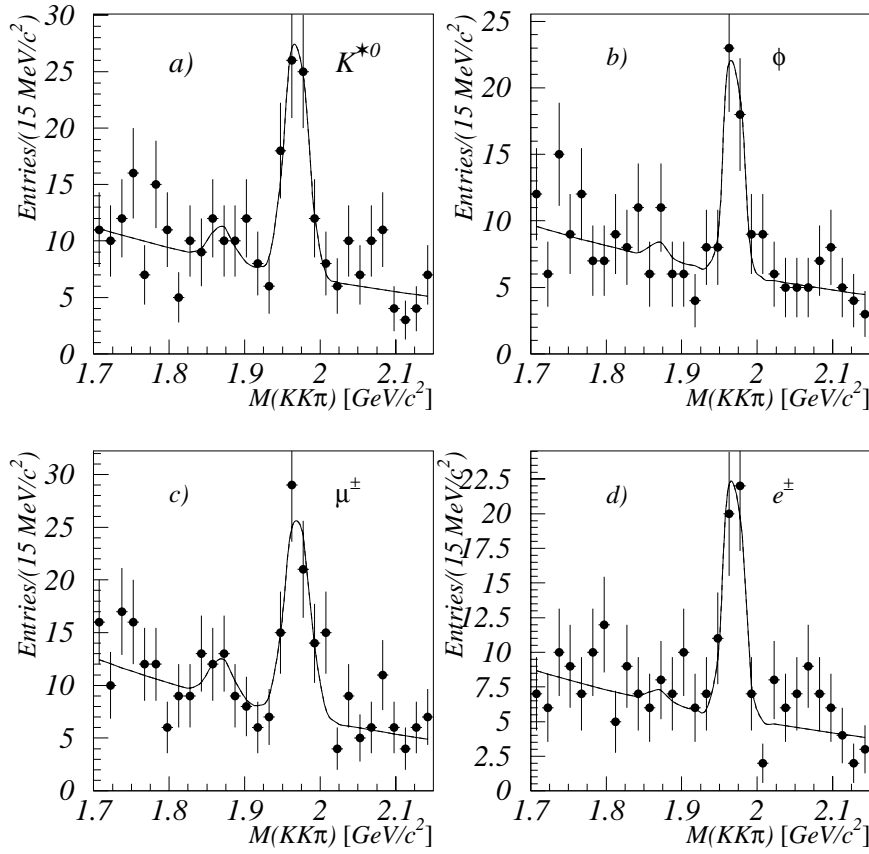
Figure 5.7: a) The KKπ invariant mass for the $D_s^{\pm} \to \overset{(-)}{K}{}^{*0}K^{\pm}$ decay mode. b) Same for the $D_s^{\pm} \to \phi\pi^{\pm}$. c) The invariant mass distribution for the $D_s^{\pm}\mu^{\mp}$ subsample. d) Same for the $D_s^{\pm}e^{\mp}$ subsample.

lated. The derivation of probabilities for an occurrence of a particular process, listed at the beginning of the chapter, per hadronic decay of the Z^0 is performed using the measured quantities of table 4.1. For the K^{*0} decay channel the branching ratio $Br(D_s^{\pm} \to \phi\pi^{\pm})$, used in quantities defined in table 4.1, is replaced by the branching ratio $Br(D_s^{\pm} \to \overset{(-)}{K}{}^{*0}K^{\pm})$.

I. α. The probability for the signal process, the semileptonic decay of a B_s^0 meson, may be expressed as

$$P_1^{B_s} = 2R_b Br(b \to B_s^0 \to D_s^- \ell^+ \nu X)[Br(D_s^- \to \phi\pi^-) +$$
$$+ Br(D_s^- \to K^{*0}\pi^-)] =$$
$$= 2R_b B_1 \left[1 + \frac{Br(D_s^- \to \phi\pi^-)}{Br(D_s^- \to K^{*0}\pi^-)}\right]. \tag{5.2}$$

β. A non-strange B decay into a $D_s K$ pair implies an intermediate D^{**} state. A crude estimation shows that only about 3-4% of non-strange D^{**} mesons produce a D_s meson in the final state (see Appendix A). A more refined analysis [35] results in an upper limit

$$\frac{Prob(Z^0 \to B_{u,d} \to D_s K \ell \nu X)}{P_1^{B_s}} < 10\%. \tag{5.3}$$

Hence this contribution to events in the $D_s^{\pm}\ell^{\mp}$ signal was neglected.

II. α. The relative occurrence of cascade decays of a non-strange B meson per hadronic Z^0 decay is

$$P_2^B = 2R_b Br(b \to B_{u,d} \to D_s X) Br(D_{ns} \to \ell \nu X)$$
$$[Br(D_s \to \phi\pi) + Br(D_s \to K^{*0}\pi)] =$$
$$= 2R_b B_2 B_{bcl} \left[1 + \frac{Br(D_s \to \phi\pi)}{Br(D_s \to K^{*0}\pi)}\right]. \tag{5.4}$$

The use of the inclusive semileptonic branching ratio B_{bcl}, measured in cascade decays, and of the inclusive $B_{u,d} \to D_s X$ branching fraction is justified, since D_s mesons are produced mainly through the emission of a $W^{\pm}$ and only a negligible contribution arises from a D^{**} intermediate state.

The production rate (5.4) is similar to the rate of the signal (5.2). However the cut on the transverse momentum

largely suppresses the former contribution. The ratio of efficiencies of the selected cuts for direct and cascade decays must be taken into account in order to estimate the fraction of cascade decays in the signal region. The ratio was evaluated on the simulated sample of B meson decays and found to be

$$R_{bcl} = \frac{\epsilon_{bcl}}{\epsilon_{B_s}} = 0.142 \pm 0.033 \ . \qquad (5.5)$$

β. Cascade decays of strange B's into two strange charmed mesons are treated as background. The probability for such process can be estimated from cascade decays of non-strange B mesons as

$$P_2^{B_s} = \frac{P_s}{2P_{u,d}} P_2^B \ . \qquad (5.6)$$

It is of the order of 10% of the P_2^B and only of the order of 2% of the signal and thus neglected.

III. Fake leptons are expected to contribute the same fraction of events to the signal region in the right and the wrong sign sample. Since no excess of events is observed in the wrong sign mass distribution (figure 5.6), this contribution was neglected.

IV. The D^+ meson decays into a $K^-\pi^+\pi^+$ final state non-resonantly and through the $\overline{K}^{*0}\pi^+$ channel. The resonant decay is around 5 times less frequent than the non-resonant one [5]. Because of the small width of the ϕ meson resonance the reflections in the D_s mass region, arising from the misidentification of one of the pions, are not seen in the ϕ decay mode of the simulated sample of D^+ decays. In the K^{*0} decay mode reflections appear as a broad accumulation in the $M(KK\pi)$ invariant mass distribution. In figure 5.8 one can see that the accumulation

is situated in the D_s mass region with the FWHM of around 130 MeV/c^2. By applying the selection criteria to simulated $b\bar{b}$ and $q\bar{q}$ events, the remaining contribution from the reflections with regard to the signal from the K^{*0} decay channel was determined to be

$$R_{ref} \; = \; \frac{\epsilon_{ref} N(ref)}{\epsilon_{B_s} N(B_s)^{K^{*0}}} \; = \; (7.6 \pm 3.3) \times 10^{-2} \,. \qquad (5.7)$$
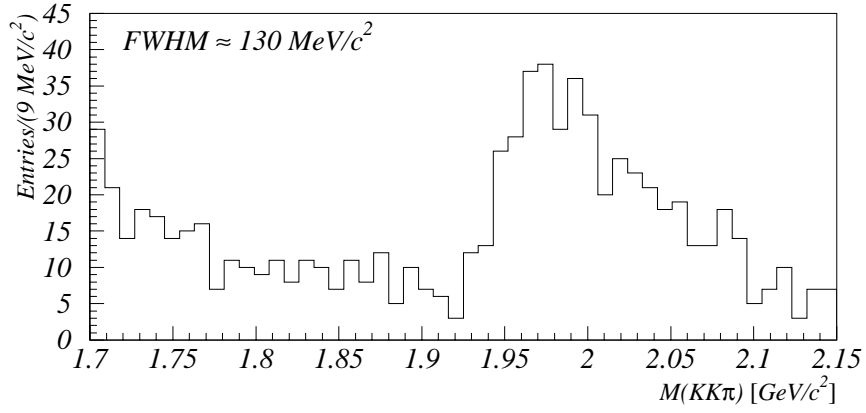

Figure 5.8: The invariant mass distribution of a $K\pi\pi$ combination by assigning the kaon mass to one of the pions. The distribution was obtained in the simulated sample of $B_{u,d} \to D^{\pm}\ell^{\mp}X$; $D^{\pm} \to K^{\mp}\pi^{\pm}\pi^{\pm}$ decays.

The above derived probabilities for individual processes, contributing to $D_s^{\pm}\ell^{\mp}$ correlations, enable the calculation of the B_s^0 purity in the sample used for the lifetime measurement:

$$
\begin{aligned}
f_{B_s} \; &= \; \frac{\epsilon_{B_s} N(B_s)}{\epsilon_{B_s} N(B_s) + \epsilon_{bcl} N(bcl) + \epsilon_{ref} N(ref)} \; = \\
&= \; \frac{1}{1 + R_{bcl}\frac{P_2^B}{P_1^{B_s}} + R_{ref} R_{K^{*0}}} \; = \\
&= \; 0.843 \; \pm \; 0.034 \,. \qquad (5.8)
\end{aligned}
$$

In the second line of equation (5.8) we used the fraction of $D_s^{\pm}$ candidates reconstructed in the K^{*0} decay channel,

$R_{K*0} = 0.63 \pm 0.20$.

The fraction of cascade decays in the signal region is

$$f_{bcl} = \frac{\epsilon_{bcl}N(bcl)}{\epsilon_{B_s}N(B_s) + \epsilon_{bcl}N(bcl) + \epsilon_{ref}N(ref)} =$$

$$= \frac{R_{bcl}\frac{P_2^B}{P_1^{B_s}}}{1 + R_{bcl}\frac{P_2^B}{P_1^{B_s}} + R_{ref}R_{K*0}} =$$

$$= 0.116 \pm 0.030 . \tag{5.9}$$

The fraction of reflections then follows from

$$f_{ref} = 1 - f_{B_s} - f_{bcl} \tag{5.10}$$

V. The contribution of the combinatorial background to the signal region was obtained from the fit to the invariant mass distribution of the $KK\pi$ combination. The fraction was found to be $f_{comb} = 0.382 \pm 0.044$.

5.4   Lifetime Measurement

5.4.1   Evaluation of the Proper Decay Time

The proper decay time of the B_s^0 meson was evaluated following the same steps as in the $\phi - \ell$ analysis. The $D_s^\pm$ track, calculated in the fit of the $KK\pi$ common vertex, was fitted into a common secondary vertex with the selected lepton. Similarly as in the $\phi - \ell$ analysis, vertices with the χ^2 probability less than 5×10^{-3} were rejected in order to improve the decay length resolution. For the 1992 and 1993 data the decay distance L was calculated using the relation (4.12) with the B_s^0 meson direction approximated by the momentum of the $D_s^\pm \ell^\mp$ system. The agreement between the polar angle of this momentum and the polar angle of the simulated B_s^0 flight direction

is shown in figure 5.9. The resolution is the same as for the approximation used for the $\phi\ell$ final state, but the non-Gaussian tails vanish. For the 1994 data the decay length was reconstructed in three dimensions.
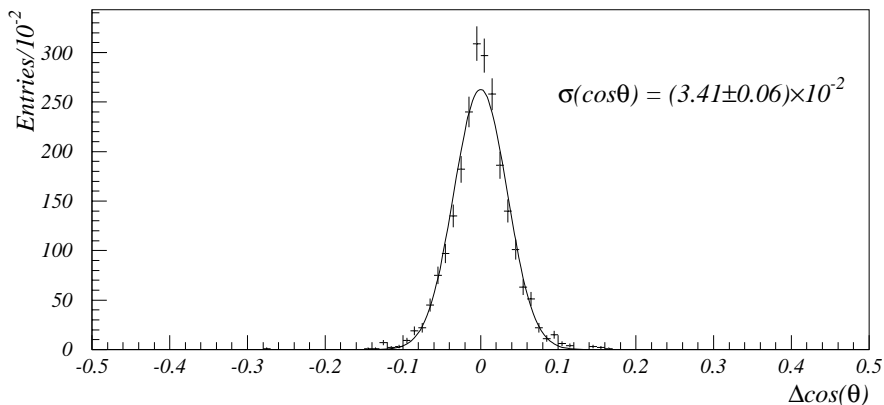

Figure 5.9: The difference between the simulated polar angle of a B_s^0 flight direction and the reconstructed polar angle of a $D_s^{\pm}\ell^{\mp}$ system.

As already mentioned in section 4.5.1, the precision of the decay length measurement improves for large angles between the final state tracks. In contrast to the $\phi - \ell$ analysis, the resolution on the decay length was now parametrized directly as a function of the angle between the direction of the identified lepton and the reconstructed direction of the D_s meson. This dependence is for positive decay lengths of the 1992 and 1993 simulated data plotted in figure 5.10.

The width of the $L_{gen} - L_{rec}$ distribution as a function of the $\cos\alpha(D_s\ell)$ was fitted with a linear function. For negative decay lengths a linear function was used to describe the dependence of the resolution on the decay length itself. This gave the following
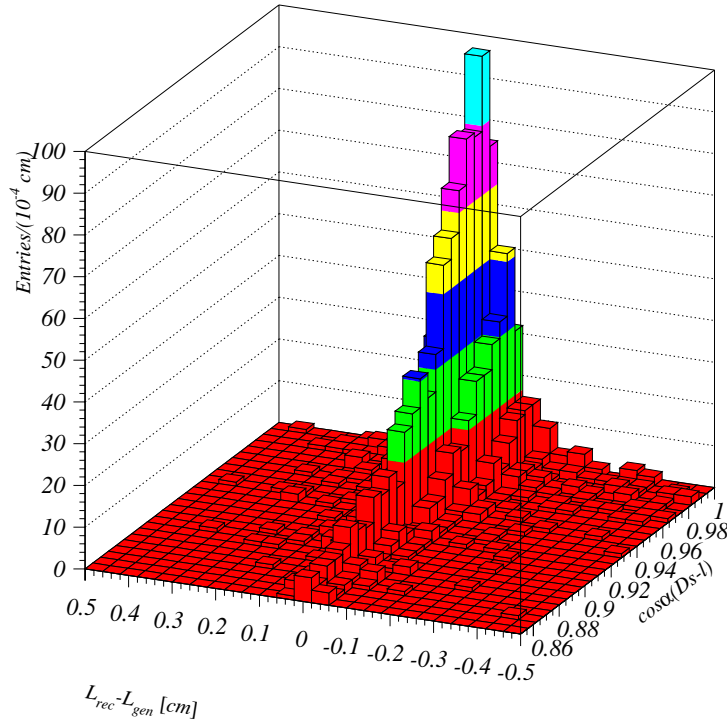
Figure 5.10: The dependence of the difference between the reconstructed and the simulated positive decay length on the angle between the $D_s^{\pm}$ meson and the $\ell^{\mp}$. The resolution improves for large angles. The distribution was obtained on the 1992 and 1993 simulated sample of B_s^0 decays.

overall parametrization of σ_L:

$$L > 0 :$$
$$\sigma_L = \begin{cases} a_L^+ + b_L^+ \cos\alpha(\mathrm{D_s}\ell) \; ; \; \cos\alpha(\mathrm{D_s}\ell) > m_\alpha \\ c_L \; ; \; \cos\alpha(\mathrm{D_s}\ell) < m_\alpha \end{cases}$$
$$L < 0 :$$
$$\sigma_L = a_L^- + b_L^- L \; . \tag{5.11}$$

Parameters obtained in two separated samples of simulated events are given in table 5.2 for '92-'93 and '94 data.

The average decay length resolution for the '92 and '93 sim-

	'92, '93	'94
a_L^+ [10^3 μm]	-2.353 ± 0.247	-3.028 ± 0.314
b_L^+ [10^3 μm]	2.756 ± 0.257	3.413 ± 0.325
c_L [μm]	205 ± 75	162 ± 26
m_α	0.928	0.935
a_L^- [μm]	259 ± 120	180 ± 110
b_L^-	-0.67 ± 0.40	-0.56 ± 0.34

Table 5.2: Parameters for evaluation of σ_L given by (5.11). Parameters were obtained by a fit to the simulated sample of B_s^0 decays.

ulated data is shown in figure 5.11. It was fitted with two Gaussian distributions, giving the width of approximately 765 μm for around 20% of events and 230 μm for 80% of events. For the '94 data the width was about 770 μm for 15% and 205 μm for 85% of events.
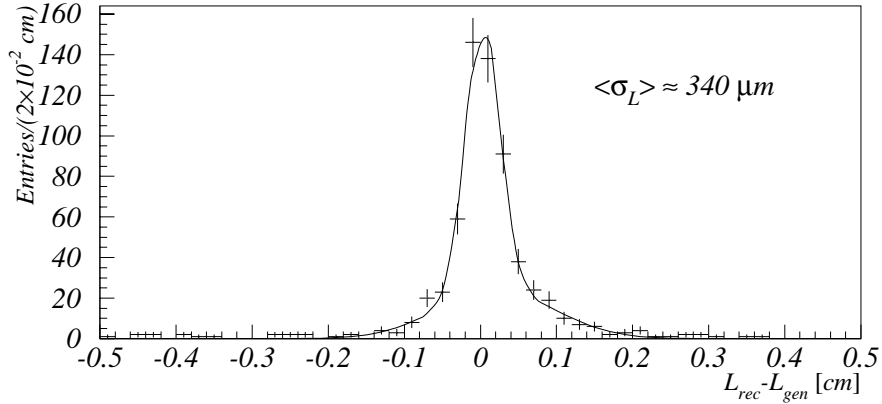
Figure 5.11: The average precision of the decay length determination for B_s^0 decays in '92 and '93 simulation.

A possible discrepancy between the simulation and real data in the decay length resolution has already been shown in figure 4.8 b). In the evaluation of systematic errors of the lifetime measurement σ_L was varied for $\pm$ 10% to account for this effect.

The reconstructed energy of the $D_s^\pm \ell^\mp$ system $E(D_s\ell)$ was

used as a basis for the B_s^0 meson energy estimation. Corrections
to this crude approximation were then applied in order to estimate
the B_s^0 momentum as accurately as possible.

For events with coincident directions of the event thrust axis
and of the thrust axis of the lepton jet, one can assume a two jet
topology, as sketched in figure 5.12.
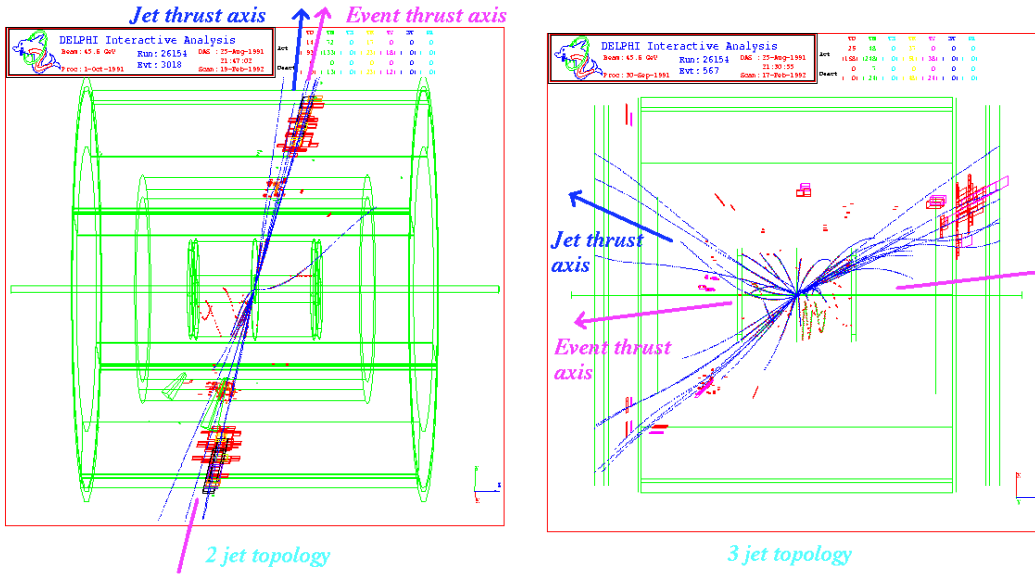
Figure 5.12: Computer reconstruction of a two- and three-jet event with
the Delphi spectrometer. Blue lines represent reconstructed tracks.
Parts of detectors are shown in green. Marked thrust axis are not the
result of reconstruction and are shown for explanation of the text only.

The energy of the beams E_b thus agrees with the energy of the
jets. For such events the difference between the beam energy and
the reconstructed energy of the jet is expected to be correlated with
the energy of a neutrino, produced in a semileptonic B decay. The
remainder of the B_s^0 meson energy, not taken by the $D_s^{\pm}\ell^{\mp}$ system, is
shown in figure 5.13 as a function of the difference between the E_b
and $c p_{jet}$. p_{jet} is the sum of momenta of charged tracks in the jet.

The distribution is shown only for events with the angle between the event thrust axis and the lepton jet axis α_{tj} smaller than $5°$.
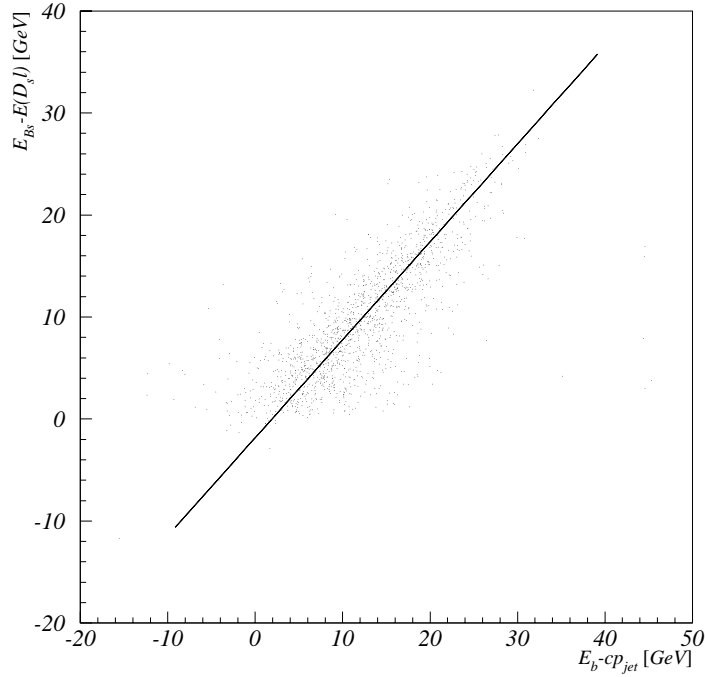
Figure 5.13: The distribution of the difference between the B_s^0 meson energy and the energy of the $D_s^\pm \ell^\mp$ system versus the difference of the beam energy and the jet momentum multiplied by c. The distribution is obtained from the simulated B_s^0 decays satisfying the requirement $\alpha_{tj} < 5°$. The full line represents the energy parametrization described by (5.13).

The two dimensional distribution, shown in figure 5.13, was fitted with a double Gaussian of the form

$$Ae^{-\frac{(x'-x_0')^2}{2\sigma_x^2}} e^{-\frac{(y'-y_0')^2}{2\sigma_y^2}} \tag{5.12}$$

with coordinates of the rotated system $x' = x\cos\beta + y\sin\beta$ and $y' = -x\sin\beta + y\cos\beta$. From fitted parameters of (5.12) the estimate of the E_{B_s} was obtained as a function of $E(D_s\ell)$, E_b and p_{jet},

for events with $\alpha_{tj} < 5°$.

For events with the angle between the event thrust axis and the lepton jet axis larger than $5°$, the average difference between the E_{B_s} and $E(D_s\ell)$, found in the simulation, was added to the reconstructed energy of the meson and the lepton. The momentum of the B_s^0 meson, needed for the lifetime calculation from (4.10), is given by $cp_{B_s} = \sqrt{E_{B_s}^2 - M_{B_s}^2 c^4}$, with the final parametrization of a strange B meson energy

$$
E_{B_s} = \begin{cases} E(D_s\ell) + a_E(E_b - cp_{jet}) + b_E \; ; \; \alpha_{tj} < 5° \\ E(D_s\ell) + c_E \; ; \; \alpha_{tj} > 5° \end{cases}. \tag{5.13}
$$

The values of parameters, obtained by the fit to simulated distributions, are a_E=0.96±0.02, b_E=(-1.83±0.25) GeV and c_E=(7.1±0.2) GeV. The dependence of the relative energy resolution on the B_s^0 energy is shown in figure 5.14. It was fitted with a linear function

$$
\frac{\sigma(E_{B_s})}{E_{B_s}} = a_\sigma E_{B_s} + b_\sigma \tag{5.14}
$$

with the resulting parameters a_σ=(-7.0±0.6)×10^{-3} GeV^{-1} and b_σ=0.35±0.02. The average precision of the E_{B_s} estimation was around 9.5%.

The resolution on the p_{B_s}, which enters the relation (4.11) for the calculation of the precision on the proper decay time evaluation, is $\sigma(p_{B_s}) = E_{B_s}\sigma(E_{B_s})/p_{B_s}$. Note that the average value of the E_{B_s}/p_{B_s} ratio differs from unity for less than 2%. The resolution σ_t was calculated separately for each individual event of the signal region, used for the lifetime measurement, from σ_L and $\sigma(p_{B_s})$.

Figure 5.15 shows the comparison of the B_s^0 energy distribution between data and the Monte Carlo simulation. For real data, the distribution obtained in the side bands of the invariant mass $1.7 < M(KK\pi) < 1.8$ GeV/c^2 and $2.05 < M(KK\pi) < 2.15$ GeV/c^2
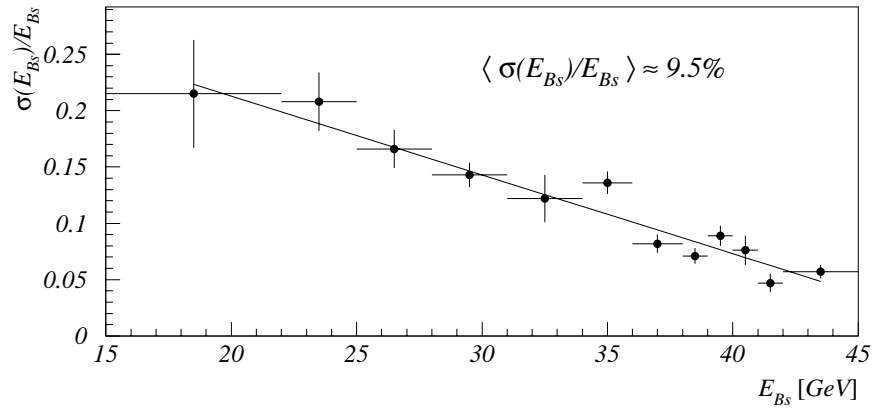
Figure 5.14: The dependence of the relative B_s^0 energy resolution on the energy itself. The dependence was fitted with a linear function on the selected sample of simulated strange B decays.
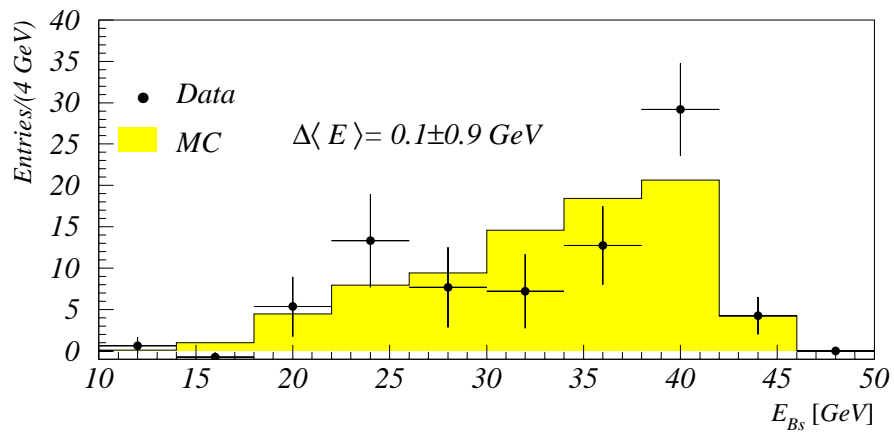
Figure 5.15: The comparison of the B_s^0 energy distribution for the real and the simulated data sample. The distribution of real events in the signal region is obtained by subtracting the energy distribution of events in the side bands of the $M(KK\pi)$ distribution. The simulated sample was obtained by applying the described selection criteria to Monte Carlo B_s^0 decays.

was subtracted from the distribution of events in the signal region. The difference in the mean of the two distributions was found to be 0.1±0.9 GeV. The smaller number of events obtained in this analysis, compared to the $\phi\ell$ final state, reflects in a higher statistical error on $\Delta\langle E\rangle$. The error was again used to estimate the systematic error on the lifetime measurement arising from the possible difference between the simulated and the real sample of events.
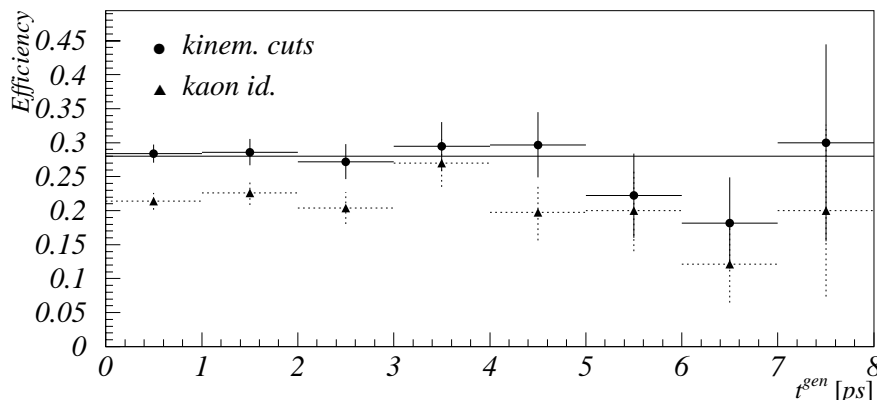
Figure 5.16: The dependence of selection criteria efficiency on the proper decay time of simulated B_s^0 decays. Dots represent the efficiency after kinematical cuts and triangles after the inclusion of particle identification requirements described in the text.

The influence of the selection criteria on the decay time dependence of the efficiency can be seen in figure 5.16. The plot does not include the geometrical acceptance of the VD due to the requirement of at least one associated hit per final state track. The efficiency behaviour is flat apart from the two bins at high proper decay times where the statistics is low. Within the statistical error the efficiency is thus consistent with a constant value over the range of the decay times used for the lifetime measurement. A χ^2 fit of a constant to the efficiency of kinematical selection criteria

yields the value (28 ± 9) %. As described in section 4.5.3, possible small deviations were taken into account by studying the fitted lifetime of the simulated sample in the same manner as in the $\phi - \ell$ analysis.

5.4.2 Likelihood Fit

The unbinned maximum likelihood fit was performed on $D_s^\pm \ell^\mp$ events with 1.941 GeV/c^2 < $M(KK\pi)$ < 1.995 GeV/c^2. The likelihood function included all non-negligible contributions evaluated in section 5.3. The form of the function, describing the probability distribution of different sources, was

$$
\begin{aligned}
\mathcal{L} = \prod_{i=1}^{N_{sig}} & (1 - f_{comb})(1 - f_{bcl} - f_{ref})\mathcal{P}_{B_s}(t_i, \sigma_{t_i}, \tau_{B_s}) \; + \\
+ \; & (1 - f_{comb})f_{bcl}\mathcal{P}_{bcl}(t_i, \sigma_{t_i}, \tau_{bcl}) \; + \\
+ \; & (1 - f_{comb})f_{ref}\mathcal{P}_{ref}(t_i, \sigma_{t_i}, \tau_{ref}) \; + \\
+ \; & f_{comb}\mathcal{P}_{comb}(t_i, \sigma_{t_i}, \tau_+, \tau_-, f_{comb}^+, f_{comb}^G, \sigma_{comb})
\end{aligned}
$$
(5.15)

The probability density distribution for B_s^0 decays $\mathcal{P}_{B_s}$ was of the same form as in the $\phi - \ell$ analysis given by (4.16). The convolution of an exponential and a Gaussian distribution was also used for the parametrization of probability functions for cascade decays $\mathcal{P}_{bcl}$ and for the contribution from D^+ reflections $\mathcal{P}_{ref}$. The average value of the $B_{u,d}$ meson lifetime $\tau_B = (1.60 \pm 0.04)$ ps [34] was assumed for the mean lifetime of the reflection contribution τ_{ref}.

The mean lifetime of cascade decays τ_{bcl} was obtained from the likelihood fit of the simulated sample. The proper decay time distribution and the result of the fit with $\mathcal{P}_{bcl}$ as a fitting function is plotted in figure 5.17 c). The fitted lifetime was $\tau_{bcl} = (2.2 \pm 0.2)$ ps. This value is higher than the average value τ_B due to the underes-

timation of a B meson momentum in this category of events. By simply comparing the mean value of the estimated momentum of decaying B mesons for direct and cascade decays one can expect a shift of around 20% to 25% in the lifetime. The value close to 2 ps is thus understandable.

The proper decay time distribution of the combinatorial background was taken from the side bands of the right sign $M(KK\pi)$ distribution, as well as from the entire interval of the wrong sign $M(KK\pi)$ distribution, shown in figure 5.6. Since no excess of events was found in the $D_S^\pm$ mass region for the wrong sign combinations, we can conclude that these events have the same origin as the background events in side bands of the right sign invariant mass distribution. A study of decay times for this category of events suggested the following term for the probability density function:

$$\mathcal{P}_{comb} = f_{comb}^G G(t_i, \sigma_{comb}) + f_{comb}^+ E(t_i, \tau_+) \otimes G(t_i, \sigma_{t_i}) +$$
$$+ (1 - f_{comb}^G - f_{comb}^+) E(-t_i, \tau_-) \otimes G(-t_i, \sigma_{t_i})$$
$$(5.16)$$

The form of (5.16) slightly differs from the function (4.17) used to describe the same source of background in the $\phi\ell$ sample. The difference might be attributed to the presence of another charged track used to reconstruct secondary vertices. In the $\phi\ell$ final state the resolution on the decay length for all categories of events, including the combinatorial background, was mainly determined by a high p_t track due to the small opening angle of particles forming the ϕ candidate. Hence the resolution σ_t was assumed the same for all types of events. In the present analysis the influence of a high p_t track is diluted by the presence of an additional charged track forming a pseudo-scalar meson. For the combinatorial background these tracks do not originate from a common vertex. The consequence is a larger smearing in the secondary vertex recon-

struction. This is described by the first and the last term of (5.16). The first term is a Gaussian, centred at zero. The last term is a convolution of an exponential and a Gaussian, with decay time τ_- describing a small tail at negative decay times. The second term of (5.16) describes events with the correctly assigned lepton from long living particles.

The decay time distribution of the combinatorial background is shown in figure 5.17 b). The likelihood fit to the distribution yielded $f_{comb}^G = 0.401 \pm 0.063$, $f_{comb}^+ = 0.520 \pm 0.046$, $\tau_+ = (1.28 \pm 0.11)$ ps, $\tau_- = (0.42 \pm 0.26)$ ps and $\sigma_{comb} = (0.283 \pm 0.037)$ ps. Since the sample is enriched in $b\bar{b}$ decays the value of τ_+ is approaching the mean lifetime of B mesons. Due to the miss-assigned tracks, not originating from B decays, the fitted value is slightly lower than τ_B.

The proper decay time distribution of the selected sample of $D_s^{\pm}\ell^{\mp}$ events is plotted in figure 5.17 a). The result of the maximum likelihood fit is superimposed, shown together with the contributions from the combinatorial background and cascade decays. The fitted lifetime of B_s^0 mesons was

$$\tau_{B_s} = (1.41 \pm 0.26(\text{stat.})) \text{ ps .} \tag{5.17}$$

The obtained result was again cross-checked by the fit to the simulated sample of B_s^0 decays, processed through the same selection criteria as applied to the real data. With the generated lifetime of 1.6 ps the result was $\tau_{B_s} = (1.535 \pm 0.069)$ ps.

5.4.3 Systematic errors

In order to evaluate systematic errors on the lifetime measurement, first all the parameters entering the likelihood fit were varied by
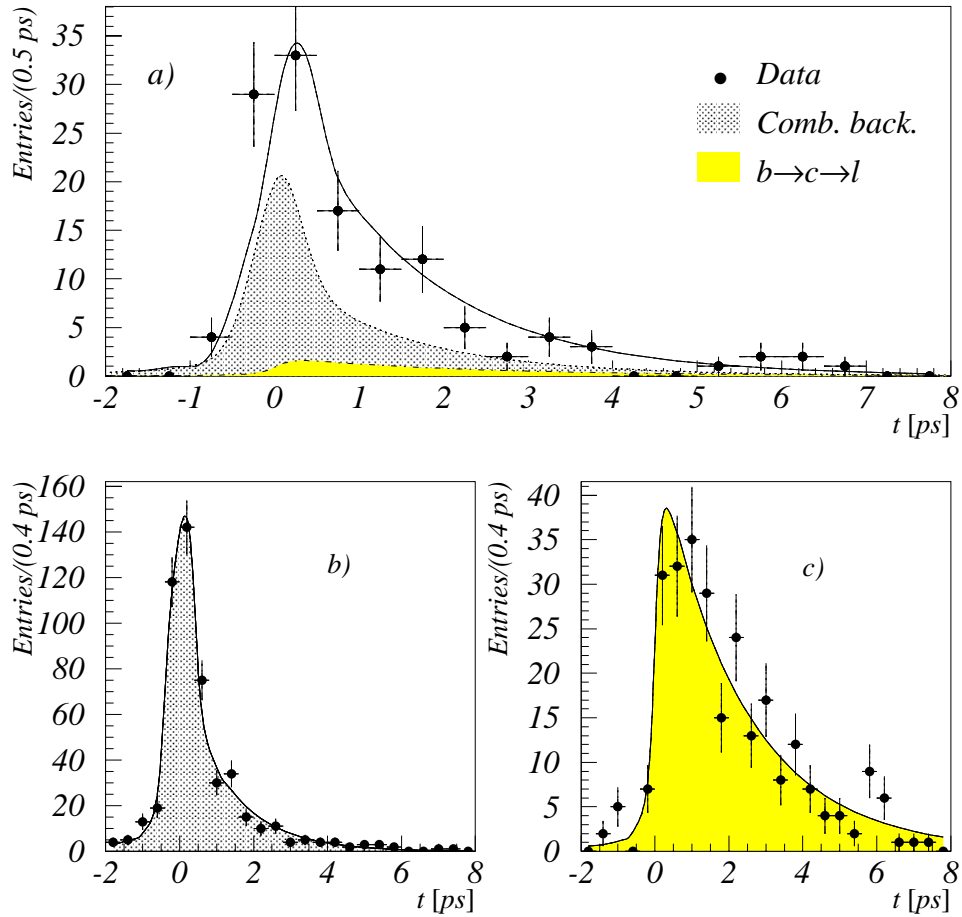
Figure 5.17: a) The proper decay time distribution of selected $D_s^\pm \ell^\mp$ events. The result of the maximum likelihood fit is shown superimposed. Shaded regions represent contributions of the combinatorial background and of cascade B decays. b) Same distribution for the combinatorial background obtained in the side bands of the right sign $M(KK\pi)$ invariant mass and in the wrong sign combinations $D_s^\pm \ell^\pm$. c) The proper decay time distribution for cascade decays obtained on the simulated sample.

one standard deviation from their average value and the fit was repeated. The parameters obtained in a separate fit of the combinatorial background were varied according to the resulting correlation coefficients. As can be seen in table 5.3, the largest contribution from this class of systematic errors arises from parameters describing the combinatorial background, particularly from the fraction f_{comb}. A similar feature was observed in the $\phi\ell$ sample as well. Due to a smaller relative background contribution the error arising from this source is lower in the present analysis.

Source of systematic error	τ_{B_s} variation [ps]
Combinatorial background (f_{comb}, f^G_{comb}, f^+_{comb}, τ_+, τ_-)	$+0.062$ -0.066
Cascade decays (f_{bcl}, τ_{bcl})	$+0.033$ -0.034
Reflections (f_{ref}, τ_{ref})	$+0.004$ -0.004
Difference data/MC in p_{B_s} eval.	$+0.042$ -0.040
Difference data/MC in σ_L	$+0.015$ -0.006
Possible analysis bias	$+0.066$ -0.066
Total	$+0.106$ -0.107

Table 5.3: Summary of systematic errors on the B^0_s lifetime measurement for the $D^{\pm}_s \ell^{\mp}$ analysis.

A possible discrepancy between the Monte Carlo simulation and real data was checked in the same manner as for the $\phi - \ell$ analysis. σ_L was varied by $\pm$ 10%, as already discussed in section 4.5.1, and the corresponding variation of the fitted lifetime was accounted for in the list of systematic errors. Another source in this class of the systematics is the B^0_s momentum. It was calculated from the estimated energy E_{B_s}. This quantity was varied in each of the events entering the likelihood fit for ± 0.9 GeV, the amount found when comparing real and simulated energy distributions. Due to a larger statistical error of this difference the error from

this source is larger than the one in the $\phi - \ell$ analysis.

The last class of systematic errors are possible limitations of the modelling used. A hint of a non perfect parametrization of the likelihood function can be seen in the first negative bin of the proper decay time distribution in figure 5.17 a), which deviates from the fitted function by around 2σ. Together with the acceptance deviations from the constant and parametrizations of p_{B_s} and σ_L, these effects were accounted for by the lifetime found in the simulated sample. The measured lifetime was corrected for the ratio of the generated and the fitted lifetime of simulated B_s^0 decays. The ratio $r_{corr} = 1.0423 \pm 0.0469$ was found to be larger than in the $\phi\ell$ case but still within the statistical error of the fit, performed on the simulated sample. Because of the correction the error $\sigma(r_{corr})\tau_{B_s}$ was added in quadrature to other systematic errors of the measurement and the statistical error was corrected by r_{corr}.

With the inclusion of systematic effects the lifetime of B_s^0 mesons, determined from the $D_s^\pm \ell^\mp$ sample, is

$$\tau_{B_s} = \left[1.47 \pm 0.27 (\text{stat.}) \pm 0.11 (\text{syst.}) \right] \text{ps} .$$

(5.18)

Part IV

Summary

Chapter 6

Combination of the Results

To combine results of the two analyses, differing in the reconstructed final state, one should first consider the statistical correlation between the two samples of events. From the production mechanism point of view all the events reconstructed in the ϕ decay mode of the $D_s^\pm \ell^\mp$ analysis are expected to be included in the $\phi\ell$ sample. The first effect that lowers this ratio is due to the larger sample of hadronic Z^0 decays, used in the reconstruction of $D_s^\pm$ mesons. Because of the slight differences in cuts, used for the different data taking periods, the 1992 data represent around 1/3 of the final sample. Hence only 2/3 of $D_s^\pm$ mesons reconstructed through the $\phi\pi^\pm$ decay channel are expected to be in common with the selected events of the $\phi - \ell$ analysis. Another cause of the dilution of the overlap is the relative fraction of the $\phi\pi^\pm$ decay mode in the overall $D_s^\pm \ell^\mp$ signal. This amounts to approximately 40%. Thus one would expect around $0.4 \times 2/3 \approx 25\%$ of the $D_s^\pm$ candidates, reconstructed in the ϕ decay mode, to be the same as events in the ϕ mass region of the $\phi\ell$ sample. However, differences in the selection criteria, used for isolation of the two samples, can cause different events of the $D_s^\pm \to \phi\pi^\pm$ decay channel to be selected in the two samples. Because of that, the value of around 25% is an

upper limit for the expected statistical overlap of both signals.

By comparing the event numbers in both selected samples and under the reasonable assumption that common events do not originate from non-physical sources of background, e.g. the combinatorial background, 6 ± 3 % of events were found to be the same.

The common systematic error of the two measurements might arise due to the used branching ratios in the calculation of specific contributions. This would connect the errors arising from the cascade background in the $D_s^{\pm} \ell^{\mp}$ analysis and from the B_s purity in the $\phi \ell$ final state. These two errors, quoted in tables 5.3 and 4.2, are partially correlated, and the amount of the common part for the two errors was found to be ± 0.008 ps.

Another source of the common systematics is the tracking performance of the Delphi spectrometer. Since this is the same for the two samples and the same sample of simulated events was used for the study of the possible difference in the decay length resolution, errors due to σ_L may be considered completely correlated. The common part of the errors, arising from this source, is $^{+0.015}_{-0.006}$ ps. The difference between the Monte Carlo and real data in the p_{B_s} estimation were studied using two different simulated samples. The algorithms of the calculation differ as well and the errors from this source were assumed to be uncorrelated.

A small correlation in the systematic errors of the two measurements originates from the use of the average B meson lifetime in both analysis. The error, which is in common to both analyses due to this reason, was found to be ± 0.002 ps.

Quadratic sum of systematic errors, which are common to both analysis, is $^{+0.017}_{-0.010}$ ps. This value is small compared to overall systematic errors of the two individual results. It was verified that

statistical and systematical correlations are too small to influence the combined result of the measurements, derived below.

The most common approach to combining results of different measurements is to calculate the mean of individual results, weighted according to their errors:

$$\overline{\tau} = \frac{\sum_i w_i \tau_i}{\sum_i w_i}$$

$$w_i = \frac{1}{\sigma_i^2} . \tag{6.1}$$

τ_i are measurements to be combined, and σ_i the corresponding errors. The error on the average value $\overline{\tau}$ then follows as

$$\sigma_{\overline{\tau}} = \left(\sum_i \frac{1}{\sigma_i^2}\right)^{-\frac{1}{2}} . \tag{6.2}$$

However, since the underlying distribution of lifetime measurements is exponential, with $\sigma_\tau \propto \tau$, the fluctuation of a single measurement to lower values would result in a lower statistical error of the measurement. If in averaging procedure the absolute errors of measurements would be used as weights, this might bias the average [36]. The average of lifetime measurements was thus performed using relative errors as weights in order to avoid biases:

$$\overline{\tau} = \frac{w_1 \tau_1 + w_2 \tau_2}{w_1 + w_2}$$

$$w_i = \frac{\tau_i^2}{\sigma_i^2} . \tag{6.3}$$

The uncertainty of $\overline{\tau}$ can be calculated to be

$$\left(\frac{\sigma_{\overline{\tau}}}{\overline{\tau}}\right)^2 = \left[\frac{3w_1}{w_1 + w_2\frac{\tau_2}{\tau_1}} - \frac{2w_1}{w_1 + w_2}\right]^2 \left(\frac{\sigma_1}{\tau_1}\right)^2 +$$

$$+\left[\frac{3w_2}{w_2 + w_1\frac{\tau_1}{\tau_2}} - \frac{2w_2}{w_1 + w_2}\right]^2 \left(\frac{\sigma_2}{\tau_2}\right)^2 . \tag{6.4}$$

In case of correlation, part of the systematic errors, common to both measurements, is quadratically subtracted from the individual errors. Due to the statistical overlap of the two samples,

statistical errors are increased by the appropriate factor, considering that the statistical errors scale as $1/\sqrt{N}$, with N being the number of signal events. The resulting systematic and statistical errors are then used as weights for averaging. Finally, common systematic errors are added in quadrature to the error on the average lifetime. Since the correlation between the two performed measurements is small, the result of such a procedure does not differ from the average, obtained by neglecting the correlation.

The combined value of the B_s^0 lifetime from the $D_s^\pm \ell^\mp$ and $\phi\ell$ sample is

$$\tau_{B_s} = (1.66 \pm 0.19) \text{ ps} . \tag{6.5}$$

Chapter 7

Conclusions

The present work evolved from the studies of B_s^0 meson properties with the Delphi spectrometer ever since the first evidence for the B_s^0 meson production in Z^0 decays in 1992 [37]. Since then, experimental methods have been developed, and the number of accumulated B_s^0 decays has been substantially increased.

The measurement of the B_s^0 meson lifetime was performed using two to some extent complementary samples of events. For the first time the sample with the reconstructed ϕ meson accompanied by a high transverse momentum lepton in the same jet was used for such measurement. The selected inclusive decay channel profits from a relatively high statistics. The statistical power of the sample is of large importance in B_s^0 lifetime measurements since with the sources of B mesons presently available they are still limited by the statistical precision (see the summary of B_s^0 meson lifetime measurements in figure 7.1). The selection of leptons with a high p_t enriches the isolated sample in direct semileptonic B decays. The reconstruction of ϕ mesons in the final state raises the fraction of strange B mesons among all the B mesons from around 11%, found in $Z^0 \rightarrow b\bar{b}$ decays, to (50 ± 7)%. By the use of the Delphi Vertex Detector the determination of the decay length and hence

of the proper decay time is possible. The maximum likelihood fit
of the decay time distribution for events in the $\phi\ell$ sample resulted
in the B_s^0 lifetime of

$$\tau_{B_s} = \left[1.75 \pm 0.20(\text{stat.}) \begin{subarray}{l} +0.15 \\ -0.11 \end{subarray} (\text{syst.})\right] \text{ps} . \qquad (7.1)$$

A more exclusive decay channel, with a reconstructed $D_s^\pm$ me-
son and a lepton of the opposite charge in the same jet, offers a
higher purity of B_s^0 mesons. A cut on the transverse momentum of
the lepton again enriches the sample of events in semileptonic de-
cays of B mesons. The reconstruction of a strange charmed meson
through its decays into $\phi\pi$ and $K^{*0}K$ final states results in the B_s^0
purity of 0.843 ± 0.034. Due to a higher signal to noise ratio the
systematic error of the lifetime measurement on the selected sam-
ple is somewhat lower than the corresponding error in the $\phi - \ell$
analysis. The result of the maximum likelihood fit of the proper
decay time distribution was

$$\tau_{B_s} = \left[1.47 \pm 0.27(\text{stat.}) \pm 0.11(\text{syst.})\right] \text{ps} . \qquad (7.2)$$

The common statistical and systematical errors of the two
measurements were found to be small. The results were combined
using the weighted average. The mean B_s^0 lifetime is

$$\tau_{B_s} = (1.66 \pm 0.19) \text{ps} . \qquad (7.3)$$

Figure 7.1 places the obtained results in the world summary
of B_s^0 lifetime measurements. Full error bars show the quadratic
sum of statistical and systematical errors while vertical lines indi-
cate the amount of statistical errors alone.

Currently the most precise individual measurement is per-
formed by the Aleph collaboration [38] using $D_s^\pm\ell^\mp$ correlations.
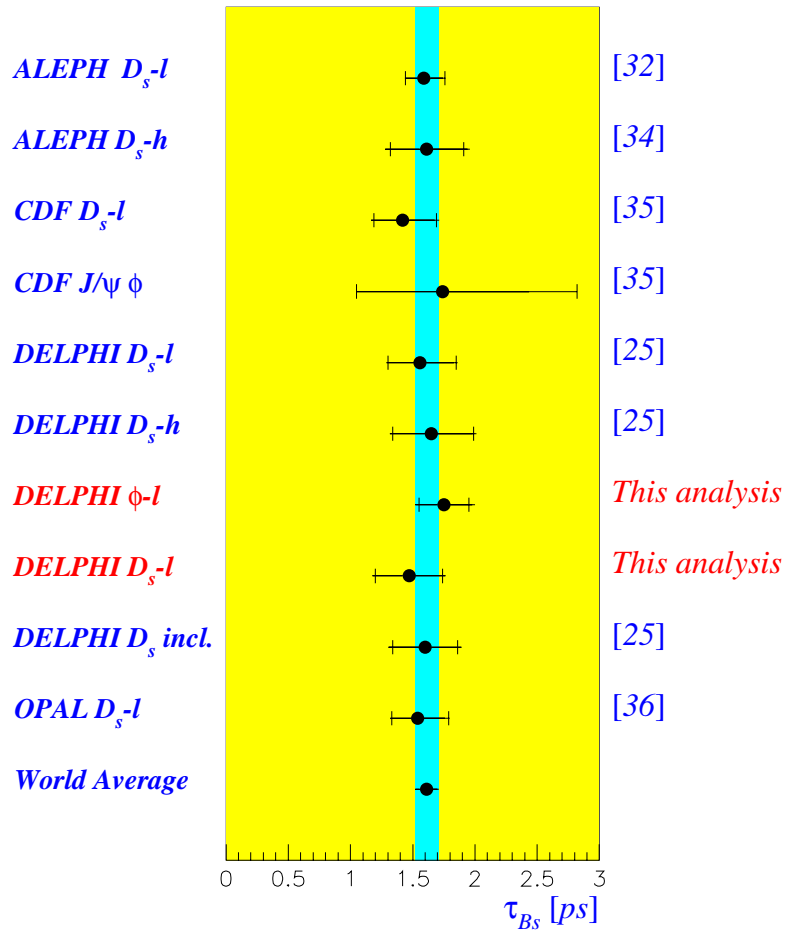
Figure 7.1: The world summary of published measurements of the B_s^0 lifetime. On the right side references of publications are indicated. Vertical lines on the error bars indicate the amount of the statistical error in the quadratic sum of the statistical and systematical error, represented by the full line. The world average was taken from [39].

The small statistical error of the measurement is the result of five $D_s^{\pm}$ decay channels, used in addition to the two presented in our analysis. Following in precision is the result of the $\phi - \ell$ analysis of the current work. The world average was calculated by the LEP B Lifetime Working Group for the 1996 edition of the Review of

Particle Properties [39]. For the average calculation the previously published result of the $D_s^\pm \ell^\mp$ analysis of the Delphi collaboration [31] was used. The lifetime obtained on the $\phi\ell$ sample contributes to the world average with a weight of approximately 17%.

The ratio of the measured B_s^0 lifetime (7.3) and of the world average for the B_d^0 meson lifetime [39] is calculated to be

$$\frac{\tau_{B_s}}{\tau_{B_d}} = 1.06 \pm 0.13 , \qquad (7.4)$$

neglecting possible systematic correlations. Unfortunately the precision of the B_s^0 lifetime measurement is not sufficient to make any statements on adequateness of the models, described in chapter 2, which are used to predict lifetime differences between individual B meson species. Even if one uses the world average for τ_{B_s}, the ratio

$$\frac{\tau_{B_s}}{\tau_{B_d}} = 1.03 \pm 0.07 \qquad (7.5)$$

is completely compatible with unity.

The ratio of the measured lifetime and the world average of the charged B meson lifetime is

$$\frac{\tau_{B^+}}{\tau_{B_s}} = 0.98 \pm 0.12 , \qquad (7.6)$$

with the error which is larger than the expected digression from unity. With the world average value of τ_{B_s} one obtains

$$\frac{\tau_{B^+}}{\tau_{B_s}} = 1.01 \pm 0.07 , \qquad (7.7)$$

the value which is not so far from the limit, predicted by the non-spectator effects: for $f_B = 200$ MeV one would anticipate the ratio of 1.05.

In the future, the $\phi\ell$ inclusive decay channel can be used for the study of B_s^0 meson oscillations. Due to the limited statistics the measurement of the oscillation frequency in the B_s^0 system has

not been performed yet and only lower limits exist. They are additionally lowered by systematic uncertainties, one of which is the uncertainty of the measured B_s^0 lifetime. It is difficult to estimate the amount of these systematic effects produced by the error on the average τ_{B_s}. Hopefully, better knowledge of the lifetime will improve results of such analysis as well as enable the future study of B_s^0 decay properties.

Part V

Povzetek doktorskega dela

Poglavje 8

8.1 Uvod

Standardni model močne in elektrošibke interakcije [1] je dandanes ena najbolj uveljavljenih teorij v fiziki osnovnih delcev. Prve eksperimentalne potrditve modela segajo v leto 1973, z odkritjem nevtralnega šibkega toka, katerega nosilec je nevtralni šibki bozoni. V letu 1983 sta skupini znanstvenikov, zbranih ob spektrometrih UA1 ter UA2, uspeli neposredno potrditi obstoj nevtralnih in nabitih šibkih bozonov [3]. Natančne meritve parametrov modela, ter s tem testi njegovih napovedi, pa so bili mogoči šele šest let kasneje, z začetkom obratovanja elektronsko-pozitronskega trkalnika LEP v Evropskem laboratoriju za fiziko osnovnih delcev (CERN) v Ženevi. Elektroni in pozitroni, pospešeni v trkalniku LEP, pri trčenju tvorijo nevtralni šibki bozon Z^0. Meritve produkcijskih in razpadnih lastnosti bozona Z^0 so potrdile napovedi teorije Standardnega modela z izjemno natančnostjo.

Bozon Z^0 razpada v par leptonov ali par kvarkov. Okoli 22% razpadov $Z^0 \rightarrow q\overline{q}$ predstavljajo razpadi v pare $b\overline{b}$ [6]. Zaradi tega je trkalnik LEP primeren za študij hadronov, sestavljenih iz kvarkov b. Fizika kvarkov b je bila pomembno področje raziskav na trkalnikih elektronov in pozitronov že pred konstrukcijo trkalnika LEP. Prednosti slednjega izvirajo iz višje razpoložljive energije

trkov. Težiščna energija trka na LEP je namreč enaka masi bo-
zona Z^0 , M_Z = (91.1885 ± 0.0022) GeV/c^2 [6]. Hadroni, ki nas-
tanejo iz kvarka in antikvarka ob razpadu Z^0 , imajo zaradi višje
energije daljše razpadne razdalje. Rekonstrukcija razpadnih raz-
dalj s pomočjo polprevodniških detektorjev pa omogoča meritev
življenjskih časov nastalih delcev. Poleg tega razpad nevtralnega
šibkega bozona omogoča nastanek celotnega spektra hadronov, ki
vsebujejo kvark b. S trkalnikom LEP lahko prvič rekonstruiramo
mezone B_s^0 in merimo življenjski čas barionov Λ_B.

Pričujoče delo opisuje meritev življenskega časa mezonov B_s^0.
Ta čas je znan z najmanšo natančnostjo med življenjskimi časi treh
različnih mezonov B: B_s^0 , B^+ in B_d^0 [1]. Razpadne lastnosti mezonov
B_s^0 niso podrobno izmerjene, saj so bili le-ti eksperimentalno potr-
jeni šele leta 1992 [37]. Življenjski čas bo v bodočnosti potreben
za izračun razpadnih širin iz izmerjenih razvejitvenih razmerij. Za
razpade hadronov, sestavljenih iz kvarkov b, so odgovorni različni
procesi, njihov prispevek pa je odvisen od sestave posameznega
delca. Ob zadostni natančnosti lahko z meritvijo življenjskih časov
posameznih hadronov b sklepamo o pomembnosti različnih pro-
cesov, udeleženih pri razpadih. Poznavanje življenjskega časa pa
je tudi nujen pogoj za meritev frekvence oscilacij mezonov B_s^0.
Meritev te količine zaenkrat še ni mogoča zaradi premajhnega števila
zabeleženih razpadov B_s^0 , predstavlja pa motivacijo za nadaljnje
raziskave na področju fizike mezonov B.

Meritev smo izvedli na dveh vzorcih semileptonskih razpadov
mezonov B_s^0. Vzorec, sestavljen iz dogodkov z rekonstruiranim
mezonom ϕ in leptonom v istem hadronskem pljusku, omogoča

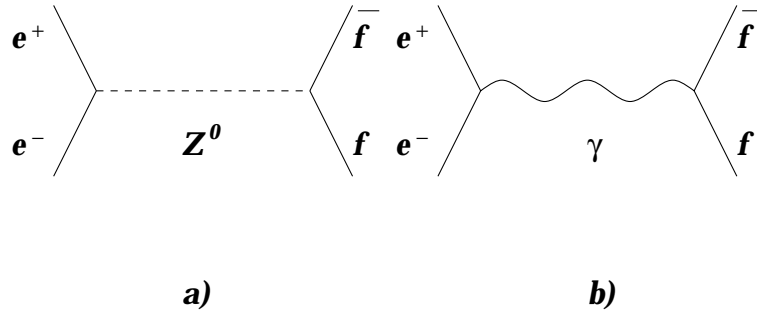[1]Mezon B_s^0 je setavljen iz antikvarka $\overline{b}$ in kvarka s. Mezon B^+ sestavlja par $\overline{b}$u in
mezon B_d^0 par $\overline{b}$d. Če ni posebej označeno, je pri oznakah delcev vedno privzeta us-
trezna trditev za nabojno konjugirano stanje.

eno statistično najnatančnejših meritev življenjskega časa B_s^0. Dogodki, ki vsebujejo mezon $D_s^\pm$ in lepton nasprotnega naboja v istem pljusku, pa zagotavljajo večjo čistost vzorca in s tem manjšo sistematično napako meritve.

8.2   Nastanek in razpad mezonov B_s^0 na trkalniku LEP

Anihilacija elektrona in pozitrona lahko poteka preko izmenjave fotona ali šibkega bozona. Feynmanova diagrama obeh procesov sta prikazana na sliki 8.1.

$$e^+ \quad \diagdown \qquad \diagup \ \overline{f} \quad e^+ \qquad\qquad \diagup\ \overline{f}$$

$$e^- \qquad Z^0 \qquad f \quad e^- \qquad \gamma \qquad f$$

a)   **b)**

Slika 8.1: Feynmanov diagram anihilacije elektrona in pozitrona preko izmenjave a) šibkega bozona ali b) fotona.

Anihilacijski sipalni presek pri težiščni energiji $\sqrt{s}$ je [7]

$$
\begin{aligned}
\sigma(\mathrm{e^+e^-} \to \mathrm{f\bar{f}}) \;=\; & N_f^c f_{QCD} \left[k_f^v \frac{4\pi\alpha^2}{3s} Q_f^2 + \right.\\
& + k_f^v \frac{G_F \alpha}{3\sqrt{2}} Q_f v_e v_f \frac{M_Z^2(M_Z^2 - s)}{(s - M_Z^2)^2 + s^2 \frac{\Gamma_Z^2}{M_Z^2}} + \\
& \left. + \frac{G_F^2}{96\pi}(v_e^2 + a_e^2)(k_f^v v_f^2 + k_f^a a_f^2) \frac{M_Z^4 s}{(s - M_Z^2)^2 + s^2 \frac{\Gamma_Z^2}{M_Z^2}} \right].
\end{aligned}
\tag{8.1}
$$

Q_f označuje naboj nastalega fermiona, izražen v enotah e_0, N_c^f pa število barv (3 za kvarke in 1 za leptone). α je konstanta

fine strukture in G_F Fermijeva konstanta, najnatančneje določena iz meritev življenjskega časa mionov [5]. Vektorsko in aksialno sklopitveno konstanto bozona Z^0 s fermioni izrazimo kot

$$v_f = 2T_{3f} - 4Q_f \sin^2 \theta_w$$
$$a_f = 2T_{3f} , \tag{8.2}$$

kjer T_{3f} predstavlja tretjo komponento šibkega izospina (+1/2 za nevtrine ter kvarke u, c, t in -1/2 za masivne leptone ter kvarke d, s, b). M_Z in Γ_Z sta masa ter širina bozona Z^0, θ_w pa Weinbergov kot. Kinematični faktorji $k_f^{v,a}$ so posledica končne mase nastalih fermionov:

$$k_f^v = \beta \frac{3 - \beta^2}{2}$$
$$k_f^a = \beta^3$$
$$\beta = \sqrt{1 - \frac{4m_f^2}{s}} . \tag{8.3}$$

Pri izračunu sipalnega preseka (8.1) je treba poleg diagramov na sliki 8.1 upoštevati še procese višjih redov. Možnost izsevanja gluonov v primeru hadronskih razpadov Z^0 je upoštevana s faktorjem

$$f_{QCD} = \left\{ \begin{matrix} 1; \ \text{leptoni} \\ 1 + \frac{\alpha_s(M_Z^2)}{\pi}; \ \text{kvarki} \end{matrix} \right\} . \tag{8.4}$$

Izmerjena razpadna širina bozona Z^0 in delež razpadov v pare $b\overline{b}$ znašata [6]

$$\Gamma(Z^0) = (2496.3 \pm 3.2) \ \text{MeV}$$
$$\Gamma(Z^0 \to q\overline{q}) = (1740.7 \pm 5.9) \ \text{MeV}$$
$$R_b \equiv \frac{\Gamma(Z^0 \to b\overline{b})}{\Gamma(Z^0 \to q\overline{q})} = 0.2219 \pm 0.0017 . \tag{8.5}$$

Primarni kvarki, nastali ob razpadu šibkega bozona, se s kvarki, nastalimi v procesu hadronizacije [12] [10] [11], združijo v opazljive hadrone. Hadroni, ki nastanejo v procesu hadronizacije, so lahko stabilni, ali pa nadalje razpadajo v lažje hadrone ter leptone. Razpad mezona B$_s^0$ je v osnovnem redu na partonskem nivoju prikazan na sliki 8.2.
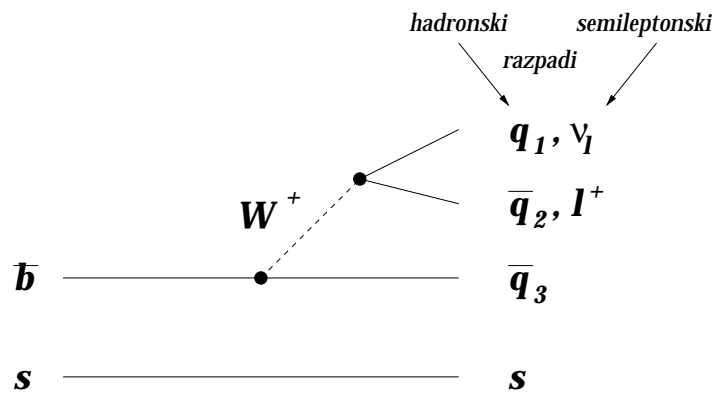
$$q_1 = u,\, c$$
$$\overline{q}_2 = \overline{d},\, \overline{s}$$
$$l^+ = e^+,\, \mu^+,\, \tau^+$$
$$\overline{q}_3 = \overline{c},\, \overline{u}$$

Slika 8.2: Feynmanov diagram razpada mezona B$_s^0$.

Razpad je lahko hadronski, če se nabiti šibki bozon W$^+$ sklaplja s kvarkoma, ali semileptonski, če W$^+$ razpade v lepton in nevtrino. Osnovni približek za razpadno širino mezona dobimo, če zanemarimo vpliv kvarka, ki spremlja težki kvark v hadronu. V tem primeru je lahki kvark zgolj opazovalec razpada in tak približek imenujemo spektatorski model. V tem modelu je razpadna širina

za hadronski razpad kateregakoli mezona B

$$\Gamma(b \rightarrow \overline{c}q_1\overline{q}_2) = 3\frac{G_F^2}{192\pi^3}m_b^5|V_{cb}|^2|V_{q_1q_2}|^2I(\frac{m_c}{m_b}, x_2, x_1) \ .$$

(8.6)

$\Gamma(b \rightarrow \overline{c}q_1\overline{q}_2)$ je sorazmerna peti potenci mase kvarka b. $V_{q_iq_j}$ so elementi matrike Cabbibo-Kobayashi-Maskava (CKM) [4], ki opisujejo moč sklopitve nabitih šibkih bozonov s kvarki. V izrazu (8.6) smo upoštevali le razpade, kjer se kvark b sklaplja s kvarkom c. Kot je razvidno iz slike 8.2 so možni tudi prehodi b→u. Slednji zaradi majhne vrednosti razmerja $|V_{ub}/V_{cb}| = 0.08 \pm 0.02$ [5] prispevajo zanemarljiv delež k celotni razpadni širini mezona B. S funkcijo $I(x_3, x_2, x_1)$ [14] upoštevamo končne mase nastalih kvarkov. V limiti $x_i = m_i/m_b \rightarrow 0$ je vrednost funkcije enaka 1.

Celotna razpadna širina delca je vsota parcialnih razpadnih širin. Ob približku $V_{cs} \approx V_{ud} \approx 1$ dobimo s Spekatorskim modelom naslednji izraz za celotno razpadno širino mezona B:

$$\frac{1}{\tau_B^{spec}} \ = \ \Gamma_B^{spec} \ \approx \ \frac{G_f^2}{192\pi^3}2.9m_b^5|V_{cb}|^2 \ .$$

(8.7)

Številski faktor 2.9 sledi iz omejitev faznega prostora za posamezne razpade, opisanih s funkcijo $I(x_3, x_2, x_1)$, če za masi kvarkov c in b privzamemo vrednosti $m_c = 1.6$ GeV/c^2 in $m_b = 5$ GeV/c^2 [5].

Proces na sliki 8.2, ki opisuje spektatorski razpad mezona B$_s^0$, ni edini mehanizem odgovoren za razpad. K razpadni širini prispevajo tudi drugi procesi, katerih prispevek je med drugim odvisen od lahkega kvarka, ki sestavlja mezon. Ti procesi povzročijo razlike med razpadnimi časi različnih vrst mezonov B. Skicirani so na sliki 8.3.

Razpadi z izmenjavo nabitega šibkega bozona (slika 8.3 a)) so možni le pri nevtralnih, razpadi z anihilacijo kvarkov (slika 8.3 c)) pa le pri nabitih mezonih B. Verjetnost za take razpade je znižana
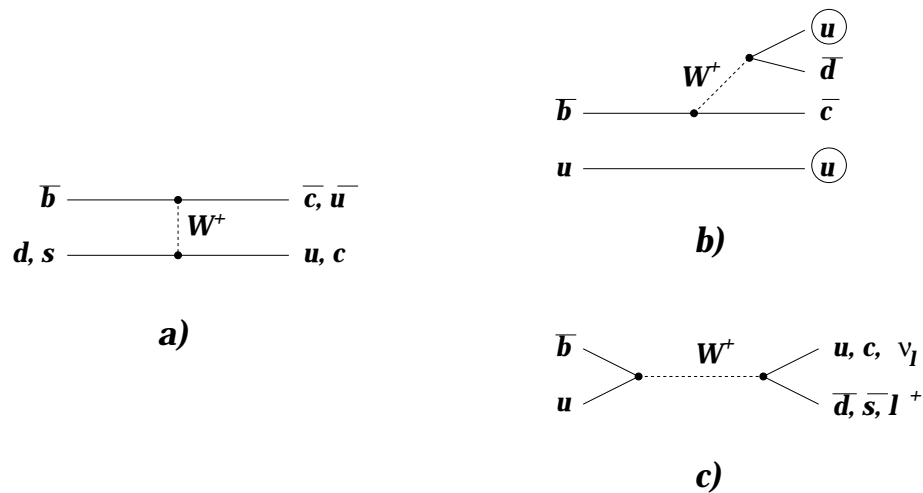
Slika 8.3: a) Razpad z izmenjavo šibkega bozona W$^\pm$. b) Razpad nabitih mezonov z dvema identičnima u kvarkoma v končnem stanju. c) Razpad preko anihilacije kvarkov.

glede na verjetnost za spektatorski razpad zaradi sučnosti nastalih kvarkov in zaradi zahteve po prekrivanju valovnih funkcij začetnih kvarkov [15]. Popravki k razpadni širini, ki izvirajo iz omenjenih procesov, so zato majhni.

Pri razpadih nabitih mezonov B se v končnem stanju lahko pojavita dva identična kvarka u (slika 8.3 b)). V tem primeru mora biti valovna funkcija končnega stanja antisimetrizirana glede na njuno zamenjavo. Popravek k spektatorski razpadni širini nabitih mezonov B, ki izvira iz takega procesa, je negativen [15]. Zato je življenjski čas mezonov $B^\pm$ nekoliko daljši kot razpadni čas nevtralnih mezonov B.

Podrobnejši račun prispevkov k razpadnim širinam različnih mezonov B, ki so posledica zgoraj opisanih procesov, nam da nasled-

nje pričakovane vrednosti razmerij življenjskih časov [17]:

$$
\begin{aligned}
\frac{\tau_{B^+}}{\tau_{B_d}} &\approx 1 + 0.05\left(\frac{f_B}{200 MeV}\right)^2 \\
\overline{\tau}_{B_d} &\approx \overline{\tau}_{B_s} .
\end{aligned}
\tag{8.8}
$$

Oznaki $\overline{\tau}_{B_s}$ in $\overline{\tau}_{B_d}$ označujeta povprečni vrednosti življenskih časov dveh masnih lastnih stanj v sistemu nevtralnih mezonov B, f_B pa razpadno konstanto mezona B.

8.3 Analiza podatkov

8.3.1 Razpadni kanal $\phi - \ell$

Med razpadi $Z^0 \rightarrow q\overline{q}$, zabeleženimi s spektrometrom Delphi v letih 1993 in 1994, smo izbrali dogodke, ki vsebujejo mezon ϕ in lepton v istem hadronskem pljusku. Hadronski razpadi Z^0 se od leptonskih ločijo predvsem po številu nabitih sledi v končnem stanju. Hadronske dogodke, ki se izbirajo že ob zapisu zabeleženih podatkov na magnetne trakove, je moč izbrati z izkoristkom nad 95% [27].

Pri izbiri vzorca $\phi\ell$ smo upoštevali elektrone in mione, identificirane s spektrometrom Delphi [20] [24]. Izbira leptonov temelji na zahtevi po visoki transverzalni gibalni količini delca glede na os hadronskega pljuska. Transverzalna gibalna količina leptona p_t, ki nastane v semileptonskem razpadu hadrona, je namreč odvisna od mase razpadlega delca. Izbira leptonov z visoko p_t omogoča obogatitev izbranega vzorca s semileptonskimi razpadi mezonov B. Simulirane porazdelitve transverzalnih gibalnih količin leptonov, nastalih v različnih procesih, so prikazane na sliki 8.4 a). Leptoni, ki izvirajo iz neposrednih semileptonskih razpadov mezonov B (b→ ℓ), imajo višjo povprečno p_t, kot leptoni iz kaskadnih raz-

padov (b → c → ℓ), kjer kvark b najprej razpade v kvark c, ta pa je vir leptonov. Še nižje transverzalne gibalne količine imajo leptoni iz neposrednih razpadov kvarkov c (c → ℓ), nastalih pri procesu Z^0 → c$\bar{c}$. Ozadje vključuje napačno identificirane leptone ter leptone iz razpadov lažjih hadronov. Prikazane porazdelitve vključujejo zahtevo, da je celotna gibalna količina leptonov, prikazana na sliki 8.4 b), višja kot 3 GeV/c.
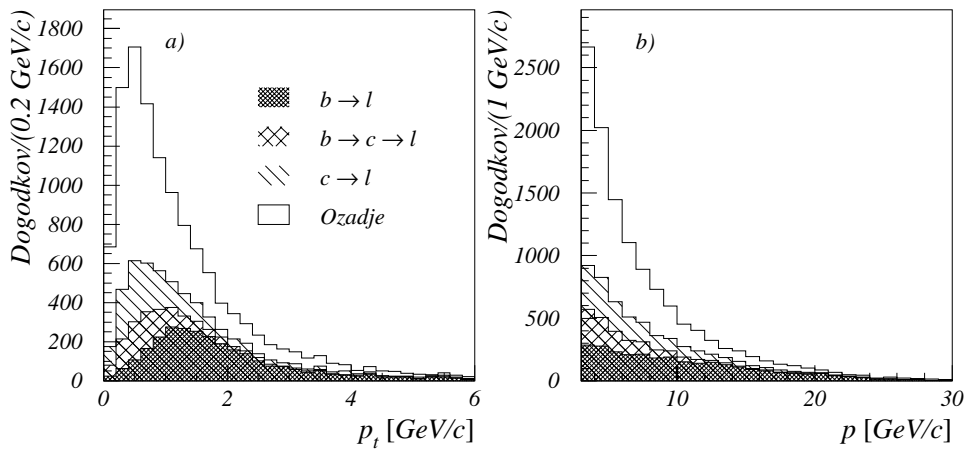
Slika 8.4: a) Rekonstruirana transverzalna gibalna količina leptonov glede na smer hadronskega pljuska. Prikazane so porazdelitve za različne vire leptonov na simuliranem vzorcu hadronskih razpadov Z^0. Porazdelitve vključujejo zahtevo, da je celotna gibalna količina delca višja kot 3 GeV/c. b) Enako za celotno gibalno količino leptonov.

Mezone ϕ smo rekonstruirali v razpadnem kanalu ϕ → K^+K^-, z razmejitvenim razmerjem (49.1 ± 0.9) % [5]. Izbira kaonov je temeljila na izmerjeni gibalni količini sledi ter na izračunani gibalni količini mezona ϕ in invariantni masi sistema $K^+K^-\ell$. Poleg kinematičnih rezov smo uporabili detektorje obročev Čerenkova, vgrajene v spektrometer Delphi [20]. Meritev kota Čerenkova skupaj z meritvijo specifične ionizacije sledi omogoča ločevanje pionov in kaonov, s tem pa znižanje kombinatoričnega ozadja v porazdelitvi invariantne mase parov K^+K^-.

Porazdelitev invariantne mase parov K^+K^- za izbrane dogodke je prikazana na sliki 8.5. Vrh porazdelitve je pri $M_\phi = (1.019 \pm 0.001)$ GeV/c^2, širina pri polovični višini pa je $\Gamma = (11.0 \pm 0.5)$ MeV. V intervalu 1.008 GeV/c^2 $< M(K^+K^-) <$ 1.030 GeV/c^2 je 433 ± 62 ϕ mezonov. M_ϕ se ujema z nominalno maso mezona ϕ, ki znaša (1019.413 ± 0.008) MeV/c^2 [5].
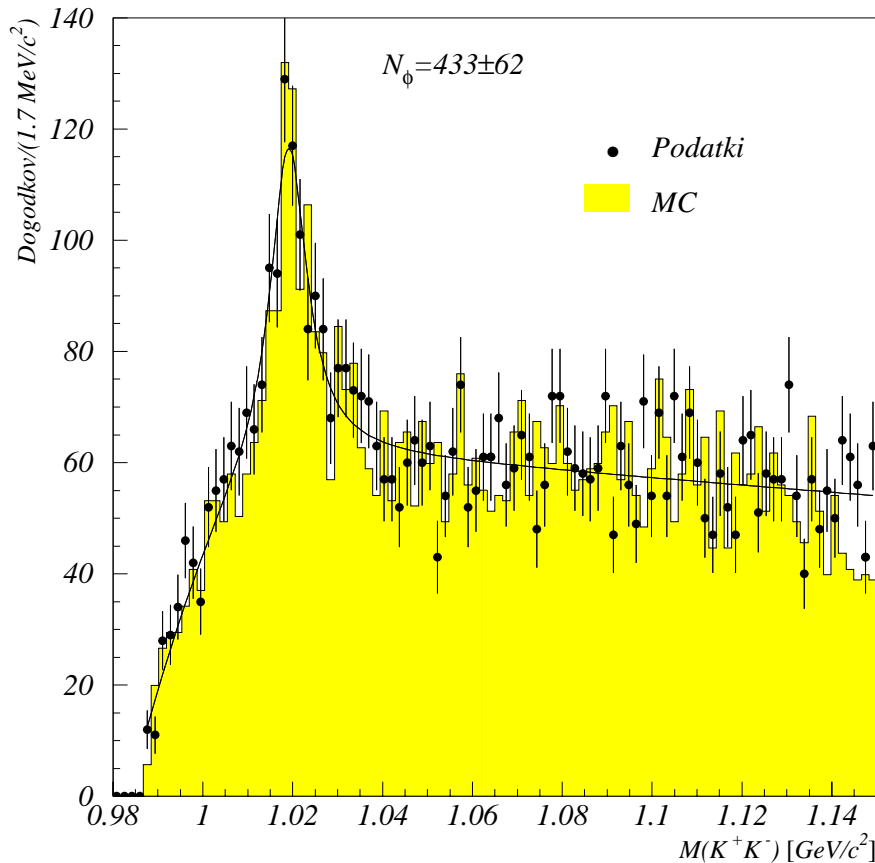
Slika 8.5: Porazdelitev invariantne mase izbranih parov K^+K^-. Na sliki je za primerjavo prikazana tudi enaka porazdelitev za simulirane hadronske razpade Z^0.

Deleže različnih procesov, ki prispevajo h končnemu stanju $\phi\ell$, smo izračunali s pomočjo simuliranih razpadov $Z^0 \to q\bar{q}$, ki smo jih izbrali z enakimi rezi kot podatke. Delež mezonov B_s^0

med vsemi razpadi mezonov B, ki prispevajo k rekonstruiranemu končnemu stanju, znaša 0.50 ± 0.07.

Razpadni čas mezona v njegovem lastnem sistemu je zvezan z razpadno razdaljo L in gibalno količino p_{B_s}:

$$t = \frac{L \, M_{B_s}}{p_{B_s}} \, . \qquad (8.9)$$

$M_{B_s} = (5375 \pm 6)$ MeV/c^2 je masa mezona B_s^0 [5].

Razpadno razdaljo mezona smo izmerili s prilagajanjem obeh kaonskih in leptonske sledi v izbranih dogodkih v skupno razpadno vozlišče. Gibalno količino smo določili iz deleža p_{B_s}, ki jo prevzame sistem $\phi\ell$, na simuliranih semileptonskih razpadih mezona B_s^0.

Za vsak dogodek v intervalu invariantne mase K$^+$K$^-$ med 1.008 in 1.030 GeV/c^2 smo izračunali razpadni čas po enačbi (8.9). Z metodo maksimalne zanesljivosti smo na tako izračunane razpadne čase prilagajali verjetnostno porazdelitev, ki je opisovala semileptonske razpade mezonov B_s^0 in prispevke procesov, ki predstavljajo ozadje. Porazdelitev razpadnih časov je prikazana na sliki 8.6.

Rezultat prilagajanja je povprečni življenjski čas mezonov B_s^0. Ob upoštevanju sistematičnih napak, ki so podrobneje opisane v tabeli 4.2, je izmerjeni življenjski čas na izbranem vzorcu dogodkov $\phi\ell$

$$\tau_{B_s} = \left[1.75 \pm 0.20(\text{stat.}) \begin{array}{c} +0.15 \\ -0.11 \end{array} (\text{syst.}) \right] \text{ps} \, .$$
$$(8.10)$$

8.3.2 Razpadni kanal $D_s^\pm - \ell^\mp$

Iz vzorca hadronskih razpadov Z^0, zabeleženih v letih 1992, 1993 in 1994, smo izbrali dogodke ki vsebujejo mezon $D_s^\pm$ skupaj z leptonom nasprotnega naboja v istem hadronskem pljusku. Način
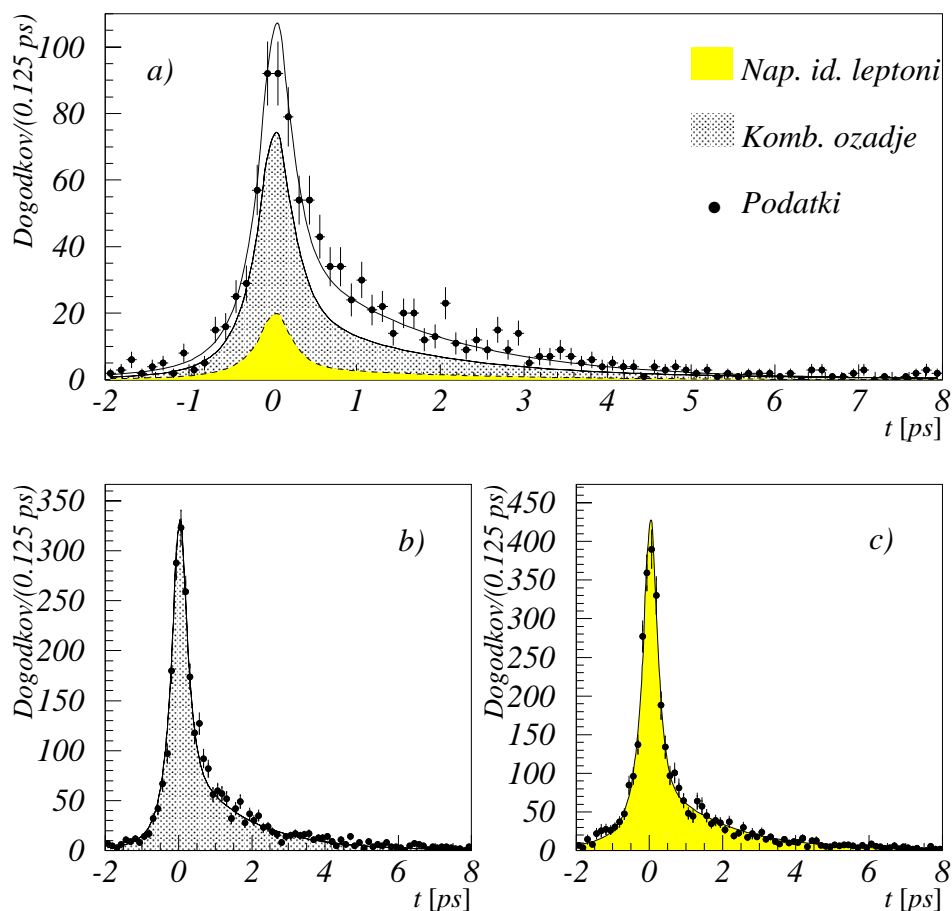
Slika 8.6: a) Porazdelitev razpadnih časov, v lastnem sistemu mezona B_s^0 , za dogodke v izbranem območju invariantnih mas K^+K^-. Osenčena območja predstavljajo prispevek kombinatoričnega ozadja ter ozadja, ki izvira iz napačno identificiranih leptonov in leptonov iz razpadov lahkih hadronov. Krivulja prikazuje rezultat prilagajanja z metodo maksimalne zanesljivosti. b) Enaka porazdelitev za dogodke v stranskem intervalu invariantnih mas K^+K^-, ki predstavljajo kombinatorično ozadje. c) Porazdelitev razpadnih časov za dogodke z napačno identificiranimi leptoni oziroma z leptoni iz razpadov lahkih hadronov. Porazdelitev je bila rekonstruirana na simuliranem vzorcu razpadov B_s^0.

izbire leptonov je bil enak kot v predhodni analizi, izbrani rezi pa nekoliko ostrejši. Zaradi tega je izbrani vzorec vseboval nižje deleže ozadja kot vzorec dogodkov $\phi\ell$.

Mezone $D_s^{\pm}$ smo rekonstruirali preko dveh razpadnih kanalov: $D_s^{\pm} \rightarrow \phi\pi^{\pm}$ in $D_s^{\pm} \rightarrow \overset{(-)}{K}{}^{*0}K^{\pm}$. Razvejitveni razmerji obeh razpadnih načinov sta podobni in znašata $(3.5 \pm 0.4)\%$ za prvi in $(3.3 \pm 0.5)\%$ za drugi kanal [5]. Medtem, ko smo mezone ϕ iskali preko enakega razpadnega kanala kot v prejšnji analizi, smo pri mezonih K^{*0} izkoristili razpad v $K^-\pi^+$.

Kinematični izbirni kriteriji so vsebovali gibalne količine obeh nabitih kaonov in nabitega piona v končnem stanju, gibalno količino mezona ϕ ali K^{*0}, invariantno maso para delcev, ki sta tvorila ϕ ali K^{*0}, energijo mezona $D_s^{\pm}$ in pa gibalno količino ter invariantno maso sistema $D_s^{\pm}\ell^{\mp}$. Ker gre pri obravnavanih procesih za razpad psevdoskalarnega mezona $D_s^{\pm}$ v vektorski mezon ϕ ali K^{*0} ter psevdoskalarni mezon $\pi^{\pm}$ ali $K^{\pm}$, smo pri izbiri dogodkov upoštevali tudi ustrezno kotno porazdelitev nastalih delcev. Poleg kinematičnih zahtev smo tako kot v prejšnji analizi uporabili identifikacijo delcev s pomočjo detektorjev Čerenkova in meritve specifične ionizacije.

Invariantno maso obeh kaonov in piona za izbrane dogodke kaže slika 8.7. V porazdelitvi je izrazit vrh pri masi $M_{D_s} = (1.968 \pm 0.002)$ GeV/c^2. Širina signala je $\sigma_{D_s} = (13.5 \pm 2.2)$ MeV. M_{D_s} se ujema z nominalno maso mezona $D_s^{\pm}$ (1968.5 ± 0.7) MeV/c^2. V območju $\pm 2\sigma_{D_s}$ je 81 ± 13 mezonov $D_s^{\pm}$.

Delež mezonov B_s^0 med vsemi mezoni B, ki prispevajo h končnemu stanju $D_s^{\pm}\ell^{\mp}$, je na simuliranih dogodkih, analiziranih na enak način kot podatki, znašal 0.843 ± 0.034.

Za dogodke z invariantno maso $M(KK\pi)$ med 1.941 in 1.995 GeV/c^2
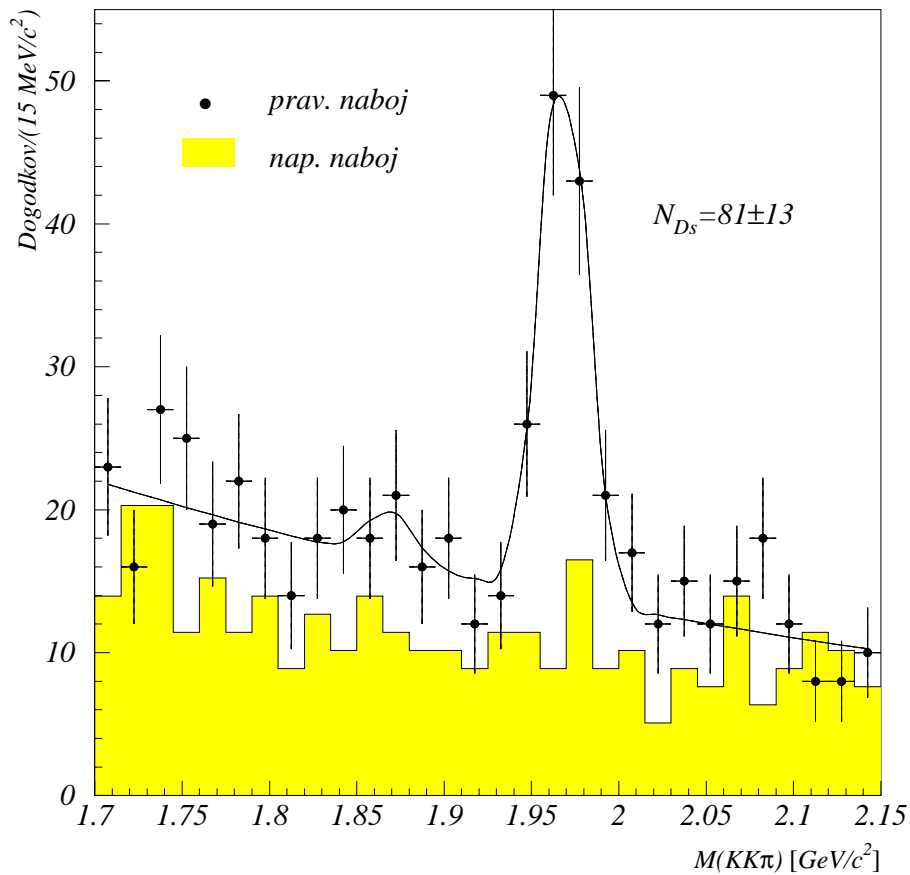
Slika 8.7: Porazdelitev invariantne mase delcev $KK\pi$ za izbrane do-
godke $D_s^\pm \rightarrow \phi\pi^\pm$, $\overset{(-)}{K}{}^{*0}K^\pm$ z $\ell^\mp$ v istem hadronskem pljusku. Senčena
porazdelitev kaže invariantno maso dogodkov, kjer je izbrani lepton
enakega naboja kot rekonstruirani mezon $D_s^\pm$.

smo izračunali razpadni čas po enačbi (8.9). Razdaljo med inter-
akcijsko točko e^+e^- ter razpadno točko mezona B_s^0 smo dobili s
prilagajanjem rekonstruirane sledi $D_s^\pm$ in leptonske sledi v skupno
razpadno vozlišče. Gibalno količino mezona B_s^0 smo izračunali iz
energije sistema $D_s^\pm\ell^\mp$, kateri smo dodali popravke izvrednotene
na simuliranih razpadih.

Kot pri analizi s končnim stanjem $\phi\ell$ smo na razpadne čase

izbranih dogodkov prilagajali verjetnostno porazdelitev z metodo maksimalne zanesljivosti. Prilagajana funkcija je zopet vsebovala člene za opis signala ter člene, ki so popisovali porazdelitve dogodkov ozadja.

Dobljene porazdelitve so skupaj z rezultati prilagajanja prikazane na sliki 8.8. Ob upoštevanju sistematičnih napak, opisanih v tabeli 5.3, je končni rezultat prilagajanja

$$\tau_{B_s} = \left[1.47 \ \pm \ 0.27(\text{stat.}) \ \pm \ 0.11(\text{syst.}) \right] \text{ps} \ .$$
(8.11)

8.4 Rezultati in zaključki

Meritvi življenjskega časa mezonov B_s^0 , izvedeni na dveh različnih vzorcih semileptonskih razpadov mezonov B, lahko združimo v enoten rezultat. S primerjavo izbranih dogodkov smo ugotovili obseg statističnega prekrivanja vzorcev. Analiza virov sistematičnih napak je pokazala, da je majhen del sistematične napake skupen obema meritvama. Korelacije obeh meritev so majhne in ne vplivajo na povprečen rezultat obeh meritev. Pri izračunu povprečja smo kot utež posamezne meritve upoštevali relativne napake, da se izognemo sistematičnemu premiku kombiniranega rezultata [36]. Izmerjeni povprečni življenjski čas mezonov B_s^0 je

$$\tau_{B_s} = (1.66 \ \pm \ 0.19) \text{ ps} \ .$$
(8.12)

Slika 8.9 uvršča obe izvedeni meritvi v povzetek svetovnih meritev življenjskega časa τ_{B_s}. Meritev življenjskega časa na vzorcu dogodkov z mezonom ϕ in leptonom v istem hadronskem pljusku je ena najnatančnejsih posameznih meritev τ_{B_s}.
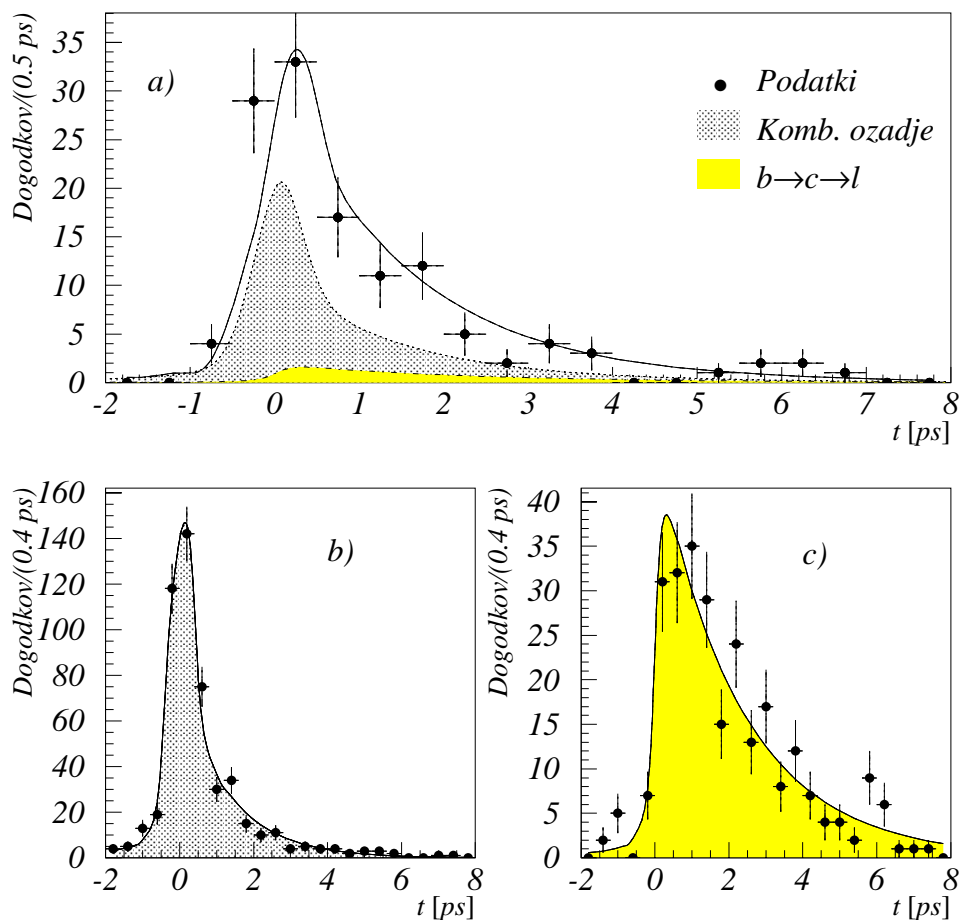
Slika 8.8: a) Razpadni čas za dogodke z invariantno maso $M(\mathrm{KK}\pi)$ v območju mase mezona $\mathrm{D}_s^{\pm}$. Senčene porazdelitve kažejo prispevka dveh najpomembnejših virov ozadja: kombinatoričnega ter ozadja z dogodki, ki vsebujejo kaskadne razpade mezonov B. Polna krivulja je rezultat prilagajanja. b) Porazdelitev razpadnih časov za dogodke v stranskem intervalu mase $M(\mathrm{KK}\pi)$ ter za dogodke z rekonstruiranim mezonom $\mathrm{D}_s^{\pm}$ v pljusku z leptonom enakega naboja. Ti dogodki predstavljajo kombinatorično ozadje. c) Porazdelitev razpadnih časov za dogodke s kaskadnimi razpadi mezonov B. Razpadni časi so bili izmerjeni na simuliranih razpadih mezonov B.
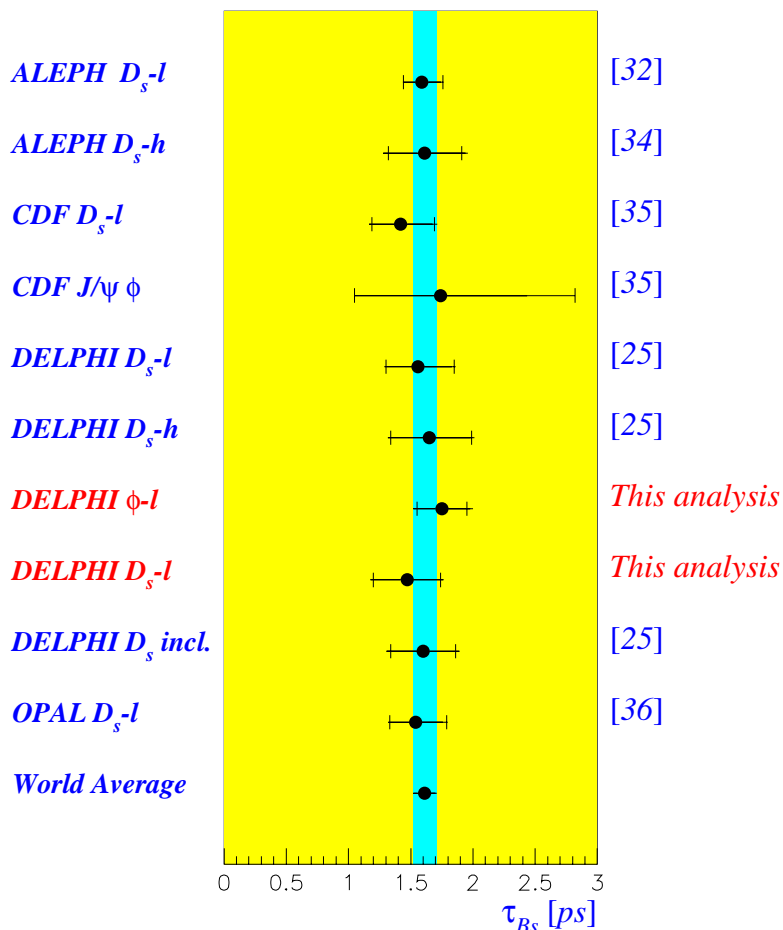
Slika 8.9: Povzetek meritev življenjskega časa τ_{B_s}. Ob desni strani so označene reference izvedenih meritev. Prvi del napak, omejen z navpičnimi črtami, označuje delež statistične napake v kvadratični vsoti sistematične in statistične napake. Svetovno povprečje je povzeto po [39].

Žal dosežena natančnost meritve ne zadošča za preverjanje napovedi razmerja τ_{B_s}/τ_{B_d} ali τ_{B^+}/τ_{B_s}, podanima z (8.8). Če uporabimo svetovno povprečje življenjskih časov τ_{B_s} in τ_{B_d} [39], dobimo

ob zanemaritvi možnih korelacij

$$\frac{\tau_{B_s}}{\tau_{B_d}} = 1.03 \pm 0.07 \,, \qquad\qquad (8.13)$$

vrednost, ki je popolnoma skladna z 1.

Podobno dobimo z uporabo svetovnih povprečij

$$\frac{\tau_{B^+}}{\tau_{B_s}} = 1.01 \pm 0.07 \,. \qquad\qquad (8.14)$$

Zgornja vrednost tega razmerja ni daleč od napovedi (8.8): pri razpadni konstanti f_B=200 MeV [19] [18] bi za razmerje pričakovali vrednost 1.05.

Življenjski čas τ_{B_s} bomo v bodoče lahko uporabili pri morebitnih meritvah razpadnih širin mezonov B_s^0. Posebej zanimiv je vzorec razpadov s končnim stanjem $\phi\ell$. Zaradi zadovoljive statistične moči ga bo mogoče uporabiti pri meritvah frekvence oscilacij v sistemu mezonov B_s^0. Zabeleženo število razpadov B_s^0 zaenkrat omogoča zgolj določanje spodnje meje frekvence oscilacij. Upati je, da se bo ob uporabi omenjenega vzorca dalo dodatno omejiti območje možnih frekvenc, ter s tem doseči globji vpogled v fiziko mezonov B.

Part VI

Appendices

Chapter 9

9.1 Appendix A

- D^{**} production in B semileptonic decays

The relative fraction of orbitally excited charm mesons in the B meson semileptonic decays can be calculated from the following measured exclusive branching ratios [5][36]:

$$
\begin{aligned}
B_0^a &= Br(\mathrm{B}_d^0 \to \mathrm{D}^- \ell^+ \nu_\ell) &=& \ (1.9 \pm 0.5) \times 10^{-2} \\
B_0^b &= Br(\mathrm{B}_d^0 \to \mathrm{D}^{*-} \ell^+ \nu_\ell) &=& \ (4.4 \pm 0.4) \times 10^{-2} \\
B_+^a &= Br(\mathrm{B}^+ \to \overline{\mathrm{D}}^0 \ell^+ \nu_\ell) &=& \ (1.6 \pm 0.7) \times 10^{-2} \\
B_+^b &= Br(\mathrm{B}^+ \to \overline{\mathrm{D}}^{*0} \ell^+ \nu_\ell) &=& \ (4.7 \pm 1.1) \times 10^{-2} \ .
\end{aligned}
\tag{9.1}
$$

The decays into the D^{**} represent the remainder of the inclusive semileptonic branching fractions [36]

$$
\begin{aligned}
B_0^{sl} &= Br(\mathrm{B}_d^0 \to \ell^+ \nu_\ell X) &=& \ (9.5 \pm 1.6) \times 10^{-2} \\
B_+^{sl} &= \frac{\tau_{B^+}}{\tau_{B_d}} Br(\mathrm{B}_d^0 \to \ell^+ \nu_\ell X) &=& \ (9.9 \pm 1.7) \times 10^{-2} \ .
\end{aligned}
\tag{9.2}
$$

Hence, one can expect the fraction of the D^{**} in the B_d^0 and

161

$B^\pm$ meson decays to be

$$f_0^{**} = 1 - \frac{B_0^a + B_0^b}{B_0^{sl}} = 0.34 \pm 0.13$$

$$f_+^{**} = 1 - \frac{B_+^a + B_+^b}{B_+^{sl}} = 0.36 \pm 0.17 , \qquad (9.3)$$

respectively. The average fraction for the non-strange B mesons

$$f^{**} = 0.35 \pm 0.10 \qquad (9.4)$$

can be used as an estimate of the D_s^{**} production in the B_s^0 decays.

- D_s production in the D_s^{**} decays

Each orbitally excited D meson appears as four states with the spin and parity quantum numbers $J^P = 0^+,\ 1^+,\ 1^+,\ 2^+$. Due to the isospin conservation the D_s^{**} cannot decay into the D_s meson and a single pion. Hence the kinematicaly favoured decay which produces the strange D meson in the final state is $D_s^{**} \rightarrow D_s \pi\pi$, with isospin of the pions system equal to 0. In the case of non-strange D meson in the final state the isospin allowed decay is $D_s^{**} \rightarrow D_{ns}K$.

In order to satisfy the Bose-Einstein statistics, the angular momentum of the $\pi\pi$ system must be even, if the isospin equals to 0. For the $D_s^{**} \rightarrow D_s \pi\pi$ decay the following conservation laws must be obeyed:

$$P_{D_s^{**}} = +1 = (-1)_{D_s}\ (-1)^{\ell_{\pi\pi}}\ (-1)^\ell$$

$$\vec{J}_{D_s^{**}} = (\vec{0})_{D_s} + (\vec{\ell})_{\pi\pi} + \vec{\ell} . \qquad (9.5)$$

The subscripts indicate particles to which the corresponding quantum number belongs to, and $\vec{\ell}$ is the relative angular momentum between the D_s meson and the $\pi\pi$ system. It is easy to conclude from the above equations that the only decay expected to

contribute to the strange D meson in the final state is the decay of the 1^+ state proceeding through an $\ell = 1$ angular momentum wave.

On a similar ground one can conclude that the decays of the D_s^{**} into the non-strange D mesons are possible through the $\ell = 0$ wave for the 0^+ and 1^+ state, while the dominant decay of the 2^+ state proceeds through the $\ell = 2$ wave.

Up to now the only experimentally observed 1^+ D_s^{**} state is reconstructed through the decays into the non-strange D meson [43][34]. It is therefore reasonable to assume that this decay is the dominant one. The upper limit for the D_s production from the orbitally excited strange D mesons can then be obtained by assuming the other 1^+ state to decay dominantly into the $D_s\pi\pi$ final state. By assigning the number of different energy levels for the individual J^P state simply by spin counting, i.e. as $2J + 1$, the fraction of the D_s in the D_s^{**} decays is

$$\frac{N_{D_s}}{N_{D_s^{**}}} = \frac{N(J = 1)}{N(J = 0) + 2N(J = 1) + N(J = 2)} = \frac{1}{4}. \tag{9.6}$$

- D_s production in the D_{ns}^{**} decays

The isospin conservation allows the decays of the orbitally excited non-strange D mesons into the $D_s^{(*)}K$ and $D_{ns}^{(*)}\pi$ final state. From the parity and angular momentum consideration one can draw the following conclusions:

0^+ state can decay into the strange and non-strange D meson ground state through the $\ell = 0$ wave.

1^+ state exhibit a similar property apart from the fact that the final state charm mesons are now D^*. However the mass and

the width of the experimentally observed D_{ns}^{**} state with $J^P = 1^+$ is 2423 MeV/c^2 and 18 MeV respectively [5]. Since the sum of the masses of the D_s^* and K meson is around 2600 MeV/c^2, we conclude that the production of the strange D mesons from this state is negligible. The assumption was thus made that only one of the 1^+ states contributes to the D_s in the final state.

2^+ state decay into the D_sK and $D_{ns}\pi$ is possible through the $\ell = 2$ wave. The measured mass and decay width of the 2^+ non-strange D meson state is approximately 2460 MeV/c^2 and 20 MeV [5]. The sum of the D_s and kaon masses is close to the value of the quoted D_{ns}^{**} mass and hence the decay of this state into the strange D meson was neglected.

Beside the above considerations one should note that the decays into the strange D mesons are suppressed also due to the additional $s\bar{s}$ pair required. The suppression factor can be inferred from the measured probabilities for the b$\rightarrow$ B$_s$ and b$\rightarrow$ B$_{u,d}$ fragmentation (see Table 4.1):

$$r_s = \frac{\mathrm{Prob}(s\bar{s})}{\mathrm{Prob}(u\bar{u})} = \frac{\mathrm{Prob}(s\bar{s})}{\mathrm{Prob}(d\bar{d})} = \frac{P_s}{P_{u,d}} \approx 0.25 . \qquad (9.7)$$

Finally we obtain for the fraction of the D_s mesons produced in the D_{ns}^{**} decays

$$\frac{N_{D_s}}{N_{D_{ns}^{**}}} = \frac{N(J = 0)}{N(J = 0) + 2N(J = 1) + N(J = 2)} \frac{r_s}{2 + r_s} +$$

$$+ \frac{N(J = 1)}{N(J = 0) + 2N(J = 1) + N(J = 2)} \frac{r_s}{2 + r_s} \approx (3 - 4) \times 10^{-2} , \qquad (9.8)$$

where the first term arises due to the contribution of the 0^+ state decays and the second due to the 1^+ state decays into the strange charmed mesons.

9.2 Appendix B

- Convolution of the exponential and the Gaussian distribution

$$
\mathcal{P}(t,\sigma_t,\tau) \;=\; \frac{1}{\sqrt{2\pi}\,\sigma_t\tau} \int_0^\infty e^{-\frac{(t-u)^2}{2\sigma_t^2}}\, e^{-\frac{u}{\tau}}\, du \;=
$$

$$
=\; \frac{1}{2\tau} e^{\frac{\sigma_t^2}{2\tau^2}-\frac{t}{\tau}} \left[1 + Erf\!\left(\frac{t}{\sqrt{2}\sigma_t} - \frac{\sigma_t}{\sqrt{2}\tau}\right)\right] \qquad (9.9)
$$

The $Erf(x)$ is the error function given by

$$
Erf(x) \;=\; \frac{2}{\sqrt{\pi}} \int_0^x e^{-z^2}\, dz \;. \qquad (9.10)
$$

- Normalisation of the convolution

Since the actual interval of the proper decay times used for the lifetime measurement is not infinite, the convolution $\mathcal{P}(t,\sigma_t,\tau)$ should be normalised in the finite interval between $-|t_1|$ and t_2:

$$
\frac{1}{A} \int_{-|t_1|}^{t_2} \mathcal{P}(t,\sigma_t,\tau)\, dt \;=\; 1\;. \qquad (9.11)
$$

The calculation of the normalisation factor A yields:

$$
\frac{1}{A} \;=\; \frac{1}{2}\left[Erf\!\left(\frac{|t_1|}{\sqrt{2}\sigma_t}\right) + Erf\!\left(\frac{t_2}{\sqrt{2}\sigma_t}\right)\right] +
$$
$$
+\; \frac{1}{2} e^{\frac{\sigma_t^2}{2\tau^2}} \left[e^{\frac{|t_1|}{\tau}} \left[1 - Erf\!\left(\frac{\sigma_t}{\sqrt{2}\tau} + \frac{|t_1|}{\sqrt{2}\sigma_t}\right)\right] -
$$
$$
-\; e^{-\frac{t_2}{\tau}} \left[1 - Erf\!\left(\frac{\sigma_t}{\sqrt{2}\tau} - \frac{t_2}{\sqrt{2}\sigma_t}\right)\right]\right]\;. \qquad (9.12)
$$

In the limit $|t_1|, t_2 \to \infty$ the normalisation factor approaches unity. The effect of the normalisation is non-negligible only at large lifetime τ. For example, the normalisation factor of the sum

$\mathcal{G}(t, \sigma_t) + \mathcal{E}(t, \sigma_t, \tau) \otimes \mathcal{G}(t, \sigma_t)$ for the interval of the decay times used in the described analysis and with the typical achieved resolution σ_t differs from unity by less than 2% for the lifetime range up to 2.5 ps.

9.3   Appendix C

In figure 9.1 the decay chain $D_s^\pm \rightarrow \phi \pi^\pm$; $\phi \rightarrow K^+ K^-$ is sketched in the rest frame of the ϕ vector meson. Since the $D_s^\pm$ and the $K^\pm$ are pseudo-scalar mesons, both successive decays proceed through the $\ell = 1$ wave. Using the Dirac notation, the state with the total angular momentum J and the z-component of the angular momentum M is represented by $|J\ M>$. The decomposition of the $D_s^\pm$ state into the ϕ meson spin state $|1\ M_\phi>$ and the relative orbital angular momentum between the ϕ and the π meson $|\ell\ M_\ell>$ is given by

$$|0\ 0> = \sqrt{\frac{1}{3}}|1\ 1>|1\ -1> -\sqrt{\frac{1}{3}}|1\ 0>|1\ 0> +\sqrt{\frac{1}{3}}|1\ -1>|1\ 1>.$$
(9.13)

The first ket vectors in the above products describe the ϕ spin state and the second the relative orbital angular momentum between the ϕ and the π. Factors $\sqrt{1/3}$ are the appropriate Clebsch-Gordan coefficients.

Since kaons are spinless, the ϕ meson's spin wave function in its rest frame equals to the angular part of the $K^+ K^-$ system wave function. The angular distribution may be described by the two sets of angles Ω_π and Ω_K, corresponding to the pion and the kaon direction with respect to some arbitrary z axis in the rest frame of the ϕ. The angular part of the wave function for the final state is
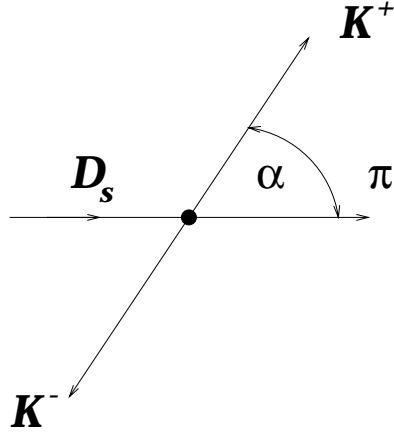
Figure 9.1: The $D_s^{\pm}$ decay into the ϕ and $\pi^{\pm}$ meson, followed by the decay $\phi \to K^+K^-$, viewed in the rest frame of the ϕ meson.

then written as

$$\psi \propto Y_1^1(\Omega_K)Y_1^{-1}(\Omega_\pi) - Y_1^0(\Omega_K)Y_1^0(\Omega_\pi) + Y_1^{-1}(\Omega_K)Y_1^1(\Omega_\pi) \tag{9.14}$$

in accordance with (9.13) and using the spherical harmonics $Y_J^M(\Omega)$. By squaring the dependence (9.14) one obtains the angular distribution of the decay products in the form

$$\frac{dN}{d\Omega_K d\Omega_\pi} \propto \left[\cos\theta_K \cos\theta_\pi + \sin\theta_K \sin\theta_\pi \cos(\phi_K - \phi_\pi)\right]^2. \tag{9.15}$$

By choosing the z axis in the direction of the pion θ_K becomes just the angle α of figure 9.1 and the distribution is

$$\frac{dN}{d\Omega} \propto \cos^2\alpha \tag{9.16}$$

Bibliography

[1] S.L. Glashow, *Partial Symmetries of Weak Interactions*, Nuc. Phys. **22** (1961) 579.

S. Weinberg, *A Model of Leptons*, Phys. Rev. Lett. **19** (1967) 1264.

A. Salam, *Weak and Electromagnetic Interactions*, Proceedings of the Nobel Symposium held 1968 at Lerum, Sweden, Stockholm (1968) 367.

[2] F.J. Hasert et al. (Gargamelle Coll.), *Observation of neutrino like interactions without muon or electron in the Gargamelle neutrino experiment*, Phys. Lett. **B46** (1973) 138.

F.J. Hasert et al. (Gargamelle Coll.), *Observation of neutrino like interactions without muon or electron in the Gargamelle neutrino experiment*, Nucl. Phys. **B 73** (1974) 1.

[3] UA1 Coll., *Experimental Observation of Lepton Pairs of Invariant Mass around 95 GeV/c^2 at the Cern SPS Collider*, Phys. Lett. **B122** (1983) 103.

UA2 Coll., *Observation of Single Isolated Electrons of High Transverse Momentum in Events with Missing Transverse Energy at the Cern $\overline{p} - p$ Collider*, Phys. Lett. **B122** (1983) 476.

UA1 Coll., *Experimental Observation of Isolated Large Transverse Energy Electrons with Associated Missing Energy at $\sqrt{s}$=540 GeV*, Phys. Lett. **B126** (1983) 398.

[4] N. Cabibbo, *Unitary Symmetry and Leptonic Decays*, Phys. Rev. Lett. **10** (1963) 531.

M. Kobayashi, T. Maskawa, *CP Violation in the Renormalizable Theory of Weak Interactions*, Prog. Theor. Phys. **49** (1973) 652.

[5] R.M. Barnett et al. (Particle Data Group), *Review of Particle Properties*, Phys. Rev. **D50** (1994) 1.

[6] Aleph Coll., Delphi Coll., L3 Coll., Opal Coll., *A Combination of Preliminary LEP Electroweak Measurements and Constraints on the Standard Model*, LEP Electroweak Working Group, CERN-PPE **95-172**, prepared from contributions of the LEP experiments to the 1995 International Europhysics Conference on High Energy Physics, 27th July-2nd August 1995, Brussels, Belgium and the 17th International Symposium on Lepton-Photon Interactions, 10th-15th August 1995, Beijing, China.

[7] J.H. Kühn, P.M. Zervas, *Heavy Flavours*, in Z *Physics at LEP 1, Vol. 1*, eds. G. Altarelli, R. Kleiss, C. Verzegnass, CERN **89-08** (Yellow Report) (1989) 267.

M. Consoli, W. Hollik, *Electroweak Radiative Corrections for* Z *Physics*, in same publication, 7.

F. Berends, Z *Line Shape*, in same publication, 89.

[8] A. Blondel, *Precision Tests of the Standard Electroweak Model at LEP*, in *High Energy Phenomenology*, Proceedings of the 42nd Scottish Universities Summer School in Physics, eds. K.J. Peach, L.L.J. Vick, P. Osborne, SUSSP Publications and Institute of Physics Publishing (1994) 417.

[9] O. Nachtmann, *Elementary Particle Physics*, Springer-Verlag (1990).

[10] B. Andersson, G. Gustafson, G. Ingelman, T. Sjöstrand, *Parton Fragmentation and String Dynamics*, Phys. Rep. **97** (1983) 31.

[11] R. D. Field, R.P. Feynman, *A Parametrization of the Properties of Quark Jets*, Nucl. Phys. **B136** (1978) 1, and references therein.

[12] F. Halzen, A.D. Martin, *Quarks and Leptons*, John Wiley & Sons (1984).

[13] C. Peterson, D. Schlatter, I. Schmitt, P.M. Zerwas, *Scaling Violations in Inclusive* e^+e^- *Annihilation Spectra*, Phys. Rev. **D27** (1983) 105.

[14] H.B. Thacker, J.J. Sakuari, Phys. Lett. **B36** (1971) 103.
M. Gourdin, X.Y. Pham, *Study of Electron Type Neutral Heavy Lepton in Electron Positron Reactions*, Nucl. Phys. **B164** (1981) 399.
J.L. Cortes, X.Y. Pham, A. Tounsi, *Mass Effects in Weak Decays of Heavy Particles*, Phys. Rev. **D25** (1982) 188.

[15] R. Rückl, *Weak Decays of Heavy Quark States*, Proceedings of Elementary Particles, Varrena (1984) 43.

[16] I.I. Bigi, *Models of Nonleptonic* B *Decays*, in B *Decays*, ed. S. Stone, World Scientific (1982) 102.

[17] I.I. Bigi, B. Blok, M. Shifman, N. Urlatsev, A. Vainshtein, *Nonleptonic Decays of Beauty Hadrons - From Phenomenology to Theory*, in B *Decays*, Revised 2nd Edition, ed. S. Stone, World Scientific (1994) 132.

[18] S. Aoki et al. (WA75 Coll.), *First Observation of the Muonic Decay* $D_s^+ \to \mu^+ \nu_\mu$, Prog. Theor. Phys. **89** (1993) 131.

[19] S. Narison, *Precise Determination of f_{P_s}/f_P and Measurement of the "Perturbative" Pole Mass from f_P*, Phys. Lett. **B322** (1994) 247.

[20] P. Aarnio et al. (Delphi Coll.), *The DELPHI detector at LEP*, Nucl. Instr. and Methods **A303** (1991) 233.
P. Abreu et al. (Delphi Coll.), *Performance of the DELPHI Detector*, Nucl. Instr. and Methods **A378** (1996) 57.

[21] Delphi Coll., *The DELPHI Microvertex Detector*, internal note, DELPHI **92-92** PHYS-203 (1992), paper submitted to the XXVI International Conference in High Energy Physics, Dallas, Texas, USA.
V. Chabaud et al., *The DELPHI Silicon Strip Microvertex Detector with Double Sided Readout*, Nucl. Instr. and Methods **A368** (1996) 314.

[22] A. Cattai et al., *Equalization of the Readout Channels of the HPC by Means of Radioactive Gas*, internal note, DELPHI **93-115** CAL-105 (1993).

[23] A. De Min et al., *Performance of the HPC Calorimeter in DELPHI*, CERN-PPE **95-04** (1995).

[24] M. Feindt, C. Kreuter, O. Podobrin, *ELEPHANT Reference Manual*, internal note, DELPHI **96-82** PROG-217 (1996).
K.D. Brand, I. Roncagliolo, F. Simonetto, *Electron Identification for Electro-weak* b, c *Physics*, internal note, DELPHI **96-23** PHYS-598 (1996).

[25] C. Fabjan, *Calorimetry in High Energy Physics*, in *Experimental Techniques in High Energy Physics*, ed. T. Ferbel, Addison-Wesley Publishing Co., (1987) 257.

[26] W. Adam et al., *Analysis Techniques for the DELPHI Ring Imaging Cherenkov Detector*, internal note, DELPHI **94-112** PHYS-429 (1994), paper submitted to Int. Conf. on High Energy Phys.

[27] P. Abreu et al. (Delphi Coll.), *Improved Measurements of Cross Sections and Asymmetries at the Z^0 resonance*, Nucl. Phys. **B418** (1994) 403.

[28] T. Sjöstrand, *The Lund Monte Carlo for Jet Fragmentation*, Comp. Phys. Comm. **27** (1982) 243.
T. Sjöstrand, *The Lund Monte Carlo for* e^+e^- *Jet Physics*, Comp. Phys. Comm. **28** (1983) 229.
T. Sjöstrand, M. Bengtsson, *The Lund Monte Carlo for Jet Fragmentation and* e^+e^- *Physics: Jetset Version 6.3: An Update*, Comp. Phys. Comm. **43** (1987) 367.

[29] Delphi Coll., *DELSIM Reference Manual*, internal note, DELPHI **87-97** PROG-100 (1987).

[30] Delphi Coll., *Summary of Delphi's current-best B&C-Physics Numbers*, internal note, DELPHI **95-139** PHYS-564 (1995), and references therein.

[31] P. Abreu et al. (Delphi Coll.), *Mean Lifetime of the* B_s^0 *Meson*, Zeit. Phys. **C71** (1996) 11., and references therein.

[32] P. Billoir, S. Qian, *Fast Vertex Fitting With a Local Parametrization of the Tracks*, Nucl. Instr. and Methods **A311** (1992) 139.

[33] G.V. Borisov, *Lifetime Tag of Events* $Z \to b\bar{b}$ *With the Delphi Detector*, internal note, DELPHI **94-125** PROG-208 (1994).

[34] S. Komamiya, b- *and* c-*Physics*, Proceedings of the Int. EPS HEP Conference, Brussels, July 1995, World Scientific (1995) 727.

[35] E. Golowich, A. Le Yaouanc, L. Oliver, O. Pene, J.C. Raynal, *Background for Tagging* B(s) *Events at LEP*, Zeit. Phys. **C48** (1990) 89.

A. Stocchi, *Mesures de la production et de la durée de vie du méson* B_s^0 *avec le détecteur Delphi à LEP*, Ph. D. Thesis, LAL **93-10** (1993).

[36] D. Bloch et al. (LEP B Lifetimes Working Group), *Averaging Lifetimes for* B *Hadron Species at LEP*, internal note, DELPHI **94-164** PHYS-467.

[37] P. Abreu et al. (Delphi Coll.), *Evidence for the* B_s^0 *meson production in* Z^0 *decays*, Phys. Lett. **B289** (1992) 199.

[38] D. Buskulic et al. (Aleph Coll.), *Measurement of the* B_s^0 *Lifetime and Production Rate With* $D_s^- \ell^+$ *Combinations in* Z *Decays*, Phys. Lett. **B361** (1995) 221.

[39] R.M. Barnett et al. (Particle Data Group), *Review of Particle Properties*, Phys. Rev. **D54** (1996) 1.

[40] D. Buskulic et al. (Aleph Coll.), Zeit. Phys. **C69** (1996) 585.

[41] F. Abe et al. (CDF Coll.), *Measurement of the* B_s *Meson Lifetime*, Phys. Rev. Lett. **74** (1995) 4988.

[42] R. Akers et al. (Opal Coll.), *An Improved Measurement of the* B_s^0 *Lifetime*, Phys. Lett. **B350** (1995) 273.

[43] D. Bloch, B, D*Spectroscopy and* $\overline{B} \to D/D^*/D^{**} \ell \overline{\nu}$, Proceedings of the Int. EPS HEP Conference, Brussels, July 1995, World Scientific (1996) 450, and references therein.